ELECTRON TRANSPORT AND ION DIFFUSIVITY THROUGH THE SOLID ELECTROLYTE INTERPHASE IN LITHIUM ION BATTERIES WITH SILICON ANODES

A Dissertation

by

LAURA ELENA BENITEZ

Submitted to the Office of Graduate and Professional Studies of
Texas A&M University
in partial fulfillment of the requirements for the degree of

DOCTOR OF PHILOSOPHY

Chair of Committee,	Jorge M. Seminario
Committee Members,	Jun Zou
	Perla B. Balbuena
	Jose Silva-Martinez
Head of Department,	Miroslav M. Begovic

August 2017

Major Subject: Electrical Engineering

ABSTRACT

Lithium-ion batteries (LIB) are the best option among batteries for portable electronic, power tools, and electric vehicles due to their higher energy storage, higher power, and lighter weight than other battery technologies such as Ni-based or lead acid. However, Li-ion batteries still face challenges such as safety, life, performance, and cost. One way to contribute to the solutions of these challenges and, consequently, improve the performance of Li-ion cells is to develop and design more stable passivation films at the electrode-electrolyte interface. Therefore, having a better understanding of the molecular processes that lead to the nucleation, growth, structure and morphology, as well as the electron and ion transport properties of the solid electrolyte interphase (SEI) is highly important for the development of new or improved lithium-ion batteries. In this work, computational methods, which allow studying phenomena not easily observable with experimental techniques, are used to study the electron transfer characteristics and the lithium ion diffusivity of the materials found in the SEI film formed in LIB with silicon anodes.

First, ab initio computational methods are used to study the electron transfer through selected finite models of SEI films formed at the anode-electrolyte interface. A combined ab initio density functional theory (DFT) and Green's functions approach, as implemented in the Generalized Electron Nano-Interface Program (GENIP), is used to calculate the current-voltage characteristics of selected SEI configurations. The models studied consist of a Li_xSi_y cluster, a SEI product (LiF, Li_2O or Li_2CO_3), and an

electrolyte component, ethylene carbonate (EC). Various parameters are considered in the investigation including: various lithiated states for the anode; several thicknesses and configurations for the SEI layer; and the presence of surface oxides (SiO_2 and $Li_2Si_2O_5$). The trend of conductance is found to be $Li_2O > SiO_2 > LiF > Li_2CO_3 > Li_2Si_2O_5$, at the same applied voltage and anode configuration.

Then, lithium-ion diffusion is studied in the main components of the SEI layer using classical molecular dynamics (MD) simulations in order to provide insights and to calculate the diffusion coefficients of Li-ions at temperatures in the range of 250 K to 400 K. The compounds studied are lithium fluoride (LiF), lithium oxide (Li_2O) and lithium carbonate (Li_2CO_3). A slight increase in the diffusivity as the temperature increases is found and since diffusion is noticeable at high temperatures, Li-ion diffusion in the range of 1300 to 1800 K is also studied and the diffusion mechanisms involved in each SEI compound are analyzed. The mechanisms of Li-ion diffusion observed include vacancy assisted and knock-off diffusion in LiF, direct exchange in Li_2O, and vacancy and knock-off in Li_2CO_3. Moreover, the effect that an applied an electric field has in the diffusion of Li-ions at room temperature is also evaluated.

The long-term goal is to eventually have more control over interface parameters such as composition, structure, porosity and thickness, and thus accurately design SEI films and therefore better Li-ion batteries. This work is a step towards this ultimate goal.

DEDICATION

To my loving husband Rogelio for his constant support and encouragement over the years, and for keeping me going when I wanted to give up.

To my wonderful son Rogelio Rene, who always had a smile and patiently waited when mommy was busy.

ACKNOWLEDGMENTS

First, and foremost I would like to thank God, because without him, none of my plans would have been possible.

I would like to express my most sincere gratitude to my advisor, Dr. Jorge Seminario, for his continuous support of my studies and research, for his patience and, enthusiasm, for sharing all his knowledge and for guiding me while also giving me the room to work in my own way.

I would also like to extend my gratitude to Dr. Perla Balbuena for her encouragement and advice throughout the course of this research.

Thanks to the rest of my committee members, Dr. Zou and Dr. Silva-Martinez for their insightful comments and questions, as well as for the time dedicated to this dissertation.

I want to thank the various members of the Molecular- and Nano- Technology Group with whom I had the opportunity to work and spend time. Thanks to Paola and Dahiyana for showing me how to perform DFT calculations and how to use GENIP. I am extremely grateful for Karim's, Naren's and Victor's assistance in finding the appropriate force fields used in the MD simulations. Thank you for all your help, for all the stimulating discussions, as well as for all the fun we had during our time at Texas A&M. Special thanks to my officemate Naren, who as a good friend was always willing to help and give his best suggestions. I greatly benefited from his profound scientific understanding and his ability to put complex ideas into simple terms.

I want to briefly thank Ilse and Coco for their friendship, for bringing joy to my life when I needed it the most.

I am also grateful for the financial support from the Assistant Secretary for Energy Efficiency and Renewable Energy, Office of Vehicle Technologies of the U.S. Department of Energy under Contract No. DE-AC02-05CH11231, Subcontract No. 7060634, and Contract No. DE-EE0007766 under the Advanced Battery Materials Research (BMR) Program.

I would like to acknowledge the support of the Texas A&M Supercomputer Facility and the Texas Advanced Computing Center.

I want to express my deepest gratitude to my family who has always supported me. Thanks to my parents, Laura and Francisco Espinoza, as well as my in-laws, Minerva and Rogelio Benitez, for enthusiastically and patiently taking care of Rogelito and cooking meals when I needed to work on my research and write this dissertation. Thanks also to the rest of my family: my sister Nora Espinoza; my brother Paco and his family, Paquito and Yuridia Espinoza; my sister-in-law, nephew and niece, Madelin, Leonardo and Aranza Gonzalez; and the rest of my extended family aunts, uncles and cousins for all the prayers.

Last but not least, thanks to my husband Rogelio for his patience and love, for the financial support all through my studies, for his encouragement every day and when I wanted to give up, for being a great example to follow, and for being a great dad. Thank you for everything!

CONTRIBUTORS AND FUNDING SOURCES

Contributors

This work was supervised by a dissertation committee consisting of Professors Jorge M. Seminario, Jun Zou and Jose Silva-Martinez from the Department of Electrical and Computer Engineering and Professor Perla B. Balbuena from the Department of Chemical Engineering.

All work for the dissertation was completed by the student, under advisement of Professor Jorge M. Seminario from the Department of Electrical and Computer Engineering.

Funding Sources

This work was made possible in part by the support of the Texas A&M Supercomputer Facility and the Texas Advanced Computing Center.

This work was made possible by financial support from the Assistant Secretary for Energy Efficiency and Renewable Energy, Office of Vehicle Technologies of the U.S. Department of Energy under Contract No. DE-AC02-05CH11231, Subcontract No. 7060634, and Contract No. DE-EE0007766 under the Advanced Battery Materials Research (BMR) Program.

Its contents are solely the responsibility of the authors and do not necessarily represent the official views of the Office of Vehicle Technologies of the U.S. Department of Energy.

NOMENCLATURE

EC	Ethylene Carbonate
DFT	Density Functional Theory
DOS	Density of States
GENIP	Generalized Electron Nano-Interface Program
HOMO	Highest Occupied Molecular Orbital
I-V	Current-Voltage
LIB	Lithium-Ion Battery
LJ	Lennard-Jones
LUMO	Lowest Unoccupied Molecular Orbital
MD	Molecular Dynamics
MO	Molecular Orbital
MSD	Mean Square Displacement
GF	Green Function
SEI	Solid Electrolyte Interphase

TABLE OF CONTENTS

Page

Page

LIST OF FIGURES

Page

Page

Page

LIST OF TABLES

Page

1. INTRODUCTION*

Lithium-ion batteries (LIB) are the most popular rechargeable batteries and are nowadays been widely used in portable electronic devices and electric vehicles due to their relative high energy density, good cycle life and good power performance. Nevertheless, Li-ion batteries still face these main challenges: safety, life, performance and cost.[1-3] Current research includes developing and designing new electrode structures and materials, for both the anode and the cathode, as well as investigating the electrolyte and its interface with the electrodes.[1, 4]

In the following sections, lithium-ion battery basics, general LIB components and challenges are summarized. The electron transport and molecular dynamics theoretical background used in this study will be reviewed as well.

1.1. Lithium Ion Batteries

Li-ion batteries (LIB) are the most used type of rechargeable batteries in consumer electronics, and they are gaining popularity in electric vehicles (EVs) as well as in military and aerospace applications. Advantages include lighter weights, no memory effects, hundreds of charge/discharge cycles, relative low self-discharge, and high energy density.[5-7] Even though they were developed in the 1970s, several issues

*Part of this chapter is reprinted with permission from:
Electron Transport and Electrolyte Reduction in the Solid-Electrolyte Interphase of Rechargeable Lithium Ion Batteries with Silicon Anodes by L. Benitez and J. M. Seminario, 2016. *J. Phys. Chem. C*, 120, 17978-17988, Copyright 2016 by American Chemical Society.
Ion Diffusivity through the Solid Electrolyte Interphase in Lithium-Ion Batteries by L. Benitez and J. M. Seminario, 2017. *J. Electrochem. Soc.*, 164, Copyright 2017 by The Electrochemical Society.

remain: lithium-ion batteries require a protection/management circuit, they degrade even if not in use, they are expensive to manufacture, they are very sensitive to high temperatures, and they have a slight probability to burst into flames.[3, 6, 8-10] Even with these issues, lithium ion batteries are still a promising alternative energy source, instead of fossil fuels, to be used in vehicles. When used in EVs, LIB's provide clean energy storage capable of significantly contributing, in the long term, to the reduction of greenhouse gas emissions.[11] Moreover, the energy efficiency of LIB's in EVs can be as high as 90%, as compared to the internal combustion engine that has efficiency close to 40%.[11-12]

Lithium ion batteries are made of one or more cells. Each cell has three functional components: a positive electrode, a negative electrode and an electrolyte. Typically, the positive electrode is a metal oxide: a layered oxide (lithium cobalt oxide, $LiCoO_2$), a polyanion (lithium iron phosphate, "LFP", $LiFePO_4$), or a spinel (lithium manganese oxide, "LMO", $LiMn_2O$).[4, 13] The negative electrode is generally made from carbon (graphite).[4] The electrolyte is commonly an organic solvent mixed with Li-based salts. Typical electrolytes are ethylene carbonate (EC), propylene carbonates (PC), and diethyl carbonate (DEC). Typical Li-based salts are lithium hexa-fluorophosphate ($LiPF_6$), lithium perchlorate ($LiClO_4$), and lithium tetra-fluoroborate ($LiBF_4$).[14-15] Novel materials for each component are being investigated and developed in order to improve and resolve the main disadvantages. Materials in current research include $LiNiO_2$, Li_2MnO_3, $LiMnPO_4$, $LiVPO_4F$, S, Se and Te for the cathode; Si, Ge, Sn, $Li_4Ti_5O_{12}$ for

the anode; and polymers and solid materials such as polyethylene oxide **(**PEO), poly(methyl methacrylate)**, (**PMMA), and LiI/Al_2O_3 for the electrolyte.[1, 4, 8, 16]

In this study, the anode material is silicon since it has been shown to be a promising material;[17] it has the largest capacity to store Li, 4212 $mAhg^{-1}$, which is excellent when compared to graphite, which has a capacity of 372 $mAhg^{-1}$. The large capacity of Si takes place with a stoichiometry corresponding to $Li_{22}Si_{5.}$[18] On the other hand, Si is an abundant material and thus less expensive than graphite.[19] However, due to Si large capacity, a large volume expansion of ~300% at full lithiation is expected, causing mechanical stresses that produce cracks in the anode and lead to a loss of electrical contact and capacity fading, increased impedance, and thermal runaway; or in other words, to a general overall cell/battery failure.[19-20]

During charging of a LIB, shown in Figure 1.1(b), lithium ions move from the positive electrode (cathode) to the negative electrode (anode) passing through the Li-ion conductive electrolyte, while electrons flow via the outer circuit also from the positive to the negative electrode driven by an external charging source; similarly, during discharge, shown in Figure 1.1(d), the reverse process occurs: the Li ions return to the positive electrode and the electrons move from the negative to the positive electrode depositing their energy in an external load.

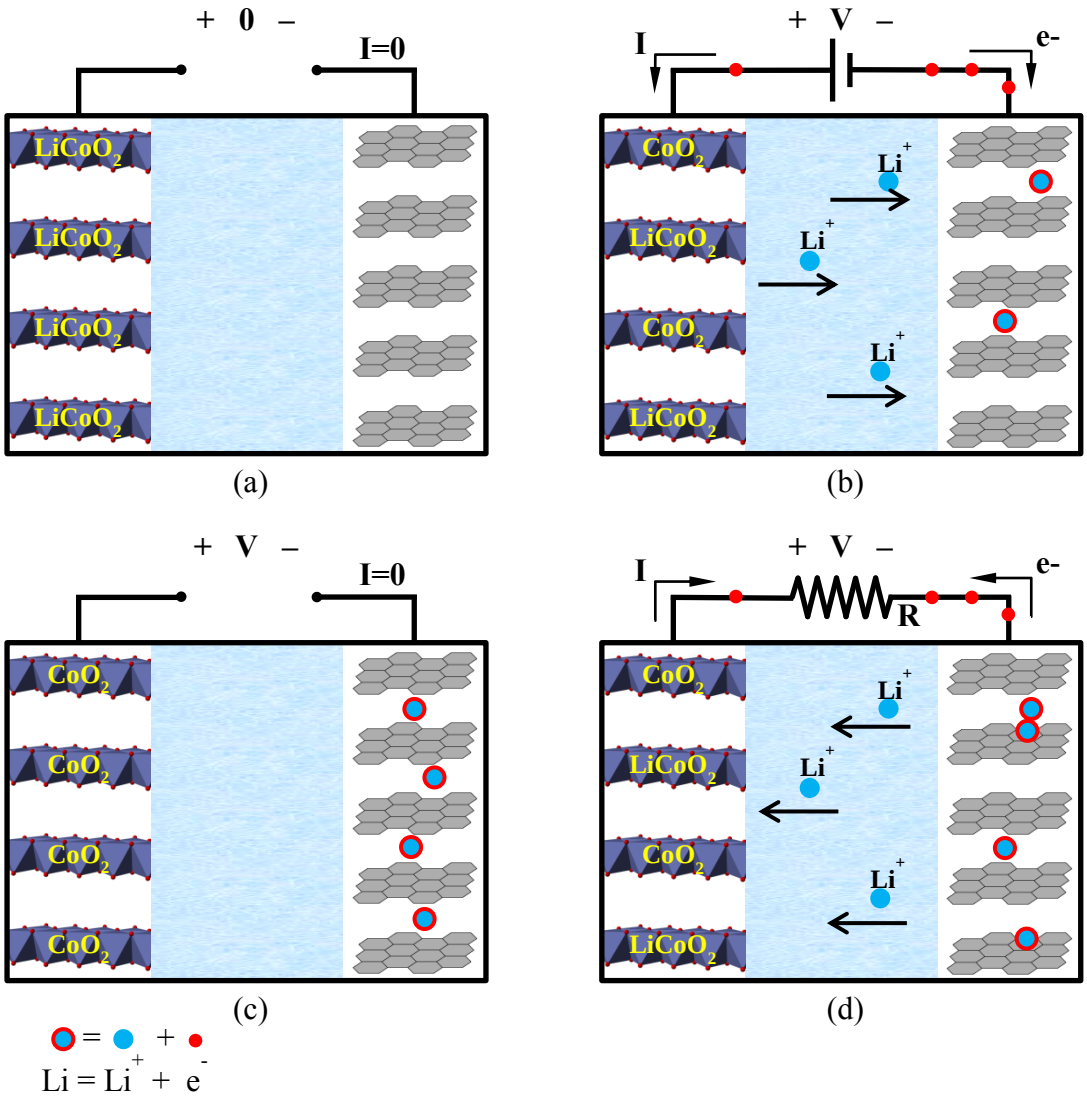

Figure 1.1. Schematic diagram of the lithium ion battery showing (a) a fully discharged state, (b) the charging mechanism, (c) a fully charged state, and (d) the discharging mechanism.

1.2. Solid Electrolyte Interphase

Just as in graphite anodes, a solid electrolyte interphase (SEI) is formed on the surface of silicon electrodes during the first charging cycles.[21] During the first cycles, the

electrolyte reduces at its interface with the anode and forms a passivating layer that consists of inorganic and organic products.[14] This SEI film consists of a dense layer found near the electrode followed by a porous layer near the electrolyte.[22-24] The denser (or inner) layer is composed of inorganic products such as LiF, Li_2O and Li_2CO_3, and the porous (or outer) layer is composed of organic products such as $(CH_2OCO_2Li)_2$, $ROCO_2Li$ and ROLi where R is an organic group such as CH_2, CH_3, CH_2CH_2, CH_2CH_3, $CH_2CH_2CH_3$ depending on the electrolyte solvent.[9, 14, 22-34] Composition and structure of SEI in Si anodes is similar to that of graphite anodes. Figure 1.2 shows a proposed model for the inner layer by Peled et. al[35] where the main components of the SEI are LiF, Li_2O and $LiCO_3$.[30-31]

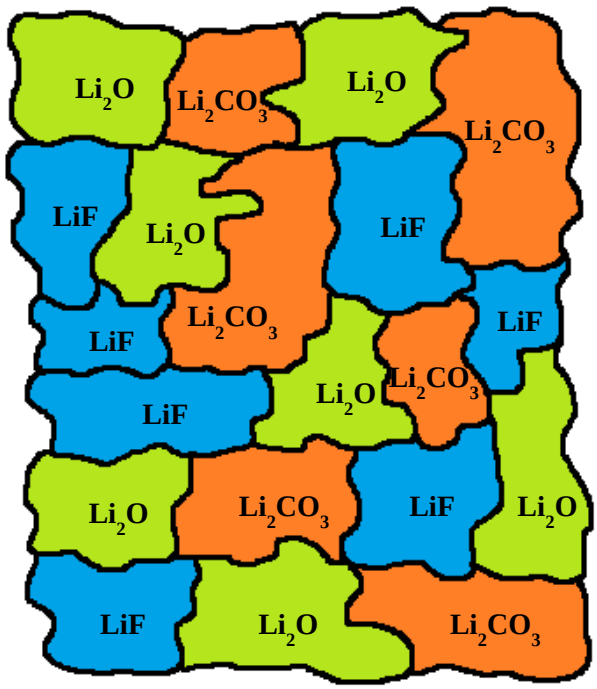

Figure 1.2. SEI model structure and composition.

In carbon anodes, the SEI formation protects the electrode against further solvent decomposition by blocking the electron leakage from the anode to the electrolyte,[36] which takes place during the charge of the battery. However in Si anodes, the huge volume expansion of the anode creates cracks in the SEI layer and generates new surfaces which are again exposed to the electrolyte,[37] as illustrated in Figure 1.3.

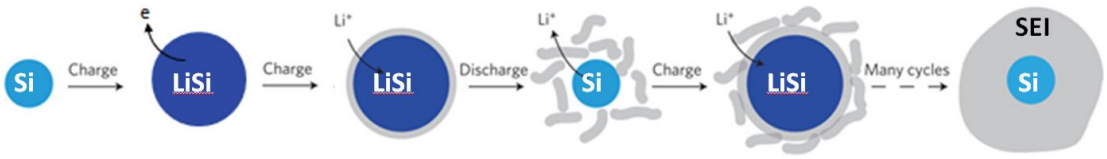

Figure 1.3. Schematic of SEI formation on silicon surfaces.

In both carbon and silicon anodes, the SEI film still allows the transport of Li^+ from the electrolyte to the negative electrode; lithium ions can move through the SEI by the exchange of ions between the electrolyte, the SEI compounds, and the lithium intercalated in the electrodes.[36] However, some Li^+ ions become trapped in the SEI thus leading to the irreversible capacity loss (ICL) in the initial cycles (during SEI formation) and capacity fading in subsequent cycles (during SEI evolution and growth).[38] Accordingly, battery capacity, stability, and performance are highly dependent on the quality and characteristics of the SEI, [14, 39-46] yet it is the "least understood component in lithium ion batteries".[47] This is due, in part, to the fact that the experimental analysis is very challenging. The SEI film thickness is very small (few Å to tens or hundreds of nanometers) and it is formed on the electrode surface thus making it almost impossible

to define the boundaries of the SEI, and to precisely detach it from the active material surface.[48-49] Moreover, most of the SEI components are highly reactive when exposed to contaminants, air or humidity.[14] For these reasons, *ex situ* characterization of the SEI becomes very difficult whereas *in situ* experiments require specially designed tools and measurement set ups.[2, 50] Given the difficulties of experimental techniques, computational simulations increasingly become a valuable tool to study properties of the SEI.

Many studies try to understand parameters such as composition, morphology and thickness, as well as to clarify formation and growth mechanisms of SEI films.[9, 28, 51-56] Its structure and composition have been investigated using, both *in situ* and *ex situ*,[14, 50, 57-58] experimental techniques such as X-ray photoelectron spectroscopy (XPS),[24] infrared spectroscopy (IR), nuclear magnetic resonance (NMR) spectroscopy,[32] Raman spectroscopy,[59] X-ray diffraction (XRD), transmission electron microscopy (TEM),[24, 32, 60] scanning electron microscopy (SEM), and time-of-flight secondary ion mass spectroscopy (TOF-SIMS)[61-62]; from these studies the most generally recognized inorganic compounds in literature are LiF, Li_2O and Li_2CO_3.

Other research has focused on studying ionic conduction,[63] tunneling barriers,[38] and interfacial capacitances,[64-65] but minimal efforts have been put toward studying electron transport and predicting electron leakage current in the individual solid-electrolyte interphase components. In Section 2 and Section 3 the investigation of the electron transfer through individual SEI compounds is presented and the results examined.

Other studies, both experimental and theoretical, have concentrated on Li-ion transport within the electrolyte and in the electrodes.[66-87] Some other investigations focus on the boundary between the liquid electrolyte and the electrode, and even the SEI as a whole,[24, 36, 61, 88-93] yet little attention has been put towards explaining transport mechanisms and predicting diffusion coefficients in the individual interphase components. In Section 4, the investigation of Li-ion diffusion in the three main components of the SEI is presented and the findings are discussed.

1.3. Motivation

Events where Li-ion batteries explode or run the risk of igniting have been reported in the past, thus causing companies to recall them and lose millions of dollars.[94-98] One way to improve the safety of Li-ion cells is to develop and design more stable SEI films.[28, 99] For that, having a more complete understanding of the nucleation, growth, as well as the electron and ion transport properties of the SEI formed in the anode-electrolyte interface is highly important in order to, ultimately, have more control over characteristics of the films, such as composition, structure and thickness.

1.4. Electron Transport

Electron transport in a nanoscopic junction is ballistic.[100-101] That is, the transport of electrons is not affected by the scattering in the material. This occurs when the mean free path of the electron is much longer than the length of the channel through which the electron travels. The electron transfer in this regime can be obtained by using the Landauer formalism.[102] However, when a molecule, cluster, or in general a group of

atoms are in the junction, the Green's Functions (GF) procedure needs to be combined with a quantum molecular structure theory such the density functional theory (DFT).[102-109]

The general configuration for electron transport comprises of a molecule and the probes of the measuring device (green atoms) as shown in Figure 1.4. The actual calculations are done on the extended molecule which consists on the molecule and a finite number of atoms from the bulk, or more precisely nanocontacts (hereupon called contacts).

Within the DFT-GF method, the quantum-mechanical calculations on the extended molecule and the density of states (DOS) of each contact bulk material are needed. Then the Generalized Electron Nano-Interface Program (GENIP), which combines the results of the DFT calculations with the GF formalism, is used to calculate the current-voltage characteristics of the systems.

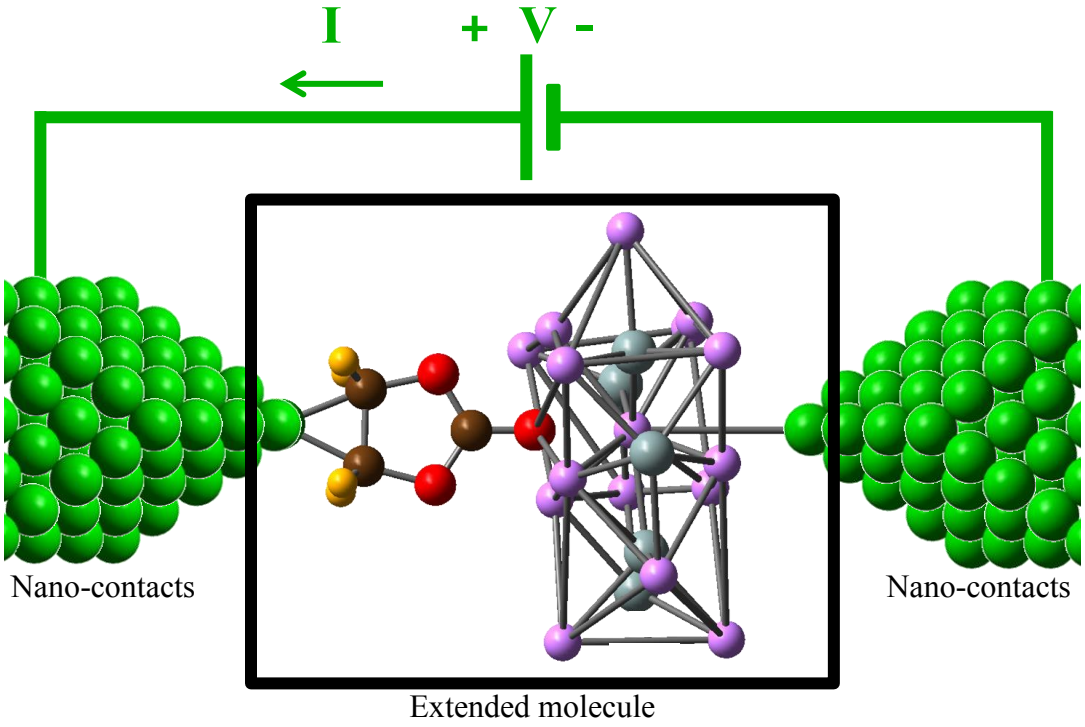

Figure 1.4. Metal-Molecule-Metal junction. Color code: Li: purple; Si: gray; O: red; H: yellow; C: brown; Au: green.

In the following sections, first the DFT basics are reviewed and then details of GENIP procedure are presented.

1.4.1. Density Functional Theory Basics

Density functional theory is a computational quantum mechanical method used to find the solution to the Schrödinger equation (SE) of a many-body system. It allows describing the electronic structure of the systems using the electron density.

The many-body, time-independent, non-relativistic Schrödinger equation, given in Equation (1.1), describes the wavefunction of a system as a function space:

$$\hat{H}\Psi(\vec{r}_1,\vec{r}_2,\vec{r}_3,\ldots,\vec{r}_N,\vec{R}_1,\vec{R}_2,\vec{R}_3,\ldots,\vec{R}_M) = E\Psi(\vec{r}_1,\vec{r}_2,\vec{r}_3,\ldots,\vec{r}_N,\vec{R}_1,\vec{R}_2,\vec{R}_3,\ldots,\vec{R}_M) \quad (1.1)$$

where $\vec{r}_i$ and $\vec{R}_A$ are the position vectors of the i^{th} electron and the A^{th} nucleus; and N and M are the total number of electrons and nuclei, respectively; Ψ and E are the wavefunction and energy of the system, respectively; and $\hat{H}$ is the Hamiltonian operator which depends on the system being described. The Hamiltonian, $\hat{H}$, takes the form of

$$\hat{H} = \hat{T}^{elec} + \hat{T}^{nucl} + \hat{V}^{ee} + \hat{V}^{nn} + \hat{V}^{ne} \tag{1.2}$$

where $\hat{T}^{elec}$ and $\hat{T}^{nucl}$ are the kinetic energy of the electrons and the nuclei given by Equations (1.3) and (1.4) respectively;

$$\hat{T}^{elec} = -\frac{\hbar^2}{2m_e}\sum_{i=1}^{N}\nabla_i^2 \tag{1.3}$$

$$\hat{T}^{nucl} = -\frac{\hbar^2}{2m_A}\sum_{A=1}^{M}\nabla_A^2 \tag{1.4}$$

$\hat{V}^{ee}$, $\hat{V}^{nn}$ and $\hat{V}^{ne}$ correspond to the electron-electron repulsion, the nuclear-nuclear repulsion and the electron-nuclear coulomb attraction[110-111] expressed in Equations (1.5) to (1.7) respectively;

$$\hat{V}^{ee} = \frac{e^2}{4\pi\epsilon_0}\sum_{i=1}^{N}\sum_{j>i}^{N}\frac{1}{|\vec{r}_i - \vec{r}_j|} \tag{1.5}$$

$$\hat{V}^{nn} = \frac{e^2}{4\pi\epsilon_0}\sum_{A=1}^{M}\sum_{B>A}^{M}\frac{Z_A Z_B}{|\vec{R}_A - \vec{R}_B|} \tag{1.6}$$

$$\hat{V}^{ne} = -\frac{e^2}{4\pi\epsilon_0}\sum_{i=1}^{N}\sum_{A=1}^{M}\frac{Z_A}{|\vec{r}_i - \vec{R}_A|} \tag{1.7}$$

m_e is the mass of the electron; m_A and Z_A are the mass and the atomic number of the nucleus A; and ϵ_0 is the electric permittivity. Here the spin of the electrons is omitted in order to simplify the notation. Solutions to simple systems, such as the particle in a box or the hydrogen atom, can be found analytically in closed form; however, most of the

systems of interest have multiple electrons interacting with multiple nuclei and a closed form or analytical solution is impossible to find. Thus, approximations are the only option left. First, the Born-Oppenheimer approximation allows treating the motion of the electrons and the nuclei separately. Since nuclei are much heavier than electrons, and electrons react faster to changes in their surroundings, the nuclei can be fixed (nuclei velocity equal to zero) and thus the term $\hat{T}^{nucl}$ can be neglected, $\hat{V}^{nn}$ becomes a constant[111], and therefore, with $\hat{T}^{elec} = \hat{T}$, Equation (1.2) becomes

$$\hat{H} = \hat{T} + \hat{V}^{ne} + \hat{V}^{ee} \tag{1.8}$$

Moreover, $\hat{V}^{ne}$ can be expressed as

$$\hat{V}^{ne} = \sum_{i=1}^{N} v(\vec{r}_i) \tag{1.9}$$

with

$$v(\vec{r}_i) = -\frac{e^2}{4\pi\epsilon_0} \sum_{A=1}^{M} \frac{Z_A}{|\vec{r}_i - \vec{R}_A|} \tag{1.10}$$

where $v(\vec{r}_i)$ is the external potential of interest, which in materials simulations is the interaction of the electrons with the atomic nuclei.

It is worth noting that the wavefunction, Ψ, cannot be directly observed; the quantity of physical interest that can be actually be measured is the probability of finding a set of N electrons, in any order, at a particular position $\vec{r}, \vec{r}_2, \vec{r}_3, \ldots, \vec{r}_N$. This probability is defined as $\Psi\Psi^*$. A closely related quantity is the electron density, $\rho(\vec{r})$. It can be obtained from the expectation value of the density operator given in Equation (1.11) where $\sum_{i=1}^{N} \delta(\vec{r} - \vec{r}_i)$ is the density operator $\hat{\rho}$, δ is the Dirac delta function, and with $|\Psi|^2 = \Psi\Psi^*$,

$$\rho(\vec{r}) = \langle \Psi | \sum_{i=1}^{N} \delta(\vec{r} - \vec{r}_i) | \Psi \rangle \tag{1.11}$$

$$\begin{aligned}\rho(\vec{r}) = & \int |\Psi(\vec{r},\vec{r}_2,\vec{r}_3,\ldots,\vec{r}_N)|^2 d\vec{r}_2 \ldots d\vec{r}_N \\ & + \int |\Psi(\vec{r}_1,\vec{r},\vec{r}_3,\ldots,\vec{r}_N)|^2 d\vec{r}_1 d\vec{r}_3 \ldots d\vec{r}_N \\ & + \int |\Psi(\vec{r}_1,\vec{r}_2,\vec{r},\ldots,\vec{r}_N)|^2 d\vec{r}_1 d\vec{r}_2 d\vec{r}_4 \ldots d\vec{r}_N + \ldots\end{aligned} \tag{1.12}$$

and since electrons are indistinguishable, exchanging electron coordinates has no effect on the probability density $|\Psi|^2$, then, all integrals are equivalent, such that

$$\int |\Psi(\vec{r},\vec{r}_2,\vec{r}_3,\ldots,\vec{r}_N)|^2 d\vec{r}_2 \ldots d\vec{r}_N = \int |\Psi(\vec{r}_1,\vec{r},\vec{r}_3,\ldots,\vec{r}_N)|^2 d\vec{r}_1 d\vec{r}_3 \ldots d\vec{r}_N \tag{1.13}$$

$$\int |\Psi(\vec{r}_1,\vec{r},\vec{r}_3,\ldots,\vec{r}_N)|^2 d\vec{r}_1 d\vec{r}_3 \ldots d\vec{r}_N = \int |\Psi(\vec{r}_1,\vec{r}_2,\vec{r},\ldots,\vec{r}_N)|^2 d\vec{r}_1 d\vec{r}_2 d\vec{r}_4 \ldots d\vec{r}_N \tag{1.14}$$

and so on; thus

$$\rho(\vec{r}) = N \int |\Psi(\vec{r},\vec{r}_2,\vec{r}_3,\ldots,\vec{r}_N)|^2 d\vec{r}_2 \ldots d\vec{r}_N \tag{1.15}$$

Moreover, the total electronic energy, E, for a given Ψ is the expectation value of the Hamiltonian, $\hat{H}$, that is

$$E = \langle \Psi | \hat{H} | \Psi \rangle \tag{1.16}$$

with Equation (1.8) into Equation (1.16),

$$E = \langle \Psi | \hat{T} + \hat{V}^{ne} + \hat{V}^{ee} | \Psi \rangle \tag{1.17}$$

$$E = \langle \Psi | \hat{T} + \hat{V}^{ee} | \Psi \rangle + \langle \Psi | \hat{V}^{ne} | \Psi \rangle \tag{1.18}$$

and with the second term of Equation (1.18), the interaction of the external potential with the quantum mechanical system, being equivalent to the interaction of the external potential with the classical charge distribution,[112-113] that is,

$$\langle \Psi | \hat{V}^{ne} | \Psi \rangle = \int v(\vec{r}) \rho(\vec{r}) d\vec{r} \tag{1.19}$$

Equation (1.18) becomes

$$E = \int v(\vec{r})\rho(\vec{r})d\vec{r} + \langle \Psi | \hat{T} + \hat{V}^{ee} | \Psi \rangle \quad (1.20)$$

Density functional theory relies in two theorems proved by Hohenberg and Kohn (HK),[114] and the derivation of a set of equations by Kohn and Sham (KS) in the 1960's.[115-116] The first HK theorem states that $v(\vec{r})$ is a functional of $\rho(\vec{r})$ and that implies that the energy E is a functional of $\rho(\vec{r})$ and therefore,

$$E = E[\rho] \quad (1.21)$$

and, since $\hat{T}$ and $\hat{V}^{ee}$ are also functionals of $\rho(\vec{r})$, it can be defined that

$$F[\rho] = \langle \Psi | \hat{T} + \hat{V}^{ee} | \Psi \rangle \quad (1.22)$$

where $F[\rho]$ is a universal functional, that is, it does not depend on the system analyzed, it is the same for all systems; thus Equation (1.20) results in

$$E[\rho(\vec{r})] = \int v(\vec{r})\rho(\vec{r})d\vec{r} + F[\rho(\vec{r})] \quad (1.23)$$

Consequently, the solution of the SE depends on finding electron density, which is a function of only 3 spatial variables as compared to directly solving the SE which is a function of 3N variables (where N is the number of electrons in the system).

The second HK theorem states that the electron density that minimizes this energy functional is the exact electron density corresponding to the full solution of the SE and establishes a variational principle. That is,

$$E[\rho(\vec{r})] \geq E_0[\rho_0(\vec{r})] \quad (1.24)$$

where $\rho_0(\vec{r})$, is the true ground state electron density, and E_0 is the ground state energy, which is the lowest energy eigenvalue of the time-independent Schrödinger equation. Both ground state electron density and energy could be found by varying a trial electron density, ρ, until the total energy is minimized,

$$E_0[\rho_0(\vec{r})] = \min_\rho E[\rho(\vec{r})] \tag{1.25}$$

or

$$E_0 = \min_\rho\{ F[\rho(\vec{r})] + \int v(\vec{r})\rho(\vec{r})d\vec{r} \} \tag{1.26}$$

In this case there is no need to involve the wavefunction Ψ, but some issues still remain, such as the degeneracy of the ground state and the v-representability of the electron density.[117-118] Furthermore, a generalization of this HK theorem which does not require the v-representability of the density was found by Levy and Lieb.[119-120] Starting from the variational principle, Equation (1.27), and then using a two-step minimization, Equation (1.28),

$$E_0 = \min_\Psi \langle \Psi | \hat{H} | \Psi \rangle \tag{1.27}$$

$$E_0 = \min_\rho \min_{\Psi\to\rho} \langle \Psi | \hat{H} | \Psi \rangle \tag{1.28}$$

then substituting the Hamiltonian $\hat{H}$ from Equation (1.8) to yield

$$E_0 = \min_\rho \{ \min_{\Psi\to\rho} \{ \langle \Psi | \hat{T} + \hat{V}^{ee} | \Psi \rangle + \langle \Psi | \hat{V}^{ne} | \Psi \rangle \} \} \tag{1.29}$$

and finally separating the terms to obtain

$$E_0 = \min_\rho \{ \min_{\Psi\to\rho} \{ \langle \Psi | \hat{T} + \hat{V}^{ee} | \Psi \rangle \} + \min_{\Psi\to\rho} \{ \langle \Psi | \hat{V}^{ne} | \Psi \rangle \} \} \tag{1.30}$$

The outer minimization searches over all the ρ's that integrate to N, and the inner minimization is restricted to all the antisymmetric wavefunctions Ψ that lead to $\rho(\vec{r})$. Then comparing with Equation (1.26) it follows that

$$\int v(\vec{r})\rho(\vec{r})d\vec{r} = \min_{\Psi\to\rho} \{ \langle \Psi | \hat{V}^{ne} | \Psi \rangle \} \tag{1.31}$$

and also the Levy-Lieb constrained-search functional is obtained as

$$F[\rho] = \min_{\Psi\to\rho} \{ \langle \Psi | \hat{T} + \hat{V}^{ee} | \Psi \rangle \} \tag{1.32}$$

In this case, Ψ is the wavefunction that yields ρ and minimizes the expectation value of $\hat{T} + \hat{V}^{ee}$ only. This result is important since the $v(\vec{r})$ term is not needed in the constraint search thus making this $F[\rho]$ truly universal.[118]

Furthermore, Kohn and Sham's work established the basis for the functionals employed by current DFT methods where the energy is partitioned in several terms and thus find $F[\rho]$. For the interpretation of the KS procedure, a system with the Hamiltonian

$$\hat{H}_\lambda = \hat{T} + \hat{V}_\lambda^{ne} + \lambda\hat{V}^{ee} \tag{1.33}$$

is considered.[118, 121] In Equation (1.33), $\hat{T}$ and $\hat{V}^{ee}$ are the kinetic and potential energies of the system respectively; λ is a parameter that varies from 0 to 1; and $\hat{V}_\lambda^{ne}$ is the nuclear-electron energy of such system. Such λ-scaled $\hat{V}^{ee}$ system is also chosen to always yield the density of the real system, $\rho(\vec{r})$, for any λ between 0 and 1. When $\lambda = 0$, $\hat{H}_\lambda = \hat{H}_0$ is the Hamiltonian corresponding to the non-interactive system with an effective potential, $v_0(\vec{r}) = v_{eff}(\vec{r}) = v_s(\vec{r})$. This effective potential, when applied to the non-interactive system, yields the same density as the true system. When $\lambda = 1$, $\hat{H}_\lambda = \hat{H}_1 = \hat{H}$ is the Hamiltonian of the real system under an external potential $v_1(\vec{r}) = v_{ext}(\vec{r})$.

Thus the energy of the λ-scaled system is given by

$$E_\lambda = \int v_\lambda(\vec{r})\rho(\vec{r})d\vec{r} + \langle\Psi_\lambda|\hat{T} + \lambda\hat{V}^{ee}|\Psi_\lambda\rangle \tag{1.34}$$

Deriving and integrating Equation (1.34) with respect to λ from 0 to 1; and since the energy for $\lambda = 1$, E_1, corresponds to the energy of the real system, E; and with the energy for $\lambda = 0$, E_0, being equal to the energy, E_s, of an imaginary system with no electron-electron interactions E_s, Equation (1.34) becomes

$$\int_0^1 E_\lambda d\lambda = \int_0^1 \int dv_\lambda(\vec{r})\rho(\vec{r})d\vec{r}\, d\lambda + \int_0^1 \langle \Psi_\lambda | \hat{V}^{ee} | \Psi_\lambda \rangle d\lambda \quad (1.35)$$

thus,

$$E - E_S = \int v_{ext}(\vec{r})\rho(\vec{r})d\vec{r} - \int v_s(\vec{r})\rho(\vec{r})d\vec{r} + \int_0^1 \langle \Psi_\lambda | \hat{V}^{ee} | \Psi_\lambda \rangle d\lambda \quad (1.36)$$

When there is no electron-electron interactions, $\lambda = 0$, the total energy E_s is simply the sum of the potential energy with the nuclei and the kinetic energy of the electrons, i.e.,

$$E_s = \int v_s(\vec{r})\rho(\vec{r})d\vec{r} + T_s \quad (1.37)$$

Then inserting Equation (1.37) into (1.36), and since $v_0 = v_s$ and $v_1 = v_{ext}$, the v_s cancel each other, therefore yielding

$$E = T_s + \int v_{ext}(\vec{r})\rho(\vec{r})d\vec{r} + \int_0^1 \langle \Psi_\lambda | \hat{V}^{ee} | \Psi_\lambda \rangle d\lambda \quad (1.38)$$

where the calculation of the last term is really the holy grail of DFT. An analytical solution does not exist, and therefore several approximations have been provided. One of the most common ones starts with the Kohn-Sham procedure,[116] in which the last term of Equation (1.38) is split into

$$\int_0^1 \langle \Psi_\lambda | \hat{V}^{ee} | \Psi_\lambda \rangle d\lambda = V_{class}[\rho] + E_{XC}[\rho] \quad (1.39)$$

where $V_{class}[\rho]$ is the classical Coulomb energy given by

$$V_{class}[\rho] = \frac{1}{2}\int \frac{\rho(\vec{r}_1)\rho(\vec{r}_2)d\vec{r}_1 d\vec{r}_2}{|\vec{r}_1 - \vec{r}_2|} \quad (1.40)$$

and $E_{XC}[\rho]$ is the exchange-correlation energy. Note that E_{XC} does not correspond to $E_X + E_C$ from the standard Hartee-Fock definitions; E_{XC} from Equation (1.39) contains a portion of the kinetic energy of the real system. Finally the total energy of the system can be expressed as

$$E[\rho] = T_s[\rho] + \int v_{ext}(\vec{r})\rho(\vec{r})d\vec{r} + V_{class}[\rho] + E_{XC}[\rho] \quad (1.41)$$

Once E_{XC} is approximated, the KS equations can be solved self-consistently. Kohn and Sham's work demonstrated that the right electron density can be found from solving the one-electron set of Schrodinger equations (KS equations)

$$\{\hat{T}_s + \hat{V}_s\}\Phi_i(\vec{r}) = \varepsilon_i\Phi_i(\vec{r}) \quad (1.42)$$

where $\hat{T}_s$ is not the true kinetic energy but that of the system with non-interacting electrons and is given by

$$\hat{T}^{elec} = -\frac{\hbar^2}{2m_e}\sum_{i=1}^{N}\langle\Phi_i(\vec{r})|\nabla_i^2|\Phi_i(\vec{r})\rangle \quad (1.43)$$

Also, $\Phi_i(\vec{r})$ are the single-electron wavefunctions, or KS orbitals, and they yield the real system density by

$$\rho(\vec{r}) = \sum_{i=1}^{N}|\Phi_i(\vec{r})|^2 \quad (1.44)$$

Moreover,

$$\hat{V}_s = \hat{V}_{ext} + \hat{V}_{class} + \hat{V}_{XC} \quad (1.45)$$

$$\hat{V}_{class}(\vec{r}) = \frac{\delta V_{class}[\rho(\vec{r})]}{\delta\rho(\vec{r})}\Big|_{\rho=\rho_0} = \frac{1}{2}\int\frac{\rho(\vec{r}_2)d\vec{r}_2}{|\vec{r} - \vec{r}_2|} \quad (1.46)$$

$$\hat{V}_{XC}(\vec{r}) = \frac{\delta E_{XC}[\rho(\vec{r})]}{\delta\rho(\vec{r})}\Big|_{\rho=\rho_0} \quad (1.47)$$

To solve the KS equations, $V_{class}(\vec{r})$ is required, and to find $V_{class}(\vec{r})$, $\rho(\vec{r})$ needs to be defined. Moreover, to obtain $\rho(\vec{r})$, $\Phi_i(\vec{r})$ needs to be found from solving the KS equations. This leads to an iterative method described below:

1. Define an initial $\rho_1(\vec{r})$.
2. Solve KS equations and find $\Phi_i(\vec{r})$.

3. Calculate the new $\rho_2(\vec{r})$ from Equation (1.44).

4. Compare $\rho_2(\vec{r})$ with $\rho_1(\vec{r})$.

5. Continue the process until $\rho_{j+1} = \rho_j$, that is until $\rho_{j+1} = \rho_0$.

Returning to the E_{XC} term, its functional is not known so only approximations are used. Commonly used types are the local density approximation (LDA), the generalized gradient approximation (GGA) as well as hybrid functionals which incorporate Hartree-Fock and other ab initio or sometimes empirical functionals. Some examples of GGA functionals include Becke's 1988 functional,[122] Lee, Yang and Parr (LYP),[123] and Perdew and the first principles Wang's 1991 (PW91).[124-125] Some hybrid methods include Becke's 1993 functional[126] with LYP (B3LYP) and Becke's '93 with PW91 (B3PW91).

There are other methods to solve SE, such as Hartree-Fock (HF)[110] which is a computationally cheap method but only includes some electron correlation (same spin). Other methods, such as configuration interaction (CI), coupled cluster (CC) and Møller-Plesset perturbation theory (MP2, MP3, etc.) do account for the electron correlation but are computationally more costly than HF. Here is where DFT provides a better approximation at the cost of HF calculations.

1.4.2. Generalized Electron Nano-Interface Program (GENIP)

The current through a molecule (or device) can be calculated using Landauer equation as derived in previous works[100, 102, 127] and given by

$$I = \frac{2e}{h} \int_{E_f + \mu_1}^{E_f + \mu_2} T(E)(f_1 - f_2)dE \qquad (1.48)$$

where e is the charge of the electron, h is the Planck constant, T(E) is the transmission function, E is the energy, E_f is the Fermi level of the molecular junction, μ_k is the chemical potential of the contacts, and f_k is the Fermi distribution for contact k. The Fermi distribution f_i is given by

$$f_k(E - \mu_k) = \frac{1}{1 + e^{\frac{E - \mu_k}{k_B T}}} \tag{1.49}$$

where k_B is the Boltzmann's constant and T is the temperature. The transmission function T(E), obtained using GF^{100} is given by

$$T(E) = \text{Trace}(\Gamma_1 G_M^R \Gamma_2 G_M^A) \tag{1.50}$$

with

$$\Gamma_k = i\left(\Sigma_k^- - \Sigma_k^+\right) \tag{1.51}$$

where Γ_k is the coupling of contact k (k = 1,2) to the molecule and represents the electron escape rate from the contacts to the molecule; G^R is the retarded Green function and G^A is its conjugate transport ($G^{R\dagger}$) also called advanced Green function; and Σ_k is the contacts' self-energy which accounts for the interaction between the contact and the molecule.

The goal is then to find the Green function (G^R) in order to calculate the current-voltage characteristics of the system using Equations (1.48) to (1.51).

The ab initio calculations solve the Schrödinger equation

$$H_{KS}\Psi = \varepsilon S\Psi \tag{1.52}$$

to obtain the overlap matrix (S), the eigenvalues (ε) and the KS Hamiltonian (H_{KS}). Then the H_{KS} is transformed as follows

$$H_{KS}S^{-1} \rightarrow H_T \tag{1.53}$$

in order to solve the more general Schrödinger equation

$$H_T\Psi = E\Psi \tag{1.54}$$

The transformed Hamiltonian, H_T, is then partitioned into sections such that

$$H_T = \begin{pmatrix} H_1 & \tau_1 & 0 \\ \tau_1^{\dagger} & H_M & \tau_2^{\dagger} \\ 0 & \tau_2 & H_2 \end{pmatrix} \tag{1.55}$$

where H_k is the Hamiltonian of contact k, and τ_k is the interaction between contact k and the molecule.

The definition of the Green function[102] is given by

$$\begin{pmatrix} g_1^{-1} & -\tau_1 & 0 \\ -1_1^{\dagger} & E - H_M & -H_2^{\dagger} \\ 0 & -H_2 & g_2^{-1} \end{pmatrix} \begin{pmatrix} G_1 & G_{1M} & G_{12} \\ G_{M1} & G_M & G_{M2} \\ G_{21} & G_{2M} & G_2 \end{pmatrix} = \begin{pmatrix} I & 0 & 0 \\ 0 & I & 0 \\ 0 & 0 & I \end{pmatrix} \tag{1.56}$$

From the second column, the below equations are obtained and solved for G_{1M} and G_{2M}

$$g_1^{-1}G_{1M} - \tau_1 G_M = 0 \tag{1.57}$$

$$-\tau_1^{\dagger}G_{1M} + \left(E - H_M\right)G_M - {}_2^{\dagger}G_{2M} = 0 \tag{1.58}$$

$$g_2^{-1}G_{2M} - \tau_2 G_M = 0 \tag{1.59}$$

yielding

$$G_{1M} = g_1\tau_1 G_M \tag{1.60}$$

$$G_{1M} = g_1\tau_1 G_M \tag{1.61}$$

Thus substituting Equations (1.60) and (1.61) into (1.58) the Green function is obtained

$$G_M = \left[E - H_M - \Sigma_1 - \Sigma_2\right]^{-1} \tag{1.62}$$

where

$$\Sigma_k = \tau_k g_k \tau_k^{\dagger} \tag{1.63}$$

The complex Green function g_k, provides information from the bulk contacts to the DFT-GF formalism.[101] It is obtained from ab initio DFT calculations on a periodic system of the bulk material. It is defined as

$$g_k = \begin{pmatrix} DOS_j s & 0 & 0 & 0 \\ 0 & DOS_j p & 0 & 0 \\ 0 & 0 & DOS_j d_{t_{2g}} & 0 \\ 0 & 0 & 0 & DOS_j d_{e_g} \end{pmatrix} \tag{1.64}$$

where the diagonal are matrices proportional to the density of states (DOS) of the bulk material. The diagonal matrices are constructed in a way that their size is equal to the number of basis functions (s-type, p-type, d-type) used to model the electronic structure of the contact atoms.

1.5. Molecular Dynamics Basics

Molecular dynamics (MD) is a computational instrument to simulate a group of particles (*in silico*) using models to mimic the dynamical behavior of the particles (atoms, molecules, clusters, etc.) over a period of time by numerically solving the classical equations of motion (Newton's equations of motion). In general, for a MD simulation three groups of information need to be specified: the algorithm to solve the

integral equations of motion, the initial conditions and structure of the system and the interaction between the particles. Afterwards, properties of interest can be measured over some period of time by selecting an appropriate statistical ensemble.

To solve Newton's equations of motion a numerical algorithm is typically used given that analytical solutions are impossible to find due to the complexity of systems. The goal is to obtain the particle positions $\vec{r}_i(t + \Delta t)$ in terms of their positions $\vec{r}_i(t)$. Several methods include leapfrog, Verlet, velocity-Verlet and Beeman. The most commonly used method is the Verlet algorithm.[128]

The initial conditions consist on specifying the boundary conditions (periodic or non-periodic) as well as the initial positions and velocities of the particles.

The interaction between particles is described by force fields, which consist on a specific interatomic potential class together with its set of parameters. These parameters are usually found by experimental methods and/or, more recently, by quantum mechanical calculations. Force fields are used to calculate the potential energy of the system, given by

$$E_{pot} = E_{bonded} + E_{non\text{-}bonded} \tag{1.65}$$

where

$$E_{bonded} = E_{bond} + E_{angle} + E_{dihedral} \tag{1.66}$$

and

$$E_{non\text{-}bonded} = E_{electrostatic} + E_{Van\ der\ Waals} \tag{1.67}$$

The terms E_{bond} and E_{angle} are usually modeled by harmonic potentials, and the $E_{dihedral}$ term varies depending on the implementation. The $E_{electrostatic}$ term is usually

computed with Coulumb's law and the $E_{Van\ der\ Waals}$ term with a Lennard-Jones (LJ) potential.

Interactions in ionic solids can be simplified by treating the ions as point charges. Therefore there is an attraction force between the particles of opposite charge as well as a repulsive force between particles with same charge.[129]

The attractive energy can be represented by a coulombic pairwise interaction given by

$$E_{Coul} = \frac{q_i q_j}{\epsilon r_{ij}} \qquad r_{ij} < r_c \qquad (1.68)$$

where q_i and q_j are the charges of the atoms, ϵ is the dielectric constant, r_{ij} is the distance between the particles i and j, and r_c is the cutoff distance. Moreover, long range coulombic interactions can be evaluated by several techniques, for example the Ewald summation technique.

The repulsive energy can be modeled by the Lennard-Jones potential or by the Buckingham potential. Furthermore, both LJ and Buckingham potentials contain a short-range repulsive term and a long-range attractive term. The attractive term is regularly known as the C6 term. The standard 6-12 LJ potential and its 6-9 variation are respectively given by

$$E_{6\text{-}12\ LJ} = 4\varepsilon \left[\left(\frac{\sigma}{r_{ij}} \right)^{12} - \left(\frac{\sigma}{r_{ij}} \right)^{6} \right] \qquad r_{ij} < r_c \qquad (1.69)$$

$$E_{6\text{-}9\ LJ} = \varepsilon \left[2 \left(\frac{\sigma}{r_{ij}} \right)^{9} - 3 \left(\frac{\sigma}{r_{ij}} \right)^{6} \right] \qquad r_{ij} < r_c \qquad (1.70)$$

where ε is the depth of the potential well, σ is the distance at which the potential is zero, $\sigma = 2^{(-1/6)}r_m$, r_m is the distance at the minimum energy, r_{ij} is the distance between the atoms, and r_c is the cutoff distance.

The Buckingham potential is given by

$$E_{Buck} = Ae^{-r_{ij}/\rho} - \frac{C}{r_{ij}^6} \qquad r_{ij} < r_c \tag{1.71}$$

where A and C are constants, and ρ is an ionic pair dependent parameter.

In order to keep quantities like temperature and pressure constant to simulate experiment environments, an ensemble can be used. An ensemble consists on a set of variables to be kept fixed. Among these variables are: the number of particles (N), the volume (V), the energy (E), the chemical potential (μ), the pressure (P) and/or the temperature (T). The most common include the microcanonical ensemble (NVE, where N, V and E are fixed), the canonical ensemble (or NVT, with N,V and T fixed), and the grand canonical ensemble (or μVT, with μ,V and T fixed).[130]

Molecular dynamics can be used to examine the structure and dynamics at atomic scale. Properties that can be measured include structural conformations (radial distribution function), transport characteristics (viscosity, diffusivity, thermal conductivity, etc.) as well as other static and non-equilibrium reactions (thermal expansion coefficient, plastic deformation, etc.).[131] Diffusion coefficients (D) are calculated from the mean square displacement (MSD), since D is proportional to the MSD[93] as shown by

$$D = \frac{1}{6}\left\langle \left|\vec{r}(t) - \vec{r}(t_0)\right|^2 \right\rangle \tag{1.72}$$

where r is the position of the particle at each time step, t is the time, t_0 is the initial time, $\vec{r}(t) - \vec{r}(t_0)$ is the distance traveled by the particle over the time interval $(t - t_0)$, and $\langle|\vec{r}(t) - \vec{r}(t_0)|^2\rangle$ is the MSD. The diffusion coefficient can be found from the slope of the MSD vs time.

The general procedure for MD is show in Figure 1.5. First, the initial configuration of the system is specified as well as the force fields to be used. Then the instantaneous forces acting on the particles are found using the potential energy, which can be represented as the sum of individual energy contributions between pairs of atoms. Next, the equations of motion given in Equation (1.73) are solved,

$$F_i(\vec{r}_1,\vec{r}_2,\vec{r}_3,\ldots,\vec{r}_n) = m_i \frac{d^2\vec{r}_i(t)}{dt^2}, \qquad i=1, 2, 3,\ldots,n \tag{1.73}$$

where n is the number of particles, $\vec{r}_i(t) = (x_i(t),y_i(t),z_i(t))$ is the position vector of the i^{th} particle, F_i is the total force acting on i^{th} particle at time t, and m_i is the mass of the particle.

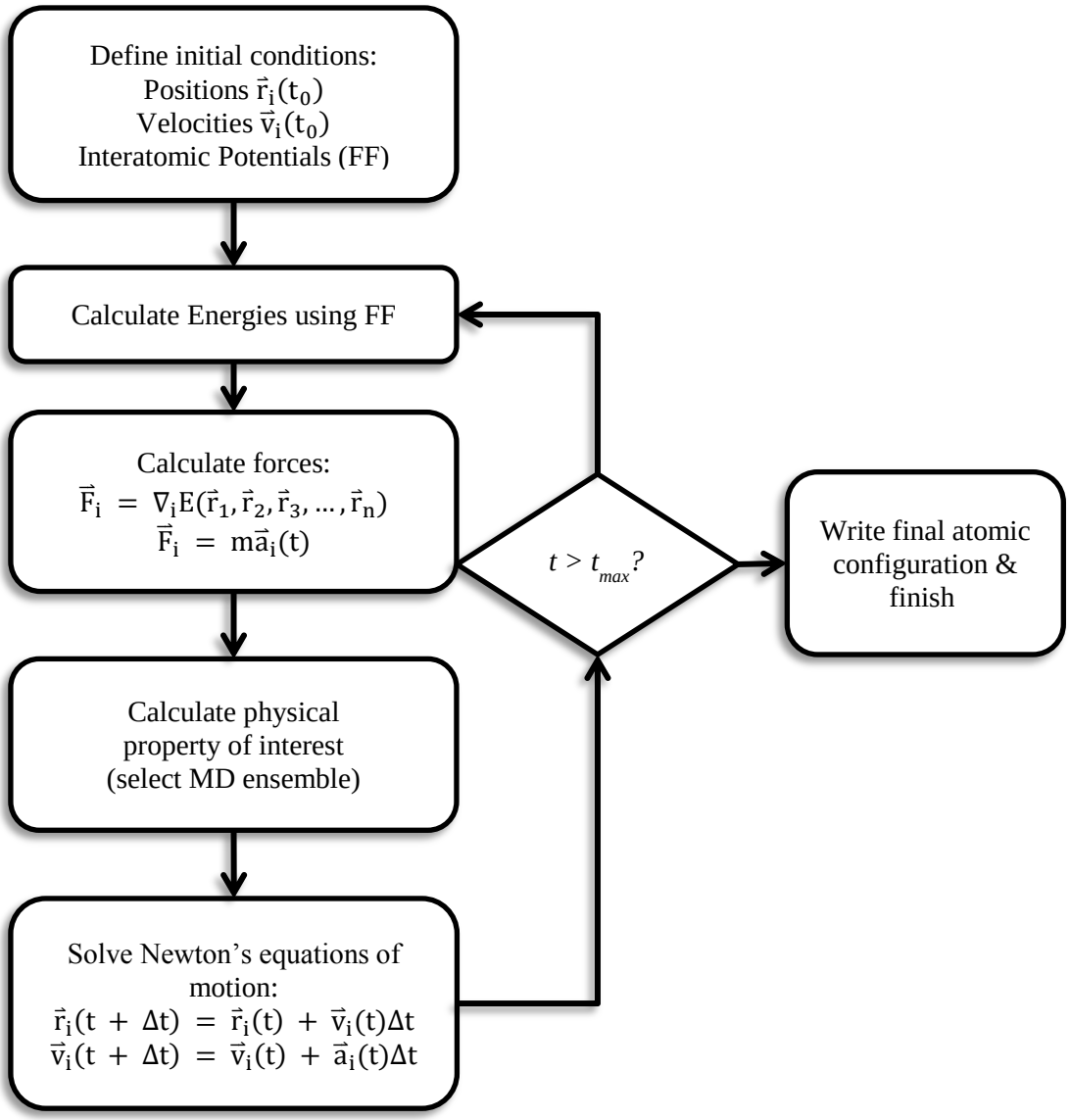

Figure 1.5. General procedure for molecular dynamics simulation.

2. ELECTRON TRANSFER THROUGH SEI LAYERS FORMED ON SI ANODES OF LI-ION BATTERIES*

2.1. Synopsis

A solid electrolyte interphase (SEI) film is formed at the surface of Li ion batteries during the first charging cycles. This film results from the electron transfer that occurs from the electrolyte to the anode, from electron leakage that occurs from the anode to the electrolyte, and from the further reduction and oxidation of the electrolyte. This film grows from a few nanometers to a few hundred nanometers and consists of both inorganic and organic products. In this paper, a combined density functional theory and Green's function approach (DFT-GF) is used to study the electron transfer through model systems consisting of electrode, SEI layer and electrolyte. In this preliminary analysis, four degrees of lithiation are modeled for the electrode, the SEI film consists of LiF or Li_2O, and the electrolyte is ethylene carbonate. Results showed a significant reduction of the electron transport when the SEI film is present and a very small finite current was still found at 1 nm thicknesses.

2.2. Introduction

In this section a novel approach to evaluate electron transfer through composite interfacial films is utilized. The reported atomistic simulations focus on the electron

*Reprinted with permission from:
Electron Transfer Through SEI layers Formed on Si Anodes of Li-ion Batteries by L. Benitez, D. Cristancho, J. M. Seminario, J. M. Martinez de la Hoz, P. B. Balbuena, 2014. *Electrochim. Acta*, 140, 250-257, Copyright 2014 by Elsevier.

transfer events during SEI growth. First, the model composite films are introduced and then the electron currents through such systems are evaluated.

The results of this study provide insights in two important issues: 1) how the SEI initially forms on Si anodes; and 2) how the SEI may grow based on the electron conductivity measured in the SEI compounds (LiF and Li_2O).

2.3. Methodology

Figure 2.1 illustrates the general system investigated. The model investigated consists of a small cluster of the Li_xSi_y electrode, a finite model of the SEI layer, and a molecule of the electrolyte. This electrolyte layer may contain solvents, salts and/or additives. Then an external voltage is applied to the two gold nanoelectrodes thus recreating the leakage current that would occur during the charge of the battery. The SEI components studied in this paper are LiF and Li_2O, and the electrolyte is ethylene carbonate (EC). The studied systems are discussed in next section.

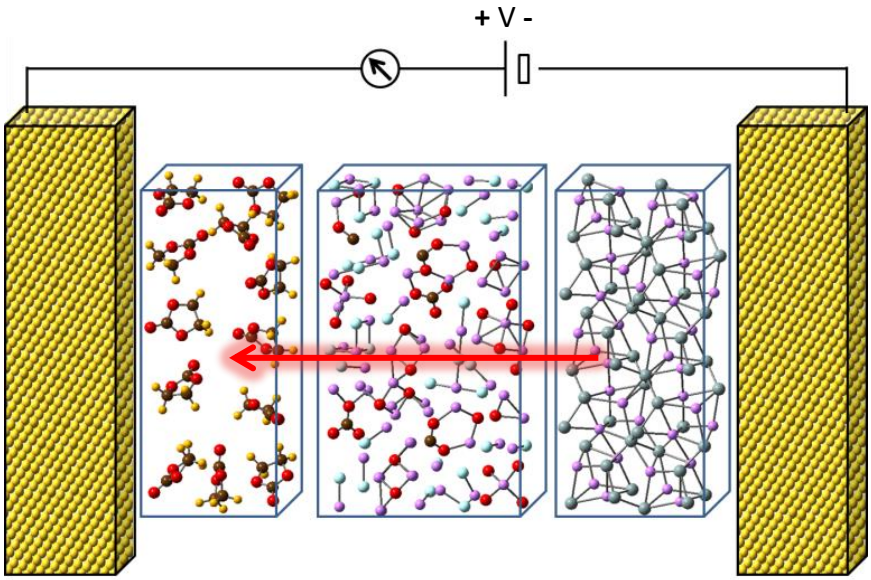

Figure 2.1. The studied model represents a portion of the interface formed by the electrolyte/SEI/Li_xSi_y electrode. A voltage is applied through the gold nano-contacts, which are coupled to both ends of the composite interface. The red arrow indicates the direction of electron leakage flow during the nucleation and growth of the SEI film.

First, geometry optimizations are performed in each component of the Li_xSi_y-SEI-EC models attached to gold nanoelectrodes. Silicon clusters (Si_{22}) are optimized using B3PW91/6-31G(*d)* level of theory,[132] and B3PW91/3-21G is used to optimize LiSi and Li_{22} clusters. Molecular geometries for the SEI molecules, LiF and Li_2O, are obtained from the Inorganic Crystal Structure Database (ICSD) (http://icsd.fiz-karlsruhe.de/icsd/)[133] and are positioned between the model anode and one molecule of the electrolyte (EC). Gold atoms representing the nanocontacts for the I-V measurement apparatus are located at each side of the Li_xSi_y-SEI-EC system. In nano-scale systems the effects of the measuring device must be accounted for, therefore the addition of the gold atoms as well as the bulk gold density of states (DOS) information is very

important. Once the model is assembled, single point (SP) self-consistent field (SCF) calculations are performed to get the Hamiltonian matrix needed to compute the current as explained in Section 1.4.2 of this document. All the DFT calculations are performed using the program Gaussian 09.[134] Then the IV curves are obtained using the help of the program GENIP.[135] This method has been used previously to obtain I-V characteristics of polypeptides in alpha-helix conformation,[136] nanosensors for fissile materials,[137] cobalt phthalocyanine complexes,[138] oligoglycines[139] and molecular biosensors,[140] among others. The density of states for the gold nano-contacts is obtained using the program CRYSTAL,[141-143] which uses ab initio DFT calculations on a periodic system of bulk gold. Then the leakage currents are found using the Landauer equation,[144-148] as described in in Section 1.4.2.

2.4. Results and Discussion

The SEI layers are represented by a cluster composed of Li_2O or LiF. Three lithiated cases for the anode are investigated: Si_{22}, $Si_{11}Li_{11}$, and Li_{22}. The electrolyte is represented by a molecule of ethylene carbonate (EC). Calculations are done for various thicknesses and configurations of the SEI layer. Then gold atoms are attached at both ends of the EC-SEI-Li_xSi_y system and an external voltage is applied to it in order to calculate the leakage current using the DFT-GF approach implemented in the GENIP program. Optimized anode structures are located in an interfacial arrangement together with a model of the SEI layer represented by either Li_2O, $(Li_2O)_2$, and $(Li_2O)_3$, or by LiF, $(LiF)_2$ and $(LiF)_3$ respectively. Two separate configurations are analyzed: 1) SEI molecules (Li_2O and LiF) connected through chemical bonds, and 2) SEI molecules

separated at Van der Waals distances in order to simulate initial nucleation stages. These configurations are based on AIMD observations[52] that show that LiF fragments, instead of LiF crystals, are found at the initial stages of LiF formation in the SEI. The current-voltage (I-V) characteristics in all cases are calculated for applied voltages in the range of -5 V to 5 V, but as indicated in Figure 2.1 the electron leakage of interest results from the positive voltages.

Figures 2.2, 2.3 and 2.4 present the I-V curves resulting from adding Li_2O units between the Li_xSi_y electrode and the electrolyte. Each figure shows the EC-$(Li_2O)_x$-Li_xSi_y systems with (Li_2O), $(Li_2O)_2$ and $(Li_2O)_3$ in red, green and blue respectively. In addition, the EC-Li_xSi_y systems (without Li_2O) are shown in black. First, the nature of the electrode can be analyzed by noting the difference in current magnitude in the various compositions of Li_xSi_y anode; the maximum currents, observed at around 5V, are ~1.5 μA in the Si electrode (Figures 2.2), ~12 μA in the LiSi electrode (Figure 2.3), and ~15 μA in the Li electrode (Figure 2.4). Secondly, by comparing the two SEI bonding configurations represented in each figure, it can be observed in all three electrode cases that the bonded SEI arrangements yield higher currents which indicate higher electron transfer than the non-bonded cases. Finally, in all three Li_xSi_y electrode cases, the current is greatly reduced by adding the SEI components as compared with the systems without any SEI film (see black curves and insets), thus indicating that the presence of the SEI film creates a clear resistance to electron transfer. This result agrees with the generally accepted idea that the SEI layer blocks electron transfer.[149] Moreover

increasing the width of the SEI layer reduces the electron transfer even more in all modeled electrodes.

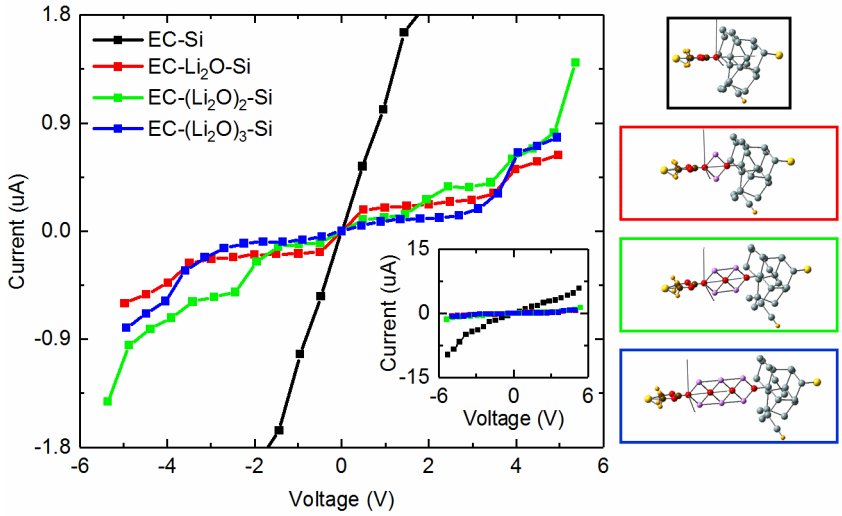

(a)

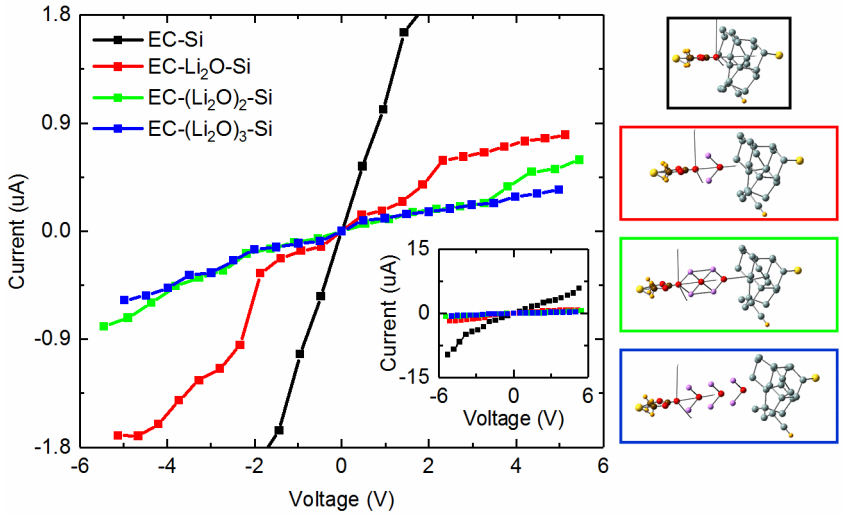

(b)

Figure 2.2. Current-voltage curves obtained for electron transport through Li_2O (red), $(Li_2O)_2$ (green), and $(Li_2O)_3$ (blue) in two different configurations between the EC molecule and the model Si electrode. (a) Units attached via chemical bonds. (b) Units separated by Van der Waals distances. The inset includes the current-voltage result (black) for the system EC/Si electrode. Note the change of scale of the inset.

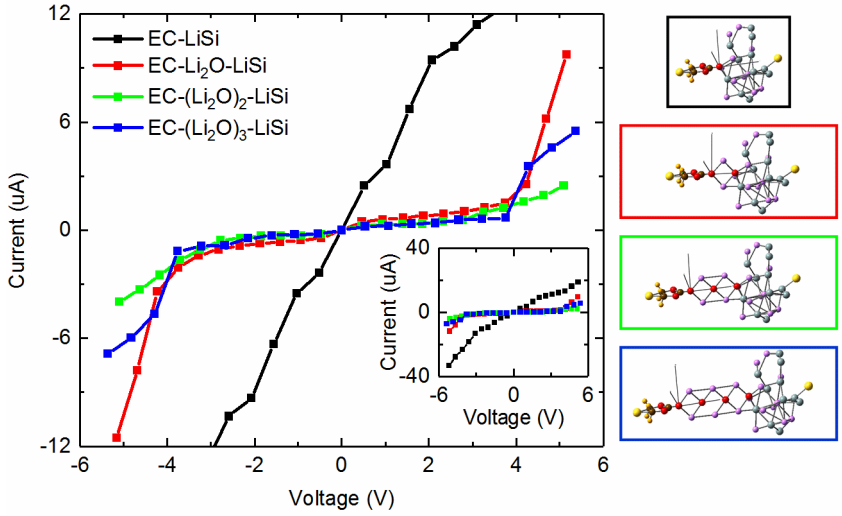

(a)

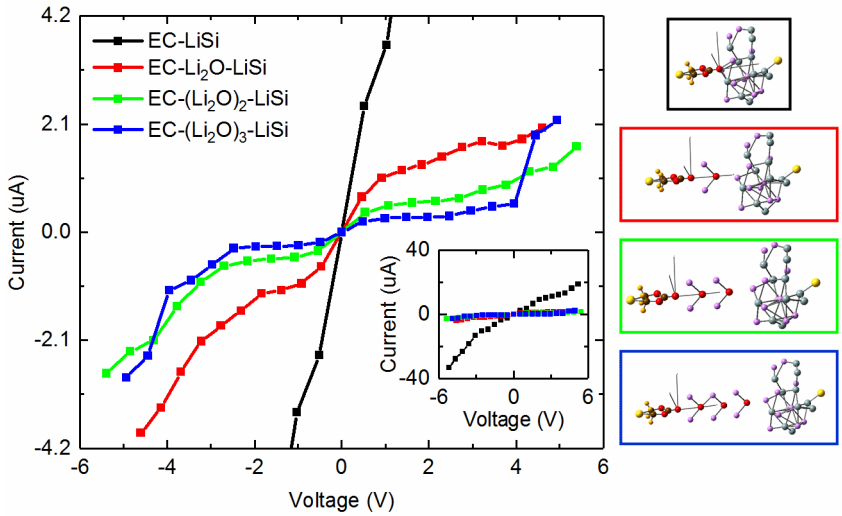

(b)

Figure 2.3. Current-voltage curves obtained for electron transport through Li_2O (red), $(Li_2O)_2$ (green), and $(Li_2O)_3$ (blue) in two different configurations between the EC molecule and the model LiSi electrode. (a) Units attached via chemical bonds. (b) Units separated by Van der Waals distances. The inset includes the current-voltage result (black) for the system EC/LiSi electrode. Note the change of scale of the inset.

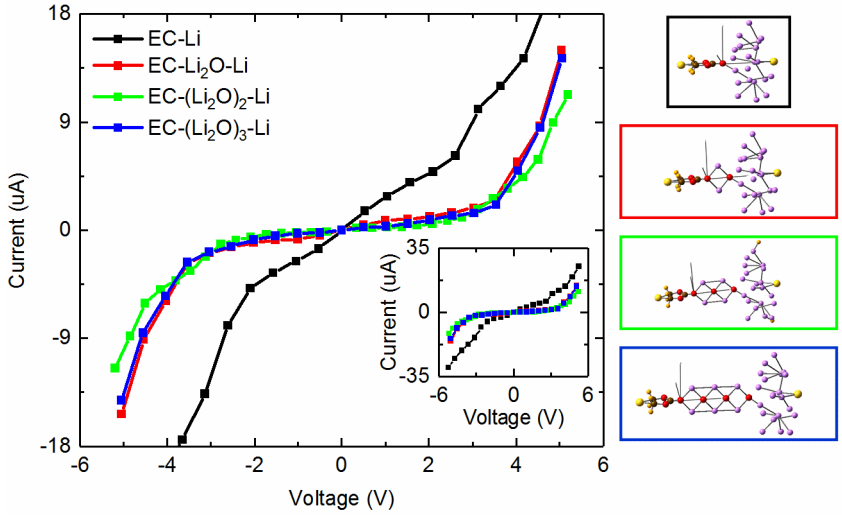

(a)

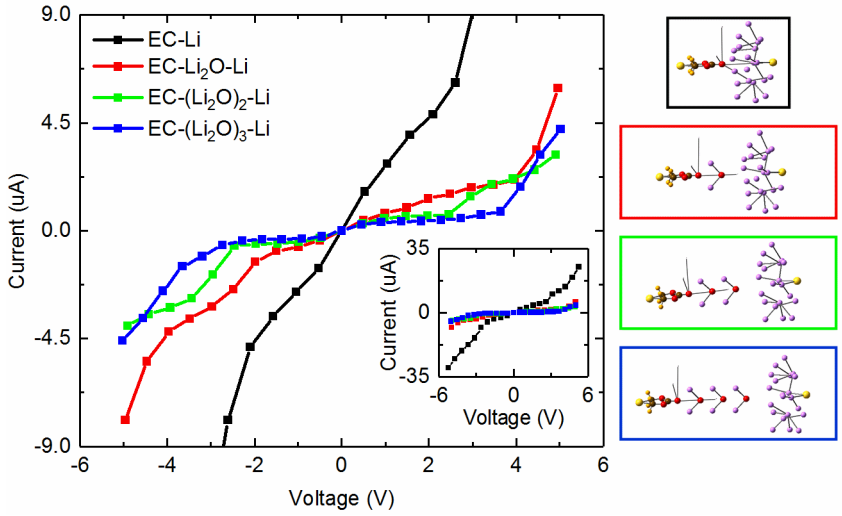

(b)

Figure 2.4. Current-voltage curves obtained for electron transport through Li_2O (red), $(Li_2O)_2$ (green), and $(Li_2O)_3$ (blue) in two different configurations between the EC molecule and the model Li electrode. (a) Units attached via chemical bonds. (b) Units separated by Van der Waals distances. The inset includes the current-voltage result (black) for the system EC/Li electrode. Note the change of scale of the inset.

Similarly, Figures 2.5, 2.6 and 2.7 present the I-V curves resulting from adding LiF units between the Li_xSi_y electrode and the electrolyte. Again, each figure shows the

EC-$(LiF)_x$-Li_xSi_y systems with (LiF), $(LiF)_2$ and $(LiF)_3$ in red, green and blue respectively. In addition, the EC-Li_xSi_y systems (without LiF) are shown in black. Also, the effects of the nature of the electrode can be noted by comparing the maximum currents in each Li_xSi_y anode case. At ~5 V, in the Si electrode, the maximum current is ~0.45 μA whereas in LiSi and Li electrodes the maximum currents are 2 μA and 3 μA, respectively. These values are much smaller than the ones found in Li_2O cases thus indicating that at this voltage, Li_2O has a much less resistance to electron transfer compared to LiF. Comparing the SEI bonding configurations in each figure, it can be observed that in all bonded cases the currents are more than twice of the currents in the non-bonded configurations. Lastly, in all three model Li_xSi_y electrode cases, the current is greatly reduced by adding the LiF components as compared with the systems without any SEI film (see black curves and insets); current reductions more than one order of magnitude are observed at about 5V in all cases. Moreover increasing the width of the SEI layer also reduces the electron transfer in all modeled electrodes.

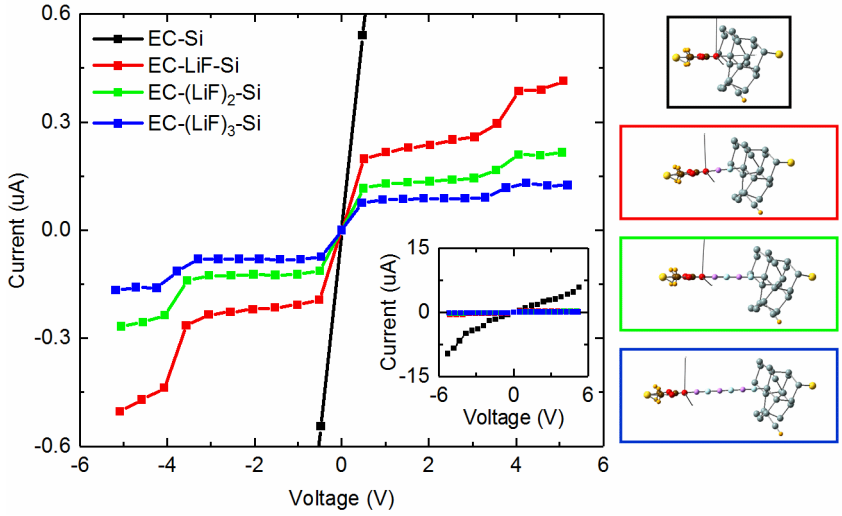

(a)

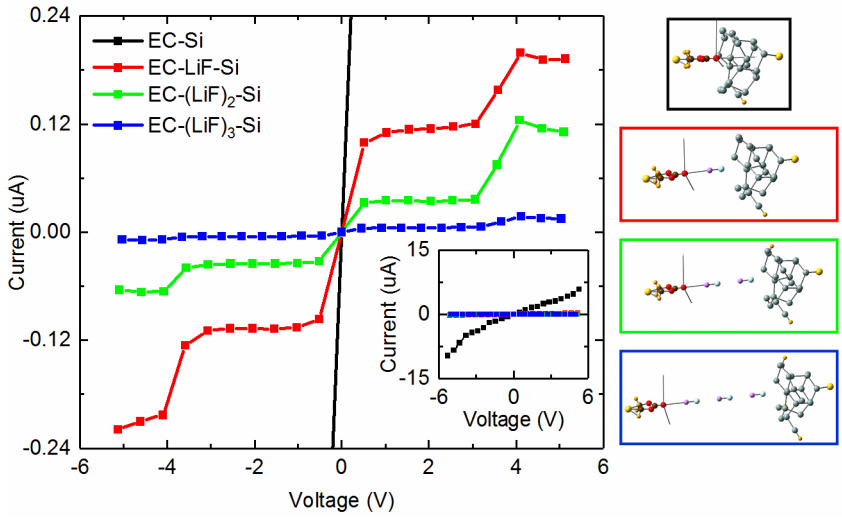

(b)

Figure 2.5. Current-voltage curves obtained for electron transport through LiF (red), $(LiF)_2$ (green), and $(LiF)_3$ (blue) in two different configurations between the EC molecule and the model Si electrode. (a) LiF units attached via chemical bonds forming a linear chain. (b) LiF units separated by Van der Waals distances. The inset includes the current-voltage result (black) for the system EC/Si electrode. Note the change of scale of the inset.

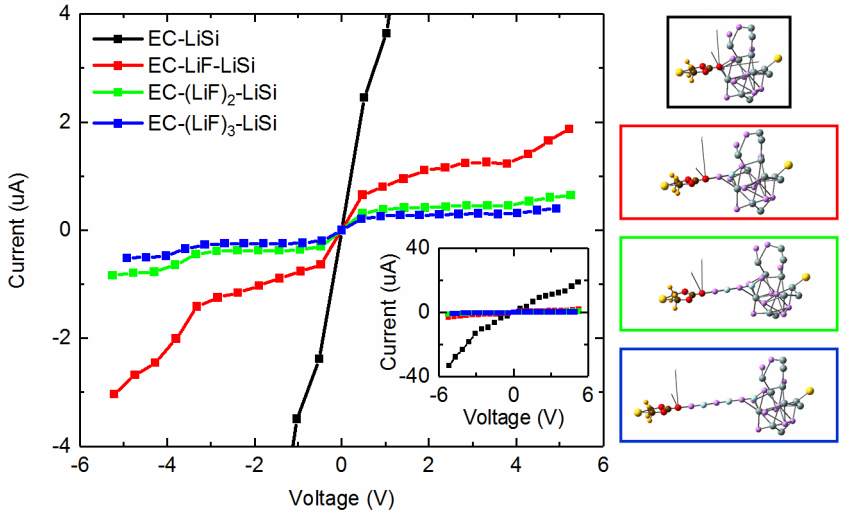

(a)

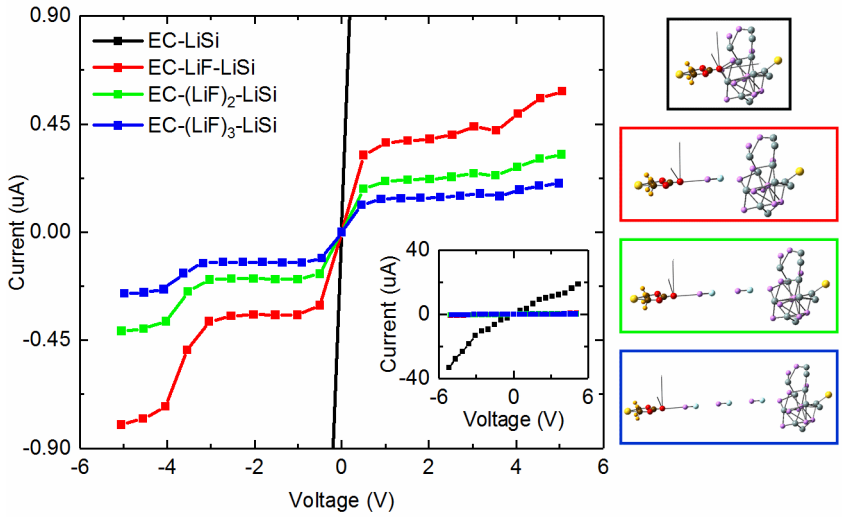

(b)

Figure 2.6. Current-voltage curves obtained for electron transport through LiF (red), $(LiF)_2$ (green), and $(LiF)_3$ (blue) in two different configurations between the EC molecule and the model LiSi electrode. (a) LiF units attached via chemical bonds forming a linear chain. (b) LiF units separated by Van der Waals distances. The inset includes the current-voltage result (black) for the system EC/LiSi electrode. Note the change of scale of the inset.

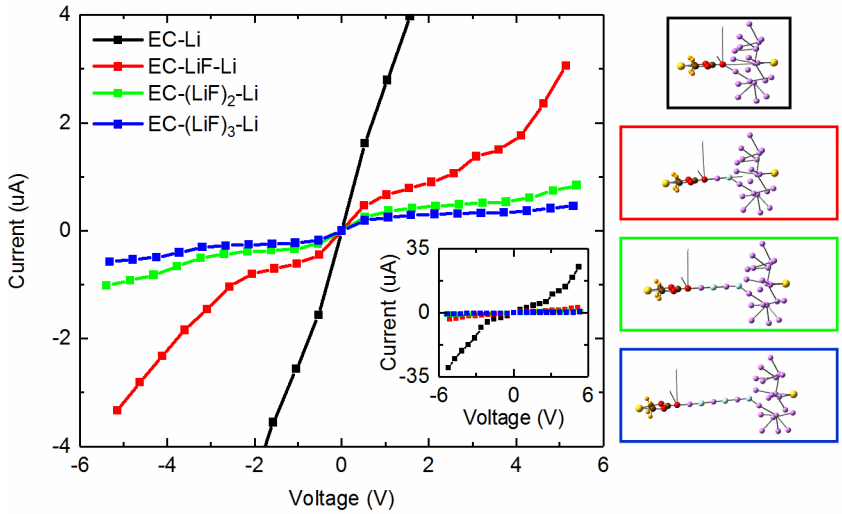

(a)

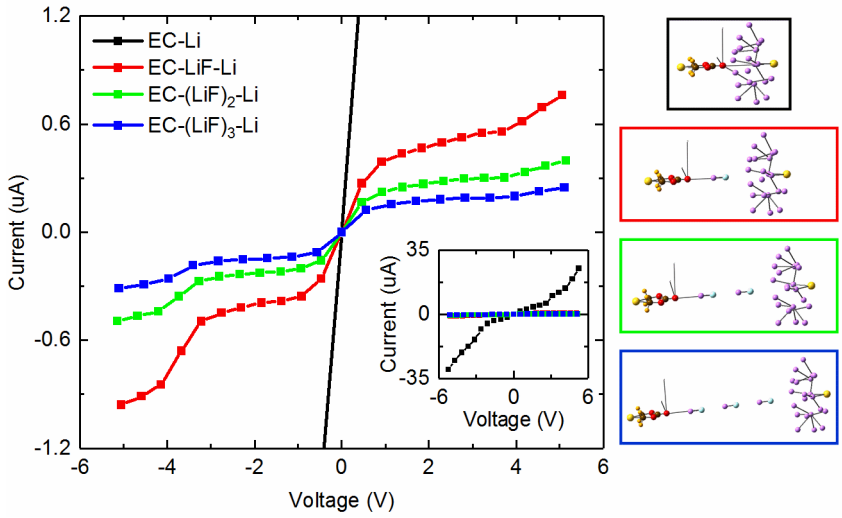

(b)

Figure 2.7. Current-voltage curves obtained for electron transport through LiF (red), $(LiF)_2$ (green), and $(LiF)_3$ (blue) in two different configurations between the EC molecule and the model Li electrode. (a) Units attached via chemical bonds forming a linear chain. (b) Units separated by Van der Waals distances. The inset includes the current-voltage result (black) for the system EC/Li electrode.

In order to analyze how the SEI thickness affects the transfer of electrons the electron current through the systems as a function of SEI thickness is calculated. The

current at 2 V versus SEI thickness for Li_2O and LIF systems is shown in Figure 2.8. The results are fitted to a function given by $f(x) = p_1.exp(-x/p_2) + p_{3+} p_4 x$, where x is the thickness of the SEI in Å and p_4 is found ~0. The current decreases rapidly as the SEI film thickness increases due to the addition of molecules. In both Li_2O and LiF cases, the current approaches zero at ~3 Å in the Si electrode (p_3 = ~0). In the lithiated cases, both in LiSi and in Li, the current approaches to zero at ~8 Å in Li_2O and ~10 Å with in LiF. This result implies that a lower electron transfer may continue even when the SEI film thickness becomes large (20-100 nm).

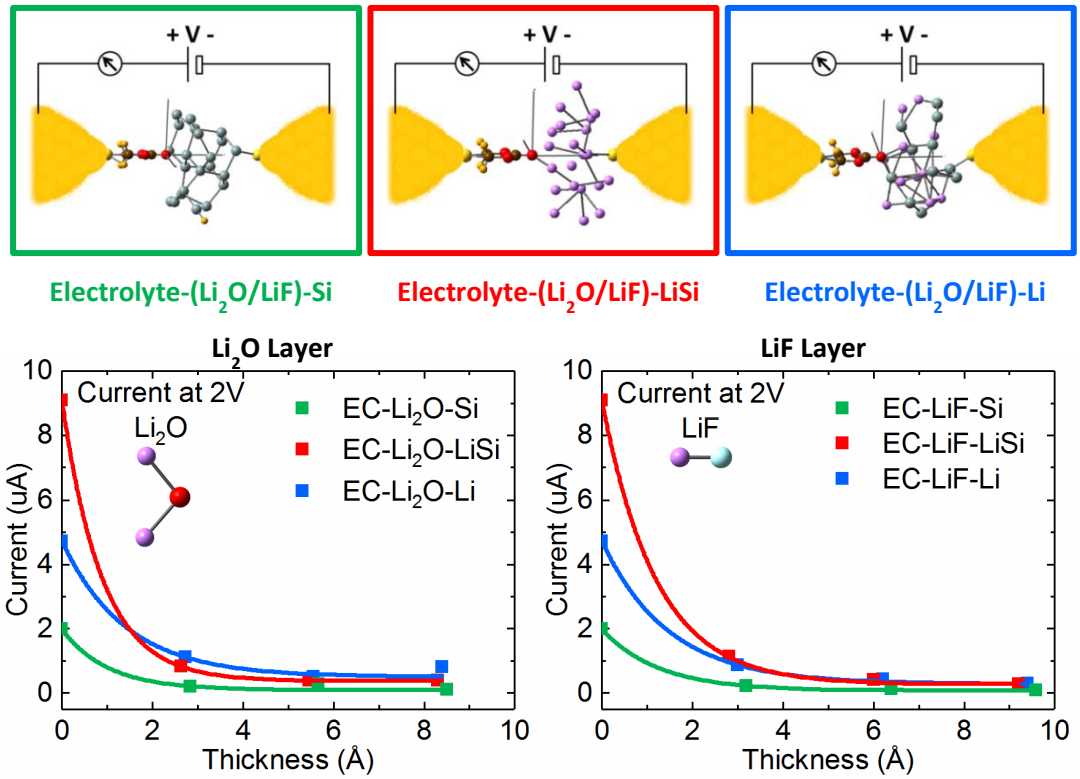

Figure 2.8. Calculated current at 2V as a function of the SEI layer thickness (Li_2O and LiF). The calculated points are well correlated with an exponential function. The colors of the curves correspond to those used in the schemes on top describing each system.

2.5. Conclusions

A novel first-principles computational approach was used to characterize the electron transfer through two model composite interfacial systems: EC-$(LiF)_x$-Li_xSi_y and EC-$(Li_2O)_x$-Li_xSi_y. Three degrees of lithiation for the electrode were studied: Si, LiSi, and Li. Based on structures obtained from AIMD simulations,[52] model SEI layers made of LiF fragments are arranged in various thicknesses and configurations, and by analogy, Li_2O model films are also built. It was found that at high voltages of ~5, Li_2O films allow a higher electron transfer than LiF films. It was also found that separating the fragments at Van der Waals distances results in lower currents, thus implying lower electron transfer rates. Moreover, increasing the thickness of the SEI layer reduces the electron transfer as well; yet, a finite small current is still found even at large film thicknesses.

3. ELECTRON TRANSPORT AND ELECTROLYTE REDUCTION IN THE SOLID-ELECTROLYTE INTERPHASE OF RECHARGEABLE LITHIUM ION BATTERIES WITH SILICON ANODES*

3.1. Synopsis

Understanding the molecular processes that lead to the formation, structure, and transport properties of the solid electrolyte interphase (SEI) found in lithium ion batteries with silicon anodes is of paramount importance for the development of lithium-ion batteries (LIB) capable of performing under the extreme exigencies of our present energy needs that are solved presently with nonrenewable energies. A combined density functional theory (DFT) and Green's function approach (DFT-GF) is used to study the electron transport characteristics in selected finite models of materials formed at the SEI located between the silicon surface of the anode of Li-ion batteries and the electrolyte solvent. The SEI products examined are lithium carbonate ($LiCO_3$) silicon oxide (SiO_2) and lithium disilicate ($Li_2Si_2O_5$). Results show that the leakage of electrons from the Si anode to the solvent is greatly reduced (up to 4 orders of magnitude) with the addition and growth of the SEI components as compared with the solvent-anode sample where no SEI is present. Moreover, it is found that at a charging voltage of 2 V, the electron leakage current decays exponentially with the length, decaying up to three orders of

*Reprinted with permission from:
Electron Transport and Electrolyte Reduction in the Solid-Electrolyte Interphase of Rechargeable Lithium Ion Batteries with Silicon Anodes by L. Benitez and J. M. Seminario, 2016. *J. Phys. Chem. C*, 120, 17978-17988, Copyright 2016 by American Chemical Society.

magnitude at about 30 Å in Li_2CO_3, two orders of magnitude at about 16 Å in SiO_2, and up to three orders of magnitude at about 47 Å in $Li_2Si_2O_5$. Additionally, the HOMO-LUMO gap shortens as the SEI layer thickness increases. An estimate of the change in current associated with energy changes using the Heisenberg uncertainty principle yields currents in the range of 10^{-4} A. Electron transport results provide particular details on the SEI layer formation and growth. A 100% Si cluster yields the largest resistance to electron transport, when compared to the lithiated electrodes modeled by $Li_{13}Si_4$ and LiSi clusters. It is also found that Li_2CO_3 is electrically more insulating than LiF and Li_2O. A high electron transfer at the initial stages of SEI formation and then significantly lower transfer yielding a progressively smaller growth of the SEI was found as well.

3.2. Introduction

While some studies have concentrated on describing and calculating ionic conduction,[63] ion diffusion,[150] or tunneling barriers,[38] minimal efforts have been put toward studying electron transport and predicting electron leakage current in the individual interphase components. Moreover, experiments in single molecules or in fragments of a crystal are understandably difficult and are not easily reproducible. For that reason, alternative methods are needed to compare and validate theoretical and experimental results. In this section, first the DFT-GF approach is used to characterize the electron transfer through Li_2CO_3, Si_2O and $Li_2Si_2O_5$. Moreover, a simple and direct method to calculate electron currents from readily available electrolyte decomposition energies found in the literature is used. Since multiple investigations have focused on understanding reactions at the electrolyte/electrode interface, including oxidation and

reduction of the electrolyte, there is a substantial amount of information on reduction energies.[33, 53, 151-157] Most these decomposition processes can be summarized into one electron (1*e*) and two electron (2*e*) mechanisms.[152-154, 157-158] In a recent study, Ma et al. studied the decomposition mechanisms of ethylene carbonate (EC) and fluoroethylene carbonate (FEC) on Si clusters at ultralow degrees of lithiation ($LiSi_{15}$ and Li_2Si_{15}) using density functional theory.[153] On an earlier investigation, Vollmer et al.[157] used DFT to calculate reduction potentials for EC, propylene carbonate (PC), and vinylethylene carbonate (VEC). Preliminary results of electron transport in LiF and Li_2O using the DFT-GF approach showed a significant reduction of the electron transport when the SEI is present and a very small finite current was still calculated at 1 nm thickness.[52]

The results of this study provide insights in two issues: 1) how the SEI initially forms and how it evolves, and 2) how it becomes stable under certain conditions.

3.3. Methodology

As shown in Figure 3.1, the systems investigated are composed of the electrolyte solution, the interphase, and the Li_xSi_y anode. In order to calculate the rate of electrons traveling from the Si_xLi_y clusters to the electrolyte molecule passing through the interphase, an external voltage is applied to the electrolyte-interphase-Li_xSi_y complex using an external power supply connected to the complex through two nanoelectrodes. The samples investigated include a molecule of the electrolyte (ethylene carbonate), a finite model of SEI or oxide layer (Li_2CO_3, SiO_2, or $Li_2Si_2O_5$), and a small cluster of the Li_xSi_y anode. The program GENIP[127, 136, 159-160] is then used to calculate the electron rates

through the complex. Four lithiated cases for the anode are investigated: Li, $Li_{13}Si_4$, LiSi and Si.

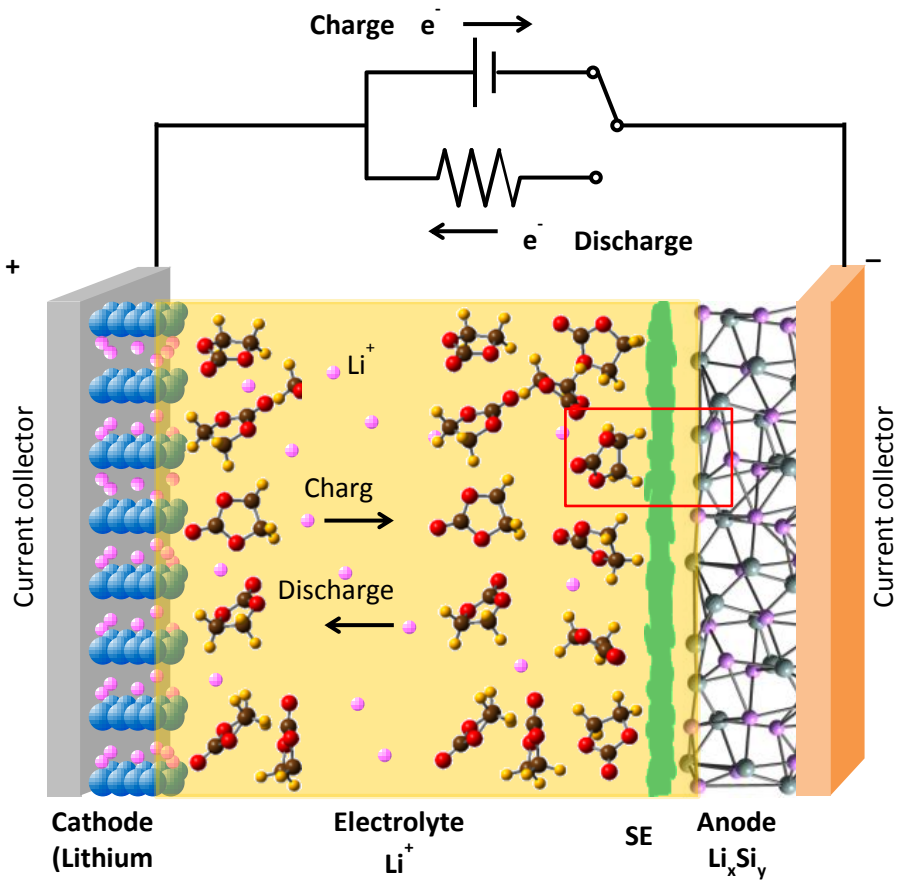

Figure 3.1. Lithium-ion battery diagram showing the sample of the EC-interphase-LiSi complex (red square) where the electron leakage rates during charge are calculated.

The first systems modeled are the configurations without any SEI component between the electrolyte and the Li_xSi_y anode as shown in Figure 3.2. The electrolyte considered in this investigation is ethylene carbonate (EC), the SEI product examined is

lithium carbonate (Li_2CO_3), and the oxides assessed are silicon oxide (SiO_2) and lithium disilicate ($Li_2Si_2O_5$).

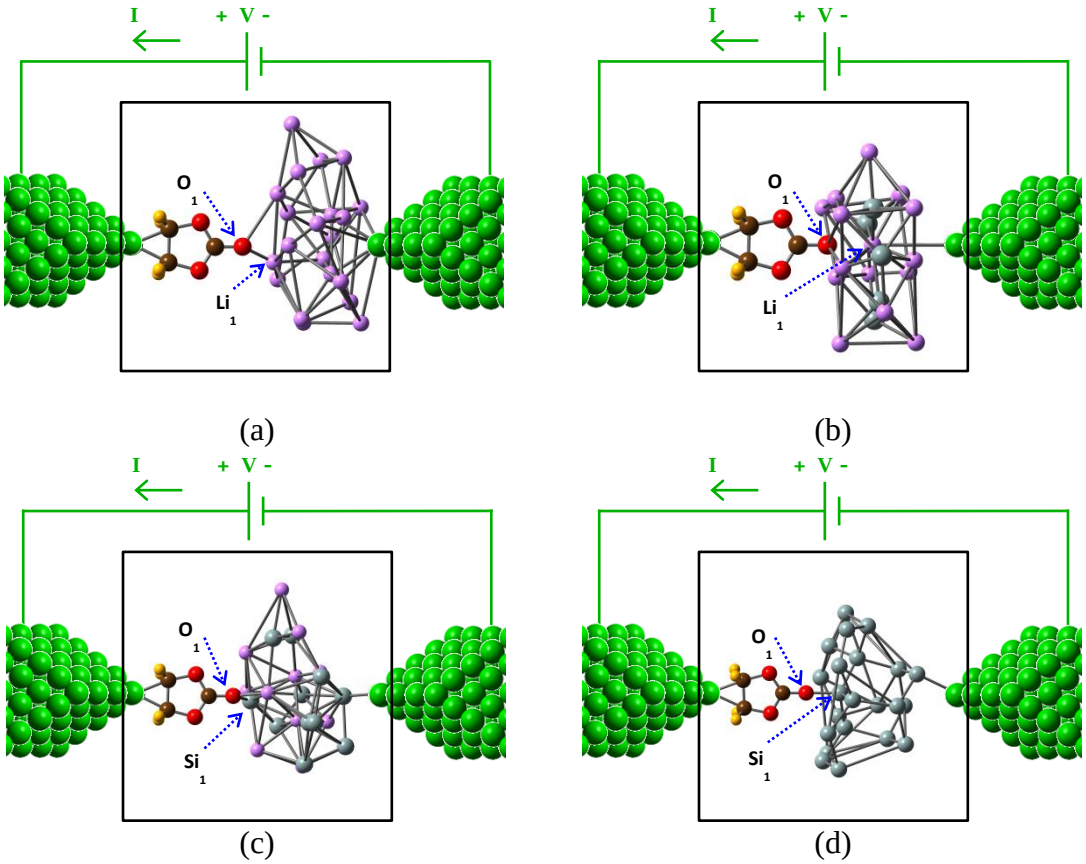

Figure 3.2. Models without SEI layer (electrolyte-Li_xSi_y) for four Li_xSi_y stoichiometries (a) Li, (b) $Li_{13}Si_4$, (c) LiSi and (d) Si attached to nano-gold electrodes in order to calculate electron transfer rates. For all other cases with SEI layer, pieces of the SEI containing from 1 to 3 units shown in Figure 3.3 are positioned between the EC and the Li_xSi_y anode. The nanoelectrodes constitute the source and drain of electrons for the calculations. Discrete part (inside black square) and the extended nano-contacts (outside black square) are solved together using the GENIP, DFT-Green's functions approach. Li (purple), Si (gray), O (red), H (yellow), C (brown) and Au (green).

The chemical structures for all molecules studied are illustrated in Figure 3.3. Calculations are done for various thicknesses of the SEI layer. The increase of the thickness is represented by the addition of SEI molecules between the electrolyte (EC) and the anode cluster (Li_xSi_y). Up to 3 molecules or units of the SEI are added in each case. Each molecule in all the models is separated at van der Waals distances to simulate initial nucleation stages.[52]

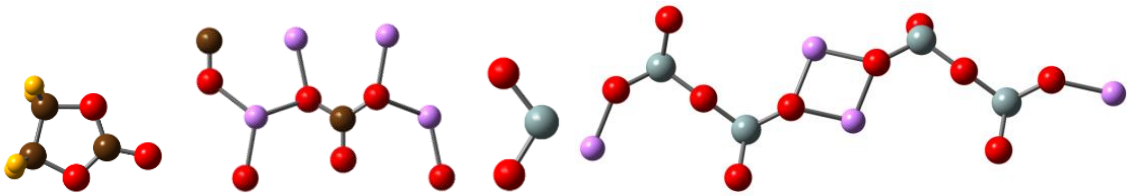

(a) (b) (c) (d)

Figure 3.3. Chemical units (structures) of SEI products and oxides analyzed using DFT (a) EC, (b) Li_2CO_3, (c) SiO_2, and (d) $Li_2Si_2O_5$. EC is the acceptor of leaking electrons from the anode and all the others represent SEI layers containing from 1 to 3 units. Li (purple), Si (gray), O (red), H (yellow), C (brown).

Within the DFT-GF method, the quantum-mechanical calculations on the extended molecule and the density of states (DOS) of each nano-contact bulk material are needed. Then GENIP (Generalized Electron Nano-Interface Program), which combines the results of the DFT calculations with the GF formalism, is used to calculate the current-voltage characteristics (quantum ammeter) of all systems. This method has been previously used to calculate the I-V characteristics of cobalt phthalocyanine complexes,[159] oligoglycines,[139] molecular biosensors,[140] etc. Details for GENIP can be

found in previous works.[127, 161-164] First, geometry optimizations are performed in each component of the EC-SEI-Li_xSi_y models attached to gold nanoelectrodes. The electrolyte molecule, EC, is optimized using B3PW91 hybrid exchange-correlation functional and the 6-311++G(d,p) basis set; preliminary Li_xSi_y clusters are optimized using smaller basis sets. The crystal structure and lattice parameters for the solid electrolyte interphase product Li_2CO_3 as well as for each oxide SiO_2 and Li_2SiO_5 are obtained from the Inorganic Crystal Structure Database (ICSD).[133] Each studied model is assembled together using van der Waals separations[165] between each component (EC, interphase and anode), and then single point (SP) calculations using B3PW91 and LANL2DZ basis set are performed using the program Gaussian 09.[134] The DOS for the gold nano-contacts is obtained from ab initio DFT calculations on a periodic system of the bulk contact material (gold) with the program CRYSTAL.[143]

A direct ab initio procedure to calculate current-voltage characteristics in molecular junctions was developed earlier by Seminario's group and used for several applications.[166-168] Other procedures also used by them are based on a Green's functions approach and the Landauer formalism.[146] In the direct approach, the I-V profiles are obtained by combining equilibrium electronic structure calculations together with the uncertainty principle. Using the energy-time uncertainty relation $\Delta E \Delta t \geq \hbar/2$, where the time it takes an electron to transfer from one molecule to another or in general from one phase to another is $\Delta t \approx (\hbar/2)(1/\Delta E)$. Since $I = \Delta Q/\Delta t$, it follows that $I \leq 2\Delta Q \Delta E/\hbar$; ΔE can be associated with the electrolyte reduction energy, and Δt with the duration of the electron transfer ($\hbar$ = reduced Planck's constant = $h/2\pi$). Thus, the currents estimated by

this procedure are upper limits to the exact values needed for the decomposition of the electrolyte solvent. They are calculated from the atomic charges (ΔQ) transferred by an external electric field from an external source used to charge the battery. If ΔQ is set to 1*e* or 2*e* for the 1-e and 2-e electrolyte reduction mechanisms, respectively, an estimated value for the anode leakage current that is needed to decompose the electrolyte can be obtained. It can then be compared with the actual current leakage due to the tunneling of electrons from the anode to the electrolyte during initial charging of the battery.

3.4. Results and Discussion

The electron transport calculations using DFT-GF are performed in each system as described previously. The current voltage (I-V) characteristics are calculated for applied voltages in the range of -5 V to 5 V; however, only the electron flow resulting from positive voltages is of interest. Figure 3.4 shows the I-V characteristics for the models with Li_2CO_3 as the SEI component; they include, EC-$(Li_2CO_3)_x$-Li_xSi_y systems with (Li_2CO_3), $(Li_2CO_3)_2$ and $(Li_2CO_3)_3$ in red, green and blue respectively. In addition, the EC- Li_xSi_y systems (without Li_2CO_3) are shown in black. It can be observed in all Li_xSi_y cases, that the current is greatly reduced with the addition of the SEI components as compared with the systems without SEI components (see black curves and insets). Current reductions up to three orders of magnitude are observed at about 5 V. Moreover, increasing the thickness of the SEI layer in LiSi and Si electrodes yields a reduction of the electron transfer. Also, a difference in current magnitude is observed in the various compositions of Li_xSi_y electrode; the maximum currents, observed at around 5V, are approximately 0.39, 0.20, 0.28 and 0.17 μA for Li, $Li_{13}Si_4$, LiSi, and Si, respectively.

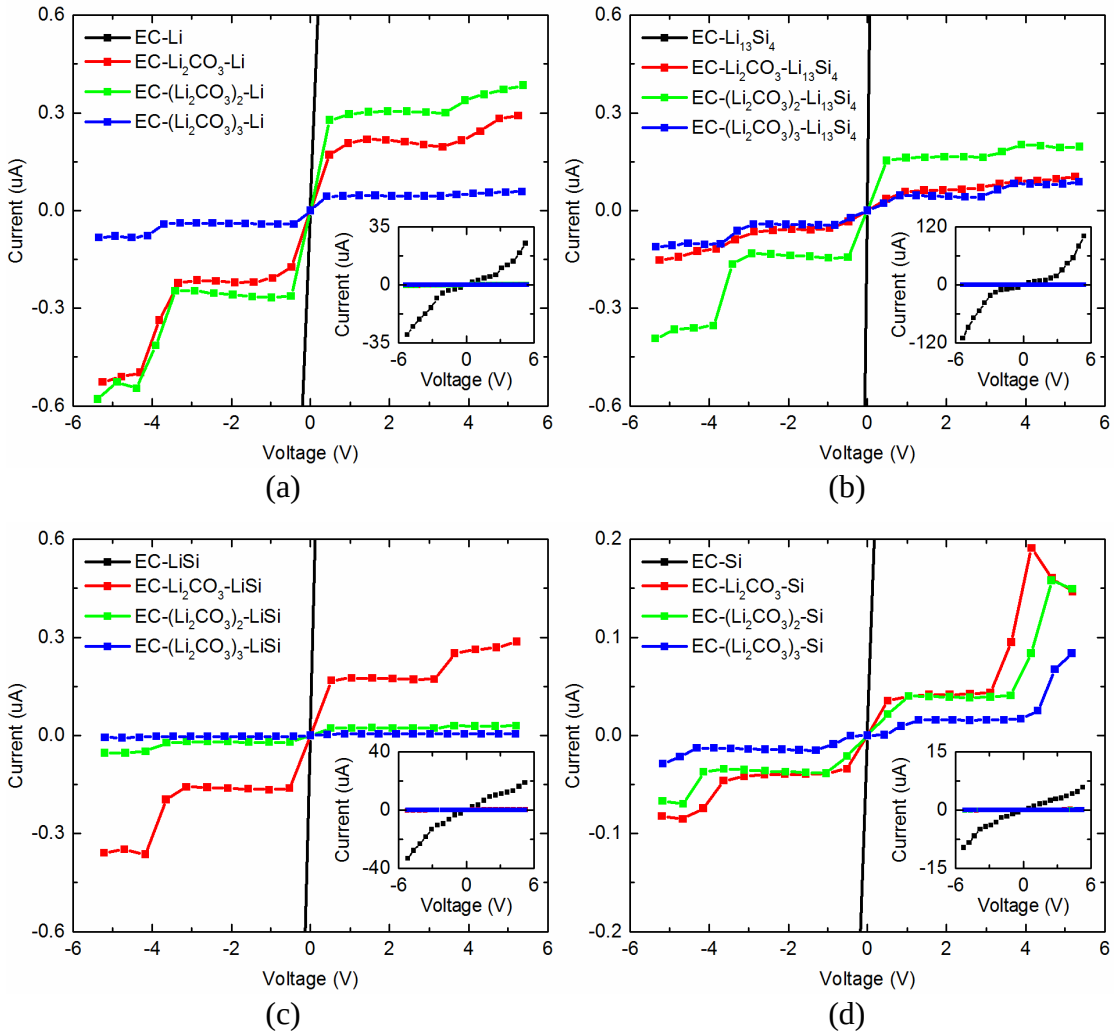

Figure 3.4. Current-voltage characteristics for electron transport through Li_2CO_3 for all Li_xSi_y clusters. (a) LiF electrode, (b) $Li_{13}Si_4$ electrode, (c) LiSi electrode, (d) Si electrode. Inset shows results (black) of EC- Li_xSi_y systems without the SEI layer.

Similar calculations are done for the oxides; Figure 3.5 shows the I-V characteristics for the models with SiO_2, including the I-V curves for the EC-$(SiO_2)_x$-Li_xSi_y systems with (SiO_2), $(SiO_2)_2$ and $(SiO_2)_3$ in red, green, and blue, respectively. In addition, the EC- Li_xSi_y systems (without SiO_2) are shown in black.

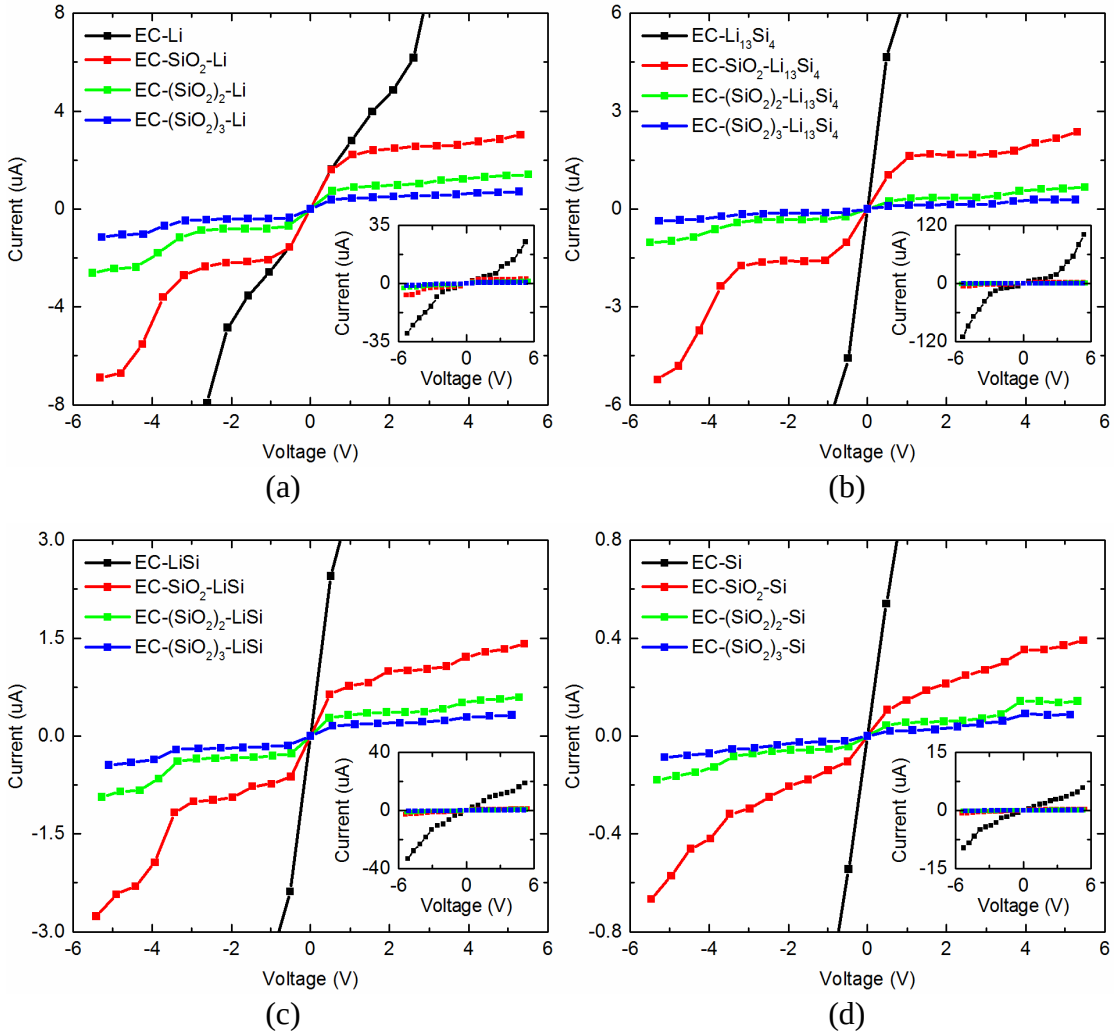

Figure 3.5. Current-voltage curves for electron transport through SiO_2 for all Li_xSi_y clusters. (a) LiF electrode, (b) $Li_{13}Si_4$ electrode, (c) LiSi electrode, (d) Si electrode. Inset shows results (black) of EC- Li_xSi_y systems without the SEI layer.

All the results for $Li_2Si_2O_5$ are in Figure 3.6. Similarly, for both SiO_2 and $Li_2Si_2O_5$, in all Li_xSi_y cases, the current is greatly reduced with the addition of the SEI components as compared with the systems without SEI components (black curves and insets). Current reductions up to two and three orders of magnitude are observed at about 5V in SiO_2 and $Li_2Si_2O_5$, respectively. Moreover, increasing the thickness of the SEI

layer also results, in most cases in a reduction of the electron transfer. The reason for the few cases when the current increases as the SEI increases in length is explained by the behavior of the HOMO-LUMO gap (HLG), which decreases as the length of the molecule increases. A decrease on the HLG (results discussed below) implies an increase in current.[169]

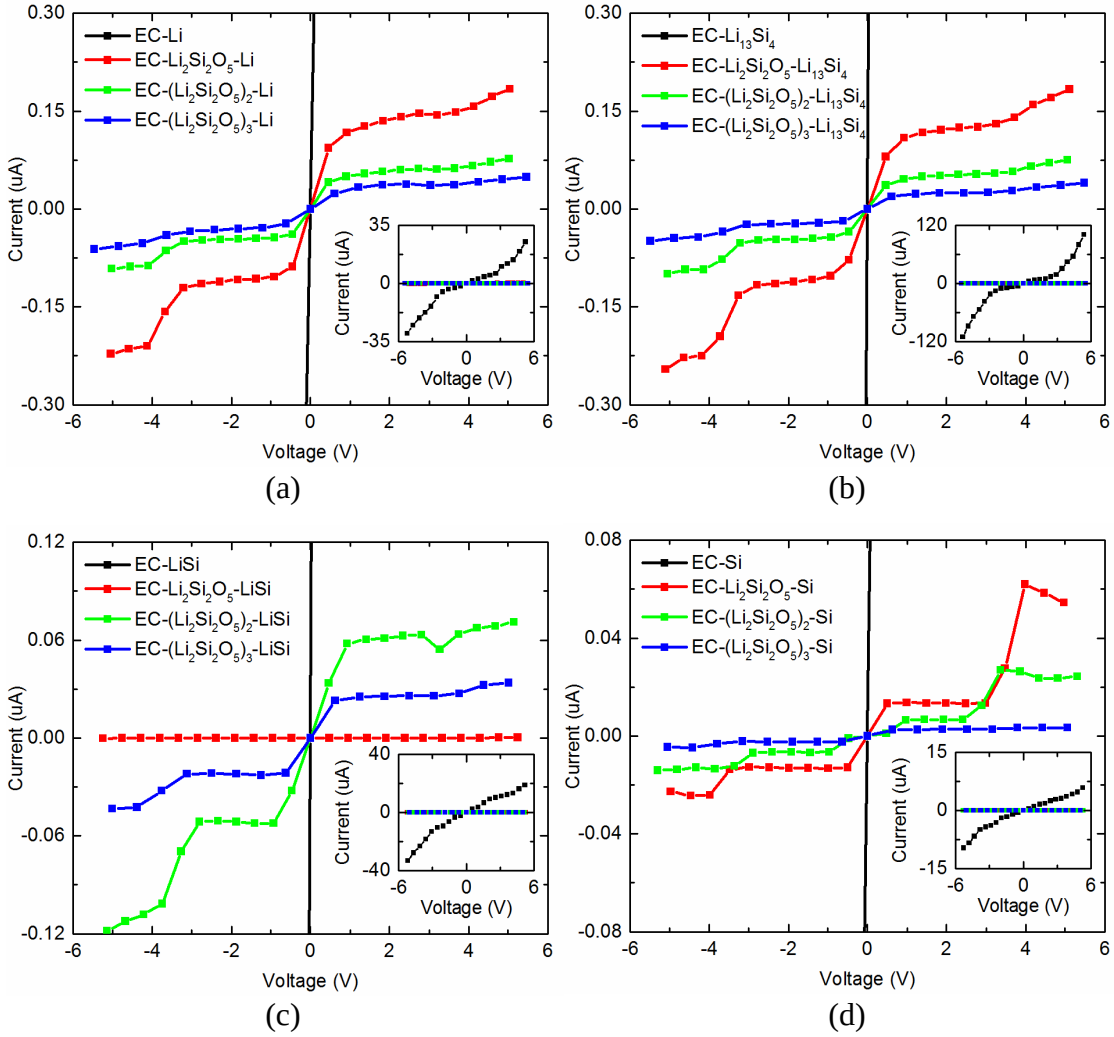

Figure 3.6. Current-voltage curves for electron transport through $Li_2Si_2O_5$ for all Li_xSi_y clusters. (a) LiF electrode, (b) $Li_{13}Si_4$ electrode, (c) LiSi electrode, (d) Si electrode. Inset shows results (black) of EC- Li_xSi_y systems without the SEI layer.

In addition, a difference in current magnitude is observed in the various compositions of Li_xSi_y electrode. For systems where the SEI is SiO_2, the maximum currents, observed at around 5 V, are approximately 3.00, 2.33, 1.40, and 0.39 μA for the Li, $Li_{13}Si_4$, LiSi, and Si electrodes, respectively. For $Li_2Si_2O_5$ systems, the maximum currents are approximately 0.18, 0.18, 0.07, and 0.06 μA for the Li, $Li_{13}Si_4$, LiSi and Si electrodes, respectively.

In all cases, Li_2CO_3, SiO_2, and $Li_2Si_2O_5$, is observed that the Si electrode configuration has the most resistance to electron transfer. Similar results were reported previously for LiF and Li_2O compounds: their presence greatly reduced the electron transfer; and higher resistance was observed in the Si electrode configuration as well.[52]

Table 2.1 summarizes the maximum current estimated for each system. Given similar configurations of increasing number of molecules between electrolyte (EC) and electrode (Li_xSi_y), the trend of conductance (dI/dV) is found to be SiO_2 > Li_2CO_3 > $Li_2Si_2O_5$. These results indicate that at high voltages, there is a much higher resistance to electron transfer in $Li_2Si_2O_5$ systems. Moreover, results suggest that much lower currents are observed in compounds that are generally longer. As compared to LiF and Li_2O, Li_2CO_3 appears to be more electrically insulating.

Table 3.1. Maximum Currents (μA) for Each SEI Cluster and Electrode Stoichiometry.[a]

	Electrode			
SEI Molecule	Li	$Li_{13}Si_4$	LiSi	Si
No SEI	25.00	100.80	19.10	5.84
Li_2CO_3	0.39	0.20	0.28	0.17
SiO_2	3.00	2.33	1.40	0.39
$Li_2Si_2O_5$	0.18	0.18	0.07	0.06

[a] All currents in μA

The current at 2 V versus SEI thickness for Li_2CO_3 systems is shown in Figure 3.7(a). The current decreases rapidly as the SEI layer thickness increases by addition of molecules, thus implying higher electron transport at initial SEI formation stages and then significantly slower steady growth. The current starts approaching zero at ~12 Å, with values in the range of 0.04 to 0.22 μA, and decays up to three orders of magnitude at about 30 Å. The current (at 2 V) versus thickness results for SiO_2 and $Li_2Si_2O_5$ are shown in Figure 3.7(b) and Figure 3.7(c), respectively. In all cases there is a significant decrease in the current as the thickness of increases. The current approaches zero at ~16 Å in SiO_2, with values in the range of 0.03 to 0.5 μA. In $Li_2Si_2O_5$, the current approaches zero at ~20 Å, with values in the range of 1.4×10^{-5} to 0.14 μA, and decays up to three orders of magnitude at about 47 Å. Again, similar results were reported for LiF and Li_2O, where the current decays to almost zero at approximately 10 Å and 8 Å, respectively.[52]

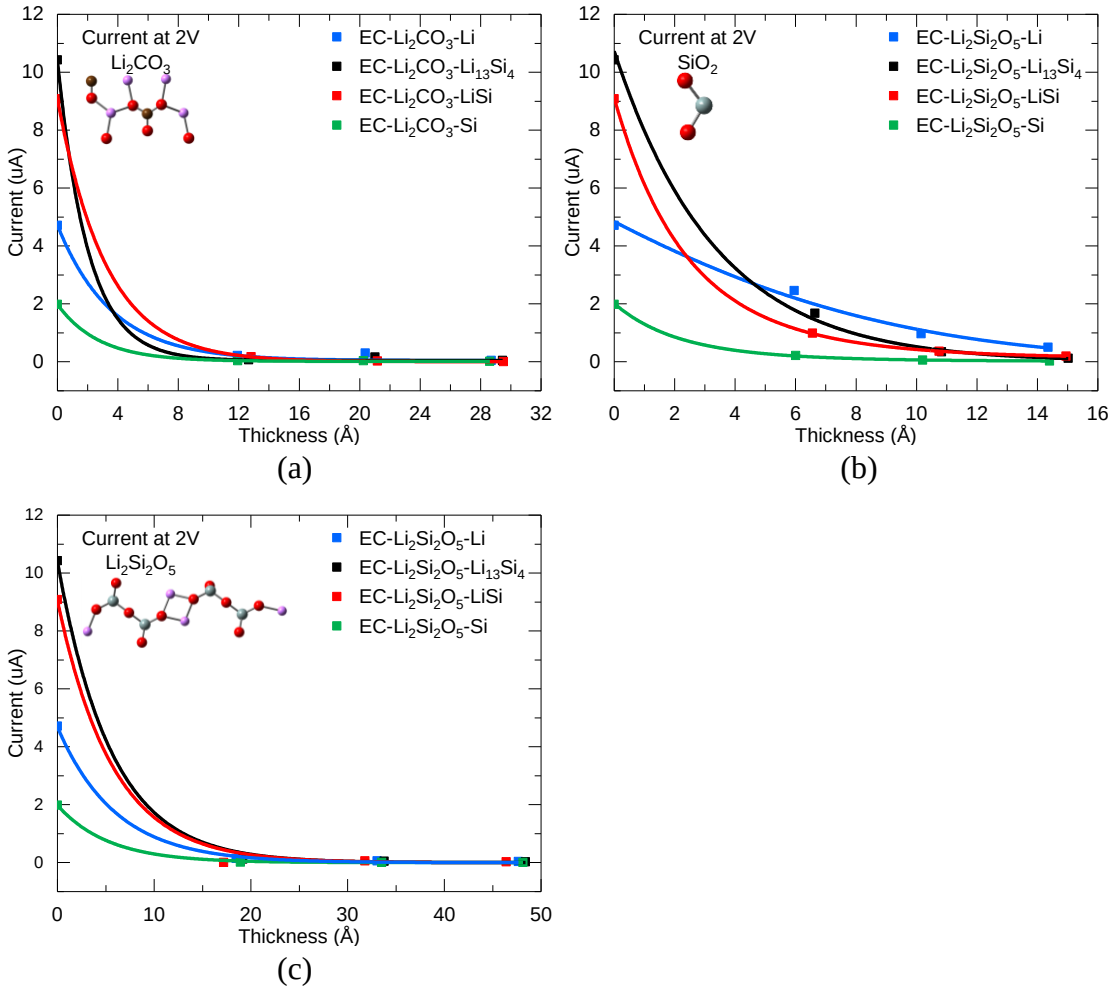

Figure 3.7. Current at 2 V versus layer thickness for (a) Li_2CO_3, (b) SiO_2, and (c) $Li_2Si_2O_5$.

In addition, HOMO-LUMO energies and HOMO-LUMO gaps (HLG) are calculated for all SEI products; for completeness, LiF and Li_2O results whose I-V characteristics have been previously studied and reported are included as well.[52] All HOMO-LUMO energies are presented in Figure 3.8. It can be observed in all cases, that the HOMO and LUMO energies generally decrease as the electrode lithiation decreases.

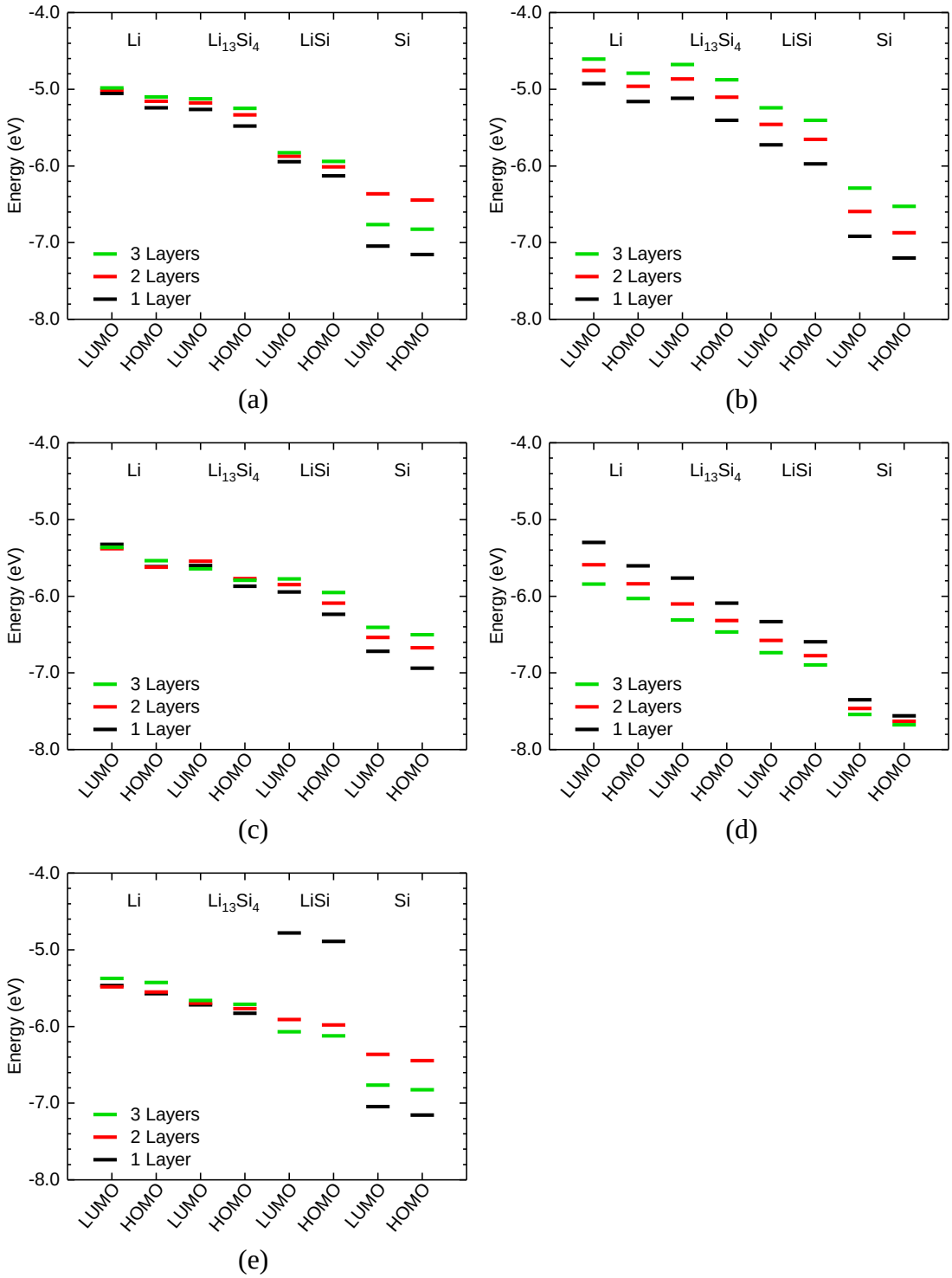

Figure 3.8. HOMO (solid line) and LUMO (dotted line) energies for all systems. (a) LiF, (b) Li_2O, (c) Li_2CO_3, (d) SiO_2 and (e) $Li_2Si_2O_5$.

In LiF and Li_2O cases, increasing the SEI layers increases both HOMO and LUMO energies. In Li_2CO_3 most HOMO and LUMO energies increase as the layers increase and in some electrode cases, Li and $Li_{13}Si_4$, the change is very small. In SiO_2 case, the HOMO and LUMO energies decrease as the SEI layer increases. Finally in $Li_2Si_2O_5$ case, for the Li and $Li_{13}Si_4$ electrodes, the HOMO and LUMO energies remain almost the same as the SEI layer increases; for the LiSi case, the energies decrease as the layers increase; and for the Si electrode the energies increase as the SEI increases.

HOMO-LUMO Gap (HLG) vs SEI thickness results for all Li_xSi_y electrode cases are presented in Figure 3.9. It can be observed, in all systems, that increasing the SEI layer reduces the HOMO-LUMO gap. For example, for Li_2CO_3 systems, the HLGs are 0.29, 0.24, and 0.17 eV for a SEI layer with 1, 2, and 3 units, respectively. This result is in accordance to the well-known effect of the size dependency of the band gap due to quantum confinement.[38, 139, 170-172] HOMO-LUMO gap results are tabulated in Table 3.2.

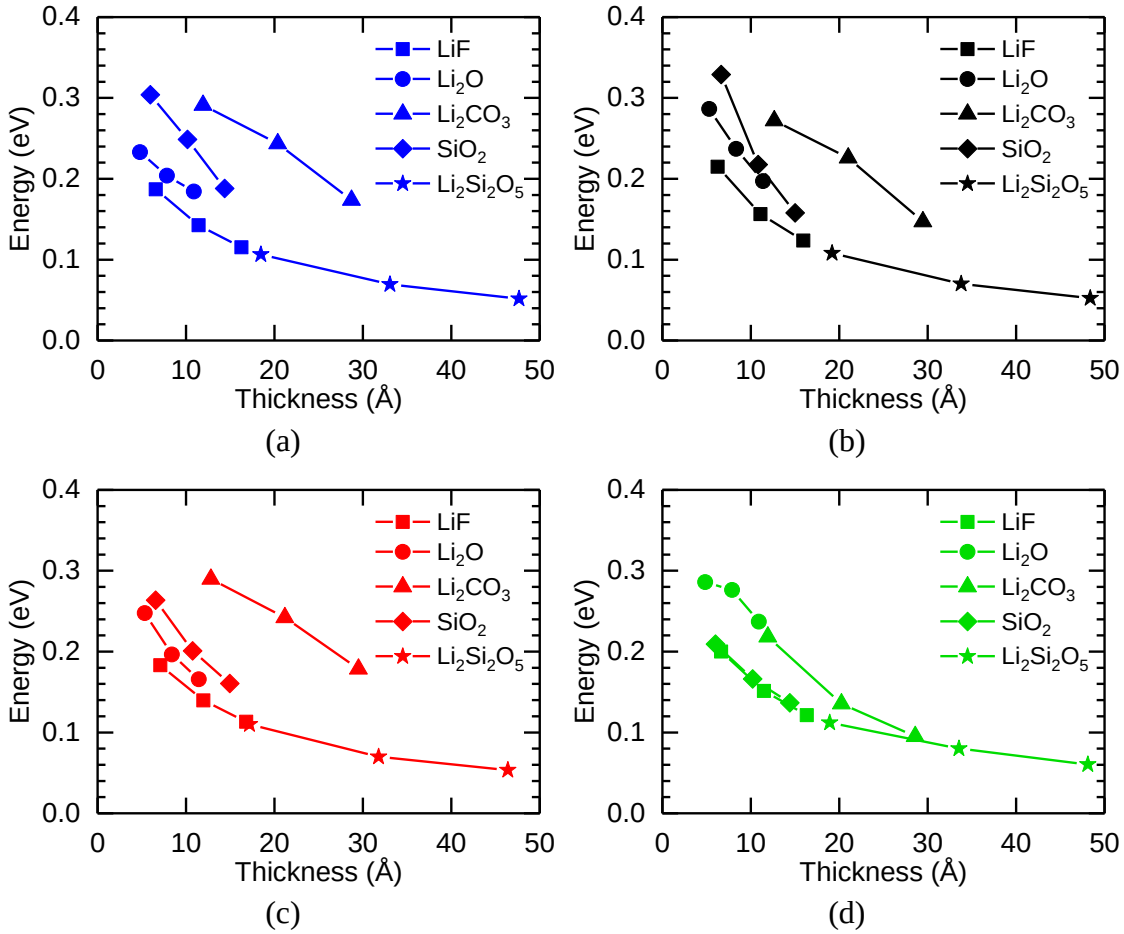

Figure 3.9. HOMO-LUMO gap energies vs SEI thickness for all systems. (a) Li electrode, (b) $Li_{13}Si_4$ electrode, (c) LiSi electrode, (d) Si electrode.

Table 3.2. HOMO-LUMO Gap Energies (eV) for All Systems.[b]

	Electrode			
SEI Molecule	Li	$Li_{13}Si_4$	LiSi	Si
No SEI	0.37	0.76	0.41	0.36
$(LiF)_1$	0.19	0.21	0.18	0.20
$(LiF)_2$	0.14	0.16	0.14	0.15
$(LiF)_3$	0.12	0.12	0.11	0.12
$(Li_2O)_1$	0.23	0.29	0.25	0.29
$(Li_2O)_2$	0.20	0.24	0.20	0.28
$(Li_2O)_3$	0.18	0.20	0.17	0.24

Table 3.2. Continued.

	Electrode			
SEI Molecule	Li	$Li_{13}Si_4$	LiSi	Si
$(Li_2CO_3)_1$	0.29	0.27	0.29	0.22
$(Li_2CO_3)_2$	0.24	0.23	0.24	0.14
$(Li_2CO_3)_3$	0.17	0.15	0.18	0.10
$(SiO_2)_1$	0.30	0.33	0.26	0.21
$(SiO_2)_2$	0.25	0.22	0.20	0.17
$(SiO_2)_3$	0.19	0.16	0.16	0.14
$((Li_2Si_2O_5)_1$	0.11	0.11	3.64	0.11
$(Li_2Si_2O_5)_2$	0.07	0.07	0.19	0.49
$(Li_2Si_2O_5)_3$	0.05	0.05	0.05	0.06

[b] All gap energies in eV

The distances from the oxygen atom labeled O_1 of the EC molecule to the closest atom, either Si_1 or Li_1, in the Li_xSi_y cluster (Figure 3.2 and Figure 3.10) are shown in Table 3.3. The distances are directly measured in the assembled models using visualization software.

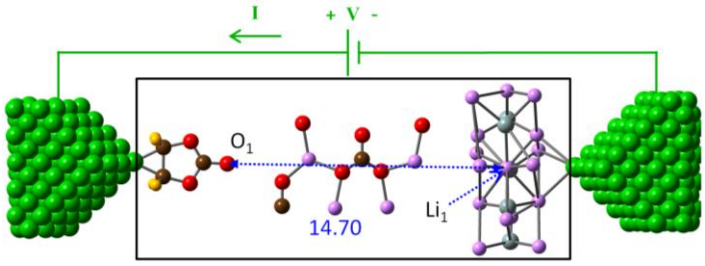

Figure 3.10. Distance from EC molecule to Li_xSi_y cluster example. Distance is measured from the rightmost oxygen atom (labeled O_1) of the EC molecule to the closest atom (Li_1) in the $Li_{13}Si_4$ cluster to calculate the leakage current from the anode to the solvent through the SEI by applying an external voltage V using two external nanotips (green). Li (purple), Si (gray), O (red), H (yellow), C (brown).

Table 3.3. Distances (Å) from the O_1 (Figure 3.2) Atom in the EC Molecule to the Closest (Li_1 or Si_1) Atom in the Li_xSi_y.[c]

	Electrode			
SEI Molecule	Li	$Li_{13}Si_4$	LiSi	Si
No SEI	1.81	1.93	1.95	1.82
$(LiF)_1$	8.09	8.19	8.20	8.47
$(LiF)_2$	12.91	13.03	12.98	13.31
$(LiF)_3$	17.74	17.88	17.79	18.16
$(Li_2O)_1$	6.33	7.24	6.48	6.66
$(Li_2O)_2$	9.34	10.28	9.47	9.70
$(Li_2O)_3$	12.37	13.31	12.48	12.74
$(Li_2CO_3)_1$	13.39	14.70	13.87	13.75
$(Li_2CO_3)_2$	21.75	23.03	22.19	22.07
$(Li_2CO_3)_3$	30.07	31.40	30.51	30.42
$(SiO_2)_1$	7.48	8.57	7.68	7.82
$(SiO_2)_2$	11.65	12.76	11.81	12.02
$(SiO_2)_3$	15.84	16.95	15.99	16.22
$((Li_2Si_2O_5)_1$	19.84	21.49	19.36	20.76
$(Li_2Si_2O_5)_2$	34.43	36.09	33.92	35.36
$(Li_2Si_2O_5)_3$	49.03	50.69	49.26	49.95

[c] All distances in Å

Several electrolyte reduction mechanisms and reduction energies (ΔE) are found in the literature, but they can be summarized into 1-electron and 2-electron mechanisms.[152-154] Ma et al. studied the decomposition mechanisms of ethylene carbonate (EC) on Si clusters using density functional theory.[153] Table 4 shows the reaction energy and energy barriers (ΔE_{ji}) for the reactions reported by Ma and Balbuena.[153] State **1** (Figure 3.11) corresponds to the initial geometry, and **2** to **7**

correspond to the intermediate and transition state geometries. Detailed explanation on each geometry can be found on Ma et. al work.[153]

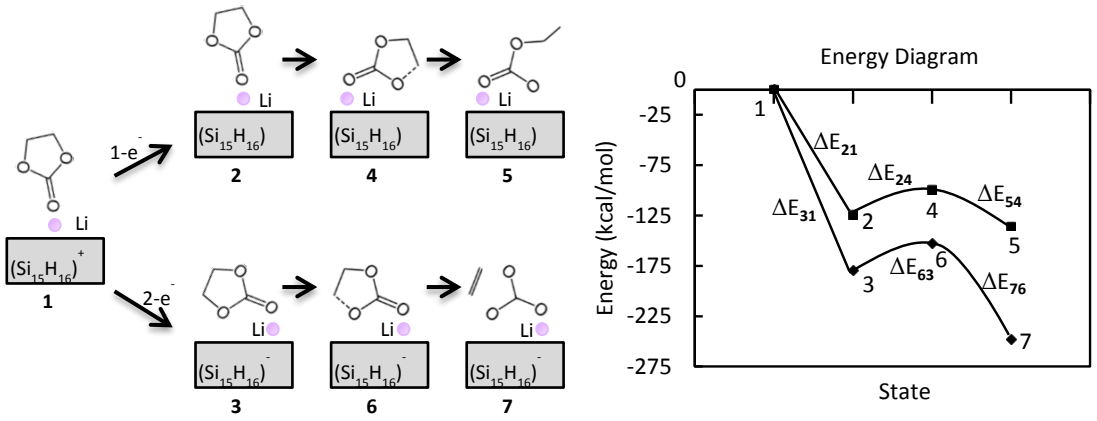

(a) (b)

Figure 3.11. 1- and 2-electron reactions with the ethylene carbonate on a silicon cluster.[153] (a) **1,** EC---$Li(Si_{15}H_{16})^+$ ion complex of EC on a $Li(Si_{15}H_{16})$ cluster; **2,** EC---$Li(Si_{15}H_{16})$ neutral complex of EC on a $Li(Si_{15}H_{16})$ cluster; **3,** EC---$Li(Si_{15}H_{16})^-$ ion complex of EC on $Li(Si_{15}H_{16})$ cluster; **4,** transition state for the EC molecule dissociation on the $Li(Si_{15}H_{16})$ surface; **5,** resulting intermediate geometry of the dissociation of EC on the $Li(Si_{15}H_{16})$ surface; **6,** transition state for the EC molecule dissociation on $Li(Si_{15}H_{16})^-$ surface; **7,** resulting intermediate geometry for the dissociation of EC on the $Li(Si_{15}H_{16})^-$ surface. (b) Energy diagram evolution for the 1- and 2-electron mechanisms.

Figure 3.11 shows the energy diagram for the 1- and 2-electron reduction mechanisms corresponding to the data shown in Table 4. Using $\Delta t \approx (\hbar/2)(1/\Delta E)$, Δt_{ji} can be found as well as the total time changes (Δt_{51} and Δt_{71}) which are found by addition of Δt_{21}, Δt_{42}, and Δt_{54} for Δt_{51}, and Δt_{31}, Δt_{63}, and Δt_{76} for Δt_{71}. Table 3.4 summarizes the energy changes presented in Figure 3.11 and the calculated time changes. According to the uncertainty principle, each time change corresponds to the minimum duration of the

corresponding reaction.[173] For the 1e mechanism, Δt_{51} = 0.58 fs is obtained, and for the 2e mechanism, Δt_{71} = 0.4 fs; these results are in a time scale reasonable for electron transfer in a single molecule.[173] Then using $I \leq 2\Delta Q \Delta E/\hbar$, Δt_{51}, and Δt_{71}, the current (I) for each 1- and 2-electron mechanisms is calculated; the results are also shown in Table 3.4. Moreover, the electron affinity of ethylene carbonate in solution was reported to be 9.65 kcal/mol,[93] resulting in a current of 2×10^{-4} A, which is comparable to the results found in Table 3.4. The EC-Si system, shown in Figure 3.2(d), can be compared to the system studied by Ma and Balbuena.[153] The maximum current found for the EC-Si system is 5.8×10^{-6} A, which is two orders of magnitude smaller than the current calculated using $I \leq 2\Delta Q \Delta E/\hbar$ (Table 3.4). This is in accordance to the fact that the currents calculated using the equality of this direct approach represent upper limits to their exact values.

Table 3.4. Energies, Times of Reaction, and Estimated Currents for the 1-e and 2-e Mechanisms. Total currents (I_{total}) corresponds to the maximum electron transfer rate that can be sustained by the reaction; also $\Delta t_{51} = \Delta t_{21} + \Delta t_{42} + \Delta t_{43}$ and $\Delta t_{71} = \Delta t_{31} + \Delta t_{63} + \Delta t_{76}$.

Transfer i→j	ΔE_{ji} (kcal/mol)[d]	Δt_{ji} (s)	I_{total} (A)
1 + e^- →**2**	-124.5	6.1×10^{-17}	
2→**4**	24.8	3.1×10^{-16}	
4→**5**	-36.0	2.1×10^{-16}	
1 + e^- →**5**		5.8×10^{-16}	2.8×10^{-4}
1 + **2**e^- →**3**	-179.7	4.2×10^{-17}	
3→**6**	27.2	2.8×10^{-16}	
6→**7**	-95.1	8.0×10^{-17}	
1 + $2e^-$ →**7**		4.0×10^{-16}	8.0×10^{-4}

[d] Energies taken from.[153]

3.5. Conclusions

The electron transport on various SEI products and oxides is investigated in four lithiation stages of the anode using a DFT-GF approach to understand early stages of SEI nucleation and growth. Results indicated that, in all Li_xSi_y cases, the current is significantly reduced with the addition of the SEI components as compared with the systems where no SEI element is present. Moreover, increasing the thickness of the SEI layer also resulted in a reduction of the electron transfer. Results indicated that at high voltages of ~5 V, $Li_2Si_2O_5$ presents a much higher resistance to electron transfer than Li_2CO_3 and SiO_2. Results also showed that the current decreases exponentially as the SEI layer thickness increases, thus implying higher electron transport at initial SEI formation stages and then significantly slower steady growth. Findings in this work complemented previous studies by expanding the electron transport analysis to the main component of the inner layer of the SEI and surface oxides, which when combined with studies of ion transport would provide key information for the development of thin layers of coating to protect the electrodes. HOMO-LUMO gaps for all systems were calculated. It was observed, in all systems, that increasing the SEI layer reduces the HOMO-LUMO gap. In addition, estimations based on the uncertainty principle were used to calculate the current (I) produced by an energy change (ΔE) of electrolyte reduction; these currents are in the range of 10^{-4} A, two orders of magnitude larger than currents found using the DFT-GF approach in a similar system. This at least confirms correctly that the electronic current calculations from the GENIP program are below the upper quota dictated by the uncertainty principle. On the other hand, it could not be

found in the literature any experimental indication of a measurement of the leakage current by electrons. The impedance measurements that have been done so far are due to the Li-ions traveling from the cathode to the anode or vice versa. This is very different to the leakage current due to the electrons that leak during charging from the anode to the solvent in which they react. An experiment to measure this effect would need to have a fully accessible battery in which the leakage electrons can be detected perhaps by the reaction products produced in the solvent. Nevertheless, as indicated in the Methodology (Section 3.3), the procedure GENIP yielded consistent results, and indirectly, it can be said that the methods involved in the procedure always were consistent with very precise related experiments.

4. ION DIFFUSIVITY THROUGH THE SOLID ELECTROLYTE INTERPHASE IN LITHIUM-ION BATTERIES*

4.1. Synopsis

Understanding the transport properties of the solid electrolyte interphase (SEI) is a critical piece in the development of lithium ion batteries (LIB) with better performance. The lithium ion diffusivity in the main components of the SEI found in LIB with silicon anodes is studied. Classical molecular dynamics (MD) simulations are performed on lithium fluoride (LiF), lithium oxide (Li_2O) and lithium carbonate (Li_2CO_3) in order to provide insights and to calculate the diffusion coefficients of Li-ions at temperatures in the range of 250 K to 400 K, which is within the LIB operating temperature range. A slight increase in the diffusivity as the temperature increases is found. Simulation results show that Li-ion diffusion coefficients at 300 K are 3.93×10^{-16} m^2/s, 4.01×10^{-16} m^2/s, and 4.90×10^{-17} m^2/s for LiF, Li_2O and Li_2CO_3 respectively; previously published computational results by other authors report diffusion coefficients in the range of 10^{-26} to 10^{-12} m^2/s. Moreover, the activation energies obtained are 0.04 eV, 0.22 eV and 0.12 eV for LiF, Li_2O and Li_2CO_3, respectively; activation energies previously obtained by others experimentally and theoretically are within 0.15 to 0.8 eV. Since diffusion is more easily noticeable at high temperatures, Li-ion diffusion over

*Reprinted with permission from:
Ion Diffusivity through the Solid Electrolyte Interphase in Lithium-Ion Batteries by L. Benitez and J. M. Seminario, 2017. *J. Electrochem. Soc.*, 164, E1-E12, Copyright 2017 by The Electrochemical Society.

temperatures in the range of 1300 K to 1800 K is also studied and the diffusion mechanisms involved in each SEI compound are analyzed. The mechanisms of Li-ion diffusion observed include both vacancy assisted and knock-off diffusion in LiF, direct exchange in Li_2O, and vacancy and knock-off in Li_2CO_3. Moreover, the effect of applied electric field in the diffusion of Li-ions at room temperature is also evaluated. It is found that as the electric field is increased, Li-ion diffusion exponentially increases, and coefficients that are at least five orders of magnitude greater than those where no field is applied are obtained. Results in this work are in good agreement with available experimental data and other computational results. This investigation of transport properties in individual SEI compounds provides essential knowledge, such as diffusion coefficients and diffusion mechanisms in a wide temperature range and under applied electric field, useful for the improvement of Li-ion batteries and for others using technologies beyond the Li-ion. Better understanding of SEI properties helps in accurately designing SEI films that could improve Li-ion battery performance. Furthermore, the evaluated force fields can be used to study further Li-ion transport in complex structures containing two or more SEI materials using classical molecular dynamics simulations.

4.2. Introduction

As mentioned in Section 1.2, there are an increasing number of studies, both experimental and theoretical, on Li-ion transport within the electrolyte and in the electrodes;[66-87, 91] the boundary between the liquid electrolyte and the electrode;[88-90, 93]

and even the SEI as a whole.[24, 36, 61, 92] In this section, transport mechanisms are studied and diffusion coefficients are predicted in the individual interphase components.

It has been found that lithium ion diffusion in the SEI is thought to occur through grain boundaries, through porous regions, or through interstitials and vacancies.[35, 150, 174-175] Each SEI component may exhibit one or more of these ion transport mechanisms. Below, ion diffusion studies and diffusion mechanism investigations found in the literature for the three main components of the inorganic SEI layer are summarized.

One of the most often-reported to be found in the SEI is LiF; this inorganic compound has been observed in both carbon and silicon based anodes. One study reported that its cation diffusivity is much lower than in other SEI inorganic compounds, and suggested that diffusion in LiF cause rate limitations in Li-ion batteries;[150] they used periodic density functional theory (DFT) calculations to determine dominant diffusion carriers and diffusion pathways, as well as used the nudge elastic band (NEB) method to calculate energy barriers of diffusion; they found that vacancies were "energetically more favorable" than interstitials, and reported energy barriers of 0.73 and 1.09 eV for neutral vacancies and neutral Schottky vacancies, respectively; moreover the associated diffusion coefficients they found were in the range of 10^{-26} to 10^{-20} m^2/s. Similar results for the energy barrier were found in other DFT studies where the lithium dynamics were investigated.[64, 176] Also, earlier experimental investigations using NMR obtained energy barriers in the range of 0.65 to 0.73 eV.[177] Two recent studies, one using molecular dynamics, [77] and the other applying phase-field model together with Fick's law,[21] reported diffusion coefficients of Li in LiF at room temperatures (298 K to 318 K) in the

range of 3.7×10^{-16} m^2/s. Moreover, diffusion in LiF has been more extensively studied at high temperatures since this compound is an important component of the molten salt mixtures used as primary coolant and fuel in nuclear fission reactors. Investigations using molecular dynamics and experimental techniques obtained diffusion coefficients in high temperature range (700 K to 1400 K), and in temperatures close to the melting point of LiF, and reported values in the range from 0.25 to 1.86 eV for the diffusion energy barrier.[178-184]

Only a couple of theoretical studies reported diffusion barriers in Li_2O at low temperature.[64, 176] Chen et al.[64] used DFT to investigate the electronic structure and the vacancy-assisted Li diffusion using NEB method; they showed that Li_2O electronic structure had insulating character and obtained a diffusion barrier of 0.15 eV. Additionally, Guan et. al.[24] and Tasaki et. al.,[185] in addition to studying LiF, also studied diffusion in Li_2O and found transport coefficients in the range of 1.7×10^{-16} m^2/s. Lithium diffusion in Li_2O has been widely studied at high temperatures due to its superionic (fast ion mobility) behavior at elevated temperatures.[71, 186-197] Most of these works focused on developing and evaluating force field parameters for molecular dynamics simulations, which were then used to analyze structure, physical properties, and diffusion.[186-195] Experimentally, diffusion of Li^+ in Li_2O was studied by Oishi et. al[196] using mass spectrometry and the ^6Li radioisotope as a tracer. In a recent study,[197] non-equilibrium molecular dynamics (NEMD) were used to obtain diffusion coefficients of Li at temperatures from ~870 K to ~1600 K. In NEMD, a fictitious electric field is applied in order to increase the occurrence of diffusion-related hopping events and thus accurately

calculate coefficients. They found that diffusion below 1200 K is dominated by synchronous nearest-neighbor hoping also called ring diffusion,[71] where two or more adjacent atoms move at the same time; at higher temperatures, interstitial-assisted diffusion mechanism governs. They also report, energy diffusion barriers of 0.26 and 1.11 eV for high temperatures and for superionic regime, respectively.

Lithium carbonate (Li_2CO_3) has been shown to be the main component of the dense inner SEI layer and it is claimed to be responsible for stabilizing SEI films.[175] Recent studies have mainly focused on finding the dominant diffusion carriers (interstitials and/or vacancies), their diffusion pathways and diffusion mechanisms, as well as the associated diffusion barriers. Shi and co-workers[174-175] in two separate works determined the dominant diffusion carriers, among interstitials, vacancies and Frenkel pairs, over a voltage range from 0 to 4.4V; they found that below 0.98 V interstitial Li^+ ions are the main carriers,[175] that above ~4 V vacancies dominate diffusion, and that between 0.98 and ~4 V interstitials and vacancies have the same influence.[174] Moreover, using the climbing image NEB (CI-NEB) method they observed that interstitial Li^+ moves via knock off mechanism and vacancy-assisted Li^+ diffusion is via direct hopping, and calculated energy barriers in the range of 0.31 for interstitials and 0.24 eV for vacancies. In addition, they report diffusion coefficient values in the range of 10^{-11} m^2/s over the voltage range they studied. Other investigations of Li-ion diffusion in bulk monoclinic Li_2CO_3 used DFT to find migration barriers and reported values of 0.23 to 0.49 eV.[64, 198] While there are studies focused on investigating the structure and

thermodynamics of Li_2CO_3,[63, 199-203] to the best of my knowledge, there are no reports on diffusion of Li-ion at high temperatures.

While the previously mentioned studies calculate diffusion coefficients only at room temperature, or only at very high temperatures (near melting), this work provides coefficients over a wider temperature range from 250 K to 1800 K, which includes LIB extreme charging temperatures (-20 to 45 °C).[204] Since SEI components are highly sensitive to temperature,[46] characterization under different temperatures is critical. Moreover, the effect of an applied electric field on the diffusion coefficient and on the diffusion mechanisms is investigated.

This study provides insight on lithium ion transport through individual SEI compounds: 1) At both low and high temperatures; and 2) At room temperature under an applied external electric field. This fundamental knowledge is useful in multi-scale computational methods developed to simulate SEI nucleation, growth and evolution.[24, 149, 205] The long-term goal is to eventually have more control over interface parameters such as composition, structure, porosity and thickness, and thus accurately design SEI films and therefore better Li-ion batteries. This work is a step towards this ultimate goal.

In this paper, the main components of the inorganic SEI layer are studied: lithium fluoride (LiF), lithium oxide (Li_2O) and lithium carbonate (Li_2CO_3).[30-31] First, the force fields needed for accurate molecular dynamics are evaluated. MD has the advantage that no previous knowledge of diffusion pathways is required and it can consider many-particle effects. Moreover, MD simulations allow studying phenomena that is not easily accessible with experimental techniques. Diffusion coefficients at several temperatures

are calculated in order to provide fundamental understanding on the transport properties of the solid electrolyte interphase found in lithium ion batteries. Furthermore, the room temperature diffusivity of Li-ions as function of an applied electric field is obtained.

In Section 4.3, details of the computational methods used are given. In Section 4.4, the results and discussions are presented. The results from the defect free SEI structures are first discussed; findings on diffusion of Li-ions over low and high temperatures are then examined; and finally, the details of the diffusion coefficients obtained after applying an electric field are reported. In Section 4.5, the findings and conclusions are briefly summarized.

4.3. Methodology

The SEI products in this study consist of lithium fluoride (LiF), lithium oxide (Li_2O) and lithium carbonate (Li_2CO_3). Their structures and crystal lattice parameters are obtained from the Inorganic Crystal Structure Database (ICSD).[133] A 5×5×5 supercell is used for LiF, a 4×4×4 supercell for Li_2O and a 3×3×4 supercell for L_2CO_3; simulation box sizes are 20×20×20 Å for LiF, 22×22×22 Å for Li_2O, and 24×21×25 Å for Li_2CO_3. Figure 4.1. shows the SEI structures studied.

In addition, all studied SEI structures are set up with three-dimensional periodic boundary conditions. Both lithium fluoride and lithium oxide are modeled by the standard 6-12 Lennard-Jones (LJ) potential energy, which for a pair of atoms i and j at a distance r is given by

$$E_{6\text{-}12\ LJ} = 4\varepsilon\left[\left(\frac{\sigma}{r}\right)^{12} - \left(\frac{\sigma}{r}\right)^{6}\right] \qquad r < r_c \qquad (4.1)$$

where ε is the depth of the LJ potential well, σ is the distance at which the potential is zero and $\sigma = 2^{(-1/6)} r_m$; r_m is the distance at the minimum (equilibrium) energy.

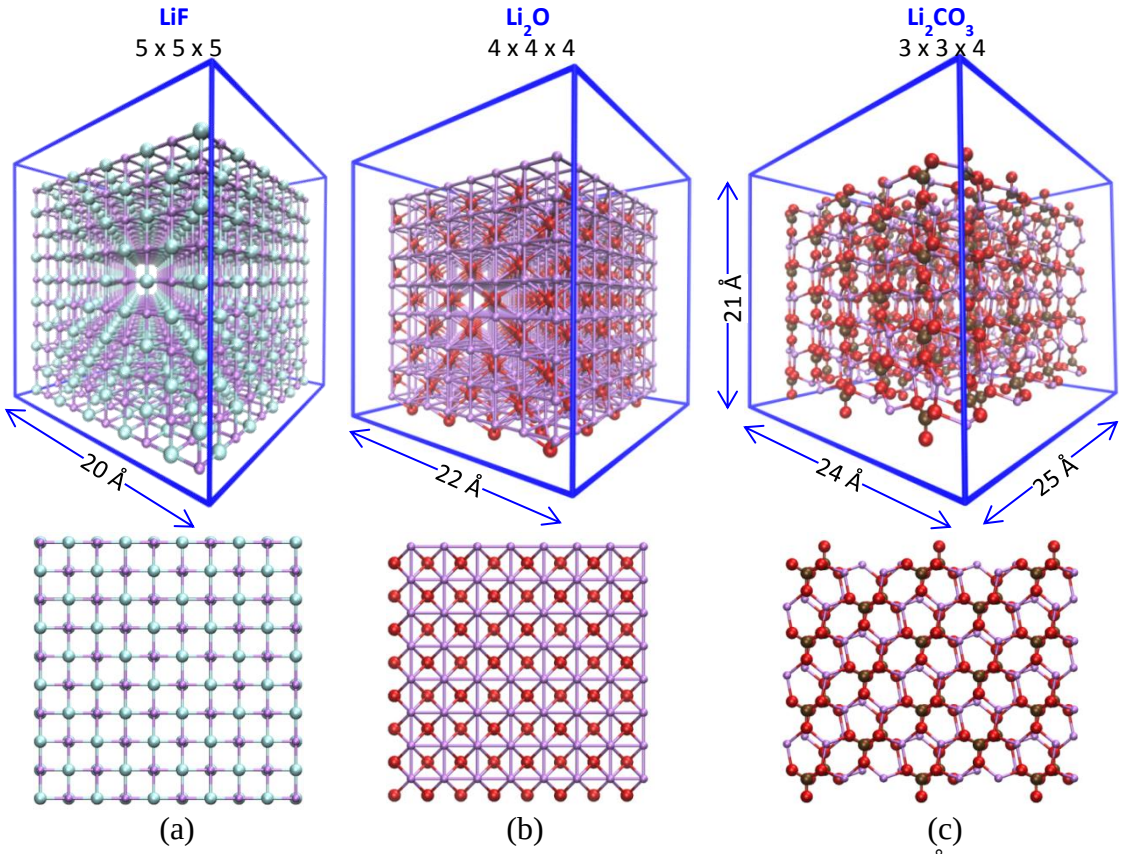

Figure 4.1. SEI structures studied. (a) LiF: 5×5×5 supercell, 20×20×20 Å box size, 500 Li atoms and 500 F atoms. (b) Li_2O: 4×4×4 supercell, 22×22×22 Å box size, 512 Li atoms and 256 O atoms. (c) Li_2CO3: 3×3×4 supercell, 24×21×25 Å box size, 288 Li atoms and 144 C atoms and 432 O atoms. Li (purple), F (cyan), O (red), C (brown).

In addition, a Coulombic pairwise interaction is also used given by

$$E_{Coul} = \frac{q_i q_j}{\epsilon r} \qquad r < r_c \qquad (4.2)$$

where q_i and q_j are the charges of the pair of atoms i and j, and ϵ is the dielectric constant. In considering the charges, it is taken into account that fluorine presents the possibility of forming a σ-hole,[206-208] a noncovalent interaction between a covalently-bonded halogen and a negative site; however, the fraction of covalent bonding in LiF is very little ~0.1 due to the large differences in electronegativities of the two atoms, which actually yield a strong ionic bond.

For both potentials, LJ and Coulombic, there is an r_c cutoff distance after which the energy is not calculated; the cutoff distance (r_c) in all calculations is 10 Å. In order to compensate for the abrupt change in energy at the cut-off distance, long range Coulombic interactions in LiF and Li_2O are evaluated by the Ewald summation technique outside this cut-off distance.[209] Lithium carbonate uses the standard 6-12 LJ and coulombic interaction potentials given by (4.1) and (4.2) respectively, together with bond, angle and improper dihedral interactions given by

$$E_{bond} = k_b(r-r_0)^2 \tag{4.3}$$

$$E_{angle} = k_\theta(\theta-\theta_0)^2 \tag{4.4}$$

$$E_{improper} = k_\chi(\chi-\chi_0)^2 \tag{4.5}$$

where k_b, k_θ and k_χ are force constants, r is the distance between the atoms and r_0 is the equilibrium bond distance; θ is the angle between atoms and θ_0 is the equilibrium angle; χ is the improper dihedral angle and χ_0 is the equilibrium value of the improper dihedral angle. The 6-12 LJ potential parameters and ionic charges used for LiF are tabulated in Table 4.1.[185, 210] ε and σ are mixed using Lorentz-Berthelot rules.[210] The parameters and

charges used to describe Li_2O and Li_2CO_3 are presented in Table 4.1.[211-212] ε and σ are mixed using geometric combination rules.[212] Bond, angle and improper interaction parameters utilized are tabulated in Table 4.2.

Table 4.1. 6-12 Lennard-Jones Parameters and Atom Charges for LiF, Li_2O and Li_2CO_3.[185, 210-212]

SEI Product	Atom	ε (kJ /mol)	σ (Å)	q (e)
LiF	Li	0.24125	1.715	0.78
	F	0.02707	3.954	-0.78
Li_2O	Li	0.1046	2.183	0.75
	O	0.25104	3.118	-1.5
Li_2CO_3	Li	0.1046	2.183	1.0
	C	0.43932	3.431	0.9853
	O	0.25104	3.118	-0.9951

Table 4.2. Bond, Angle and Improper Dihedral Interaction Parameters for Li_2CO_3.

Bond C-O		Angle O-C-O		Improper O-C-O-O	
k_b (kJ/mol-Å^2)	r_0	k_θ (kJ/mol-rad^2)	θ_0	k_χ (kJ/mol-rad^2)	χ_0
3222	1.3	460.2	120	1050	180

All molecular dynamics simulations are done using Large-scale Atomic/Molecular Massively Parallel Simulator (LAMMPS),[213] and all visualizations of the structures are performed using the graphics software, Visual Molecular Dynamics (VMD).[214] In this investigation, the defect-free samples are first studied, and then the point defects are added in each SEI sample and the diffusion is evaluated. First an

energy minimization of each SEI product is performed in order to find a stable structure; then the samples are equilibrated at 5 K for 1 ns to allow the relaxation of the structure; next, a simple MD simulated annealing is followed with the following steps: first, a gradual temperature ramp up to 800 K is performed at a rate of 0.795 K/ps; subsequently, the sample is cooled down to 250 K at a rate of 0.55 K/ps, and finally it is stabilized at 250 K for 1 ns. Annealing is done in order to find a structure closer to a global energy minimum; thus, optimizing the structure of the samples. Then temperature equilibrations lasting 1 ns each are done in 25 K increments from 250 K to 400 K, in 50 K increments from 400 K to 600 K, and finally in 100 K increments from 600 K to 1800 K. Increase rates are 1 K/ps for all the aforementioned temperature ranges. All simulations are done at zero pressure since experimental diffusion studies, especially SEI studies must be carried out in vacuum. The NPT ensemble is used for all MD simulations and then some features are compared with those under the NVT ensemble. The time step used for LiF and Li_2O is 1 fs, a typical value for MD simulations, and for Li_2CO_3, a 0.1 fs time step is used since values smaller than 1 fs are used in samples modeled with bonded interactions.[81, 215]

First, the quality of the force fields is evaluated by checking the crystal structure and bond distances of each structure after the energy minimization, and after equilibrium at 300 K. In addition, snapshots of the structures are taken during each temperature equilibration every 2 ps, and the coordinates are saved. Then, the radial distribution functions (RDF's) for all the atom pairs in each compound are calculated with VMD at each temperature using the saved atom coordinates from the 500 snapshots taken.

Afterwards, the diffusion of Li^+ at various temperatures is evaluated. First, defects are created in each compound (LiF, Li_2O, and Li_2CO_3) in order to allow Li^+ ion diffusion. For that, one Li-ion and one F-ion are removed in LiF sample; two Li-ions and one O-ion are removed in Li_2O sample; and for Li_2CO_3, one Li-ion is added as interstitial. Again, energy minimization, equilibration at 5 K, thermalization, and equilibration at 250 K are done. Then temperature equilibrations are done from 250 K to 600 K and at high temperatures in the range of 700 K to 1800 K; temperature increments and the rates for the temperature ramps are the same as above. LiF and Li_2O are compared with available experimental and MD results. Once the structure is equilibrated, the mean square displacement (MSD) of the Li^+ ion is recorded at each temperature using the appropriate "compute" command in LAMMPS. Diffusion coefficients (D) are calculated from the mean square displacement (MSD), since D is proportional to the MSD[93] as shown by

$$D = \frac{1}{6}\langle|\vec{r}(t) - \vec{r}(t_0)|^2\rangle \tag{4.6}$$

where r is the position of the particle at each time step, t is the time, t_0 is the initial time, $\vec{r}(t) - \vec{r}(t_0)$ is the distance traveled by the particle over the time interval ($t - t_0$), and $\langle|\vec{r}(t) - \vec{r}(t_0)|^2\rangle$ is the MSD. The diffusion coefficient is found from the slope of the MSD vs time.

Lastly, an electric field is applied in the range of 0.1 V/Å to 0.85 V/Å to each of the studied structures and the diffusion coefficients are calculated. In different simulation runs for each SEI product and for each field applied, energy minimization, equilibration at 5 K for 100 ps, thermalization up to 800 K at a rate of 7.95 K/ps, cool

down to 300 K at a rate of 7.95 K/ps, and finally equilibration at 300 K for 100 ps are done. The electric field is applied to the sample at the 300 K equilibration and the MSD of the Li-ions is recorded during a 100 ps timeframe and snapshots of the structures are taken every 0.1 ps. As the electric field is increased from zero, only results in the linear regime of the MSD can be directly compared to results with no field applied. [197] The field is increased up to 0.85 V/Å where non-linear effects are clearly observed.

4.4. Results and Discussion

First the total energy obtained at each stage of the simulations performed for pristine and impure samples is analyzed. Figure 4.2 to Figure 4.4 show total energy and the temperature versus time for each case studied. For the case of LiF, shown in Figure 4.2(a-b), it can be observed that the energy of the pristine crystal structure (blue curve) starts at about -76 Gcal/mol, then increases to -70 Gcal/mol as the temperature is increased to 800 K (~2 ns), then it goes down to -74 Gcal/mol when the temperature decreases to 250 K (~3 ns). Afterwards, the energy increases in a stepwise manner to an average energy of -67.5 Gcal/mol at a temperature of 1200K (~20 ns). At this temperature (1200 K) the energy significantly jumps to -63.8 Gcal/mol. This suggests a change of phase in the structure, namely indicating the melting of LiF. There is a significant volume increase that produces a corresponding energy increase. After that, the energy continues increasing to -58.4 Gcal/mol as the temperature goes to 1800K (~28 ns). Energy variations around average values are approximately 0.1 Gcal/mol at low temperatures and 0.7 Gcal/mol at high temperatures. The energy profile does not change when the vacancy defects (black curve) are introduced to the structure. In both

LiF cases, pure and impure crystal structures, the major contributions to the energy come mainly from the short range and long range coulombic interactions. In comparison with simulations performed under the NVT ensemble, the energy of the pristine crystal structure (red curve) starts at about -71 Gcal/mol, then increases to -66 Gcal/mol as the temperature is increased to 800 K (~2 ns), then it goes down to -70 Gcal/mol when the temperature decreases to 250 K (~3 ns). After that, the energy increases in a stepwise manner to an average energy of -61 Gcal/mol as the temperature increases to 1800K (~20 ns). In the NVT case, the volume is not able to change and thus the jump in energy at 1200 K is not observed. Energy variations are similar to the NPT case. Again, the energy profile does not change significantly when the vacancy defects (green curve) are introduced to the sample.

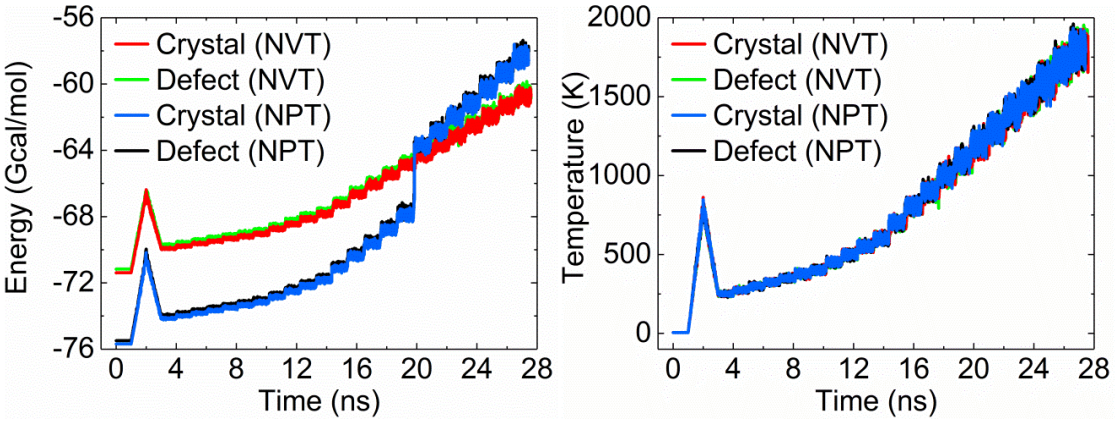

Figure 4.2. (a) Energy versus time curves and (b) Temperature versus time curves under NPT and NVT ensembles for LiF structures (vacancy defect ratio of 2/1000).

For the Li_2O defect-free structure (blue curve) shown in Figure 4.3(a-b), a large variation in the energy is observed at the beginning of the simulation which stabilizes when the sample is cooled down to 250 K (~3 ns). At 250 K the average energy value corresponds to -114 Gcal/mol. Then the energy increases in a stepwise style as the temperature of the sample is increased all the way up to 1800 K (~28 ns). Energy variations around average values are approximately 0.1 Gcal/mol and 1 Gcal/mol at low and high temperatures, respectively. Again, the energy profile does not change when the vacancy defects (black curve) are introduced in the Li_2O crystal. In both cases, pure crystal and impure structure, the major energy contributions to the total energy come from the short range and long range coulombic interactions.

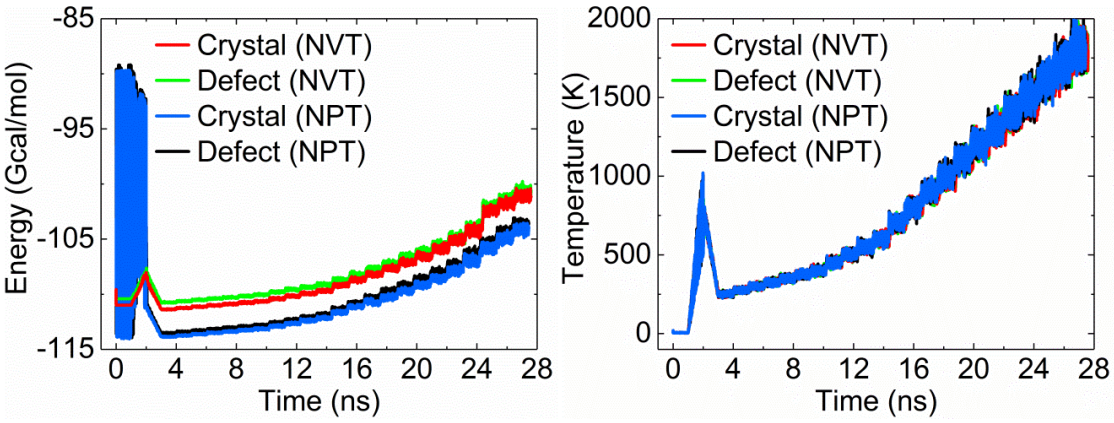

Figure 4.3. (a) Energy versus time curves and (b) Temperature versus time curves under NPT and NVT ensembles for Li_2O structures (vacancy defect ratio of 3/798).

In the NVT case, for the pristine crystal structure (red curve), the large variation in the energy at the beginning of the simulation run is not observed; the energy of the defect-free structure starts at -111 Gcal/mol, then it increases to -108 Gcal/mol as the temperature is increased to 800 K (~2 ns); it then goes down to -111 Gcal/mol when the temperature decreases to 250 K (~3 ns). Then the energy increases in a stepwise style as the temperature is increased all the way up to 1800 K (~28 ns). Energy variations around average values are approximately the same in both NVT and NPT cases. Moreover, the energy profile does not change when the vacancy defects (green curve) are introduced in the Li_2O structure.

In the case of Li_2CO_3, in order to find the best the volume for this structure, a test simulation was performed under the NPT ensemble first. In this test run, the structure was first minimized, then heated to 800 K (0.795 K/ps), subsequently cooled down to 250 K (0.55 K/ps), then slowly heated back up to 1800 K (~0.060 K/ps). Then, production runs under the NPT and NVT ensembles were restarted using the last saved state from the NPT test run. The calculations were restarted using the simulation box size and shape, boundary settings, atom positions and velocities, as well as atom attributes and force field styles and coefficients. Therefore, for the case of Li_2CO_3, shown in Figure 4.4(a-b), the energy of the defect-free structure (blue curve) starts around the average value of -62 Gcal/mol and slowly goes down to an average value of -74 Gcal/mol as the temperature goes up to 1800 K. When the interstitial Li^+ is introduced to the structure (black curve), no changes are observed in the energy profile. The energy variations in the Li_2CO_3 case are approximately 11 and 17 Gcal/mol at low

and high temperatures, respectively. In both cases, the pristine crystal and impure structure, the major energy contribution to the total energy comes from very strong short range coulombic interactions. Comparing with the NVT ensemble, the energy of the pristine crystal structure (red curve) first starts at an average value of -73 Gcal/mol, then goes slightly up to -69 Gcal/mol and then slowly goes down to -71 Gcal/mol as the temperature increases to 1800 K. Energy variations are approximately the same in both NVT and NPT cases. Again no changes are observed in the energy profile when the interstitial defect (green curve) is introduced to the structure. Comparing the energy profiles of the different SEI components studied, it can be observed that the lowest energies are obtained in the Li_2O case which yields energies in the range from -115 to -100 Gcal/mol (excluding initial energy variations). Then LiF case yields energies from -76 to -58 Gcal/mol. Finally, Li_2CO_3, produces energies in the range of -50 to -85 Gcal/mol.

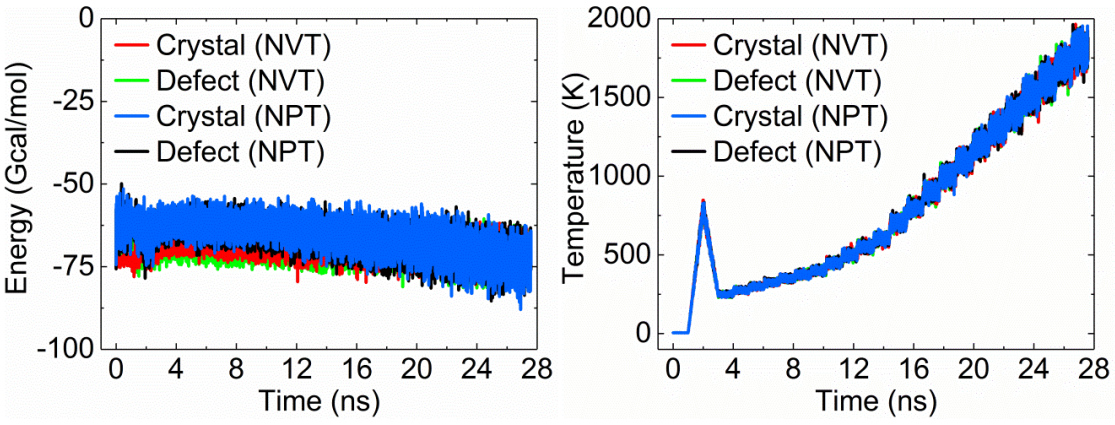

Figure 4.4. (a) Energy versus time curves and (b) Temperature versus time curves under NPT and NVT ensembles for Li_2CO_3 structures (interstitial defect ratio of 1/864).

The defect free structures are then studied to evaluate the force fields. First, it is verified that the crystal structure and bond distances of each SEI compound are maintained after the energy minimization and equilibrium at 300 K. Figure 4.5 shows the structures obtained after equilibration at 300 K for LiF, Li_2O, and Li_2CO_3. It can be observed, in all cases, that the crystal structure was not changed significantly. For LiF, the crystal order is well maintained both after minimization and equilibration at 300 K. For Li_2O case, there is minor disorder after the energy minimization; however, the crystal order and structure are reestablished after thermalization up to 800 K and then, equilibration at 300 K.

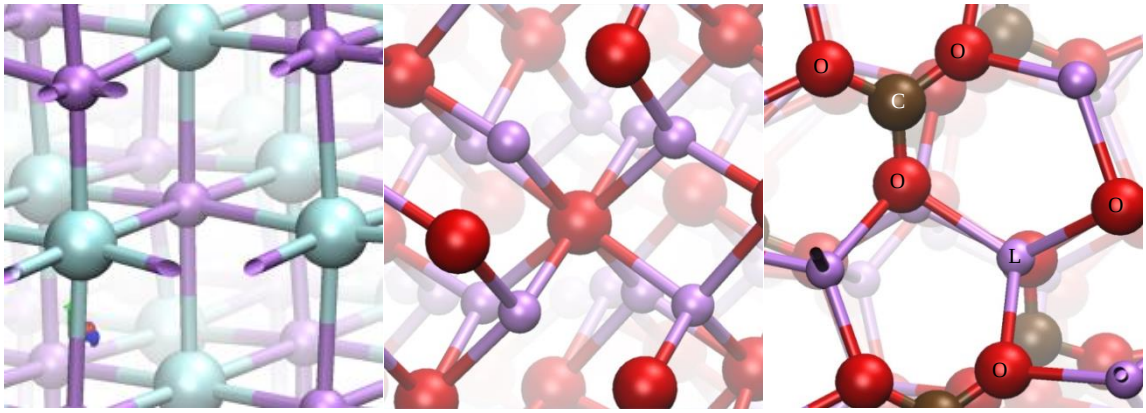

(a) (b) (c)

Figure 4.5. Structure after 300 K equilibrium for (a) LiF, (b) Li_2O and (c) Li_2CO_3. Li (purple), F (cyan), O (red), C (brown).

For Li_2CO_3, the crystal structure is conserved during minimization; nonetheless, in the equilibration at 300 K, slight crystal distortion is seen. Table 4.3 presents a comparison

of all bond distances obtained in this work and the data available in the ICSD.[133] For all compounds, bond distances remain quite similar after minimization; at 300 K equilibrium, even though there is more variation than that of the minimization, the bond distances are still within ±0.2 Å.

Table 4.3. Comparison of Calculated and Experimental Bond Distances

SEI Product	Bond	Bond distance (Å)		
		Bergerhoff et al.[133]	After Minimization	After Equilibration at 300 K
LiF	Li-F	2.01	2.00	2.20
Li_2O	Li-O	2.00	1.93	1.95
	Li-Li	2.31	2.32	2.26
Li_2CO_3	C-O1	1.30	1.29	1.30
	C-O2	1.30	1.29	1.30
	C-O3	1.27	1.30	1.31
	Li-O1	1.97	1.96	1.95
	Li-O2	1.93	1.94	1.94
	Li-O3	1.89	1.89	1.96

RDF curves for temperatures ranging from 250 K to 1800 K are analyzed and only selected representative RDF curves are presented in Figure 4.6. For LiF, the RDF curves from 250 K to 800 K are similar. Characteristic peaks representing the crystalline structure are observed, and the intensity of the peaks decreases and their widths broadens as the temperature increases. At 1000 K, the RDF is significantly different from those at lower temperatures, peaks can still be observed yet they are shifted and broader, indicating that some disorder in the structure is starting to appear. At 1200 K, the

characteristic peaks disappear and g(r) approximates to 1 at long range, indicating that the simulated structure becomes liquid at this temperature; this suggests that the result for melting temperature of 1200 K is very close to the experimental melting point of LiF (1122 K).[216] At temperatures greater than 1200 K, all RDF curves are equal to the 1200 K curve.

Li_2O RDF curves from 250 K to 600 K are alike; their peaks decrease and broaden as temperature increases. From 800 K to 1400 K peaks continue to decrease and widen until individual peaks combine. At 1800 K, a considerable difference is observed, peaks start vanishing and g(r) begins approaching a value of 1 at long range; however, the simulated structure does not become liquid at this temperature, implying that a value greater than 1800 K for the melting temperature is obtained, which is higher than the experimental result of 1700 K.[217]

For Li_2CO_3 compound, the RDF curves in the temperature range from 250 K to 1100 K are almost the same. A small decrease in the first peak intensity is observed as the temperature increases above 1200 K, this suggests that melting is starting to occur around this temperature; this melting temperature obtained is higher than the experimental value of 996 K.[218-219] At 1800 K the RDF curves are clearly different than the curves at lower temperatures.

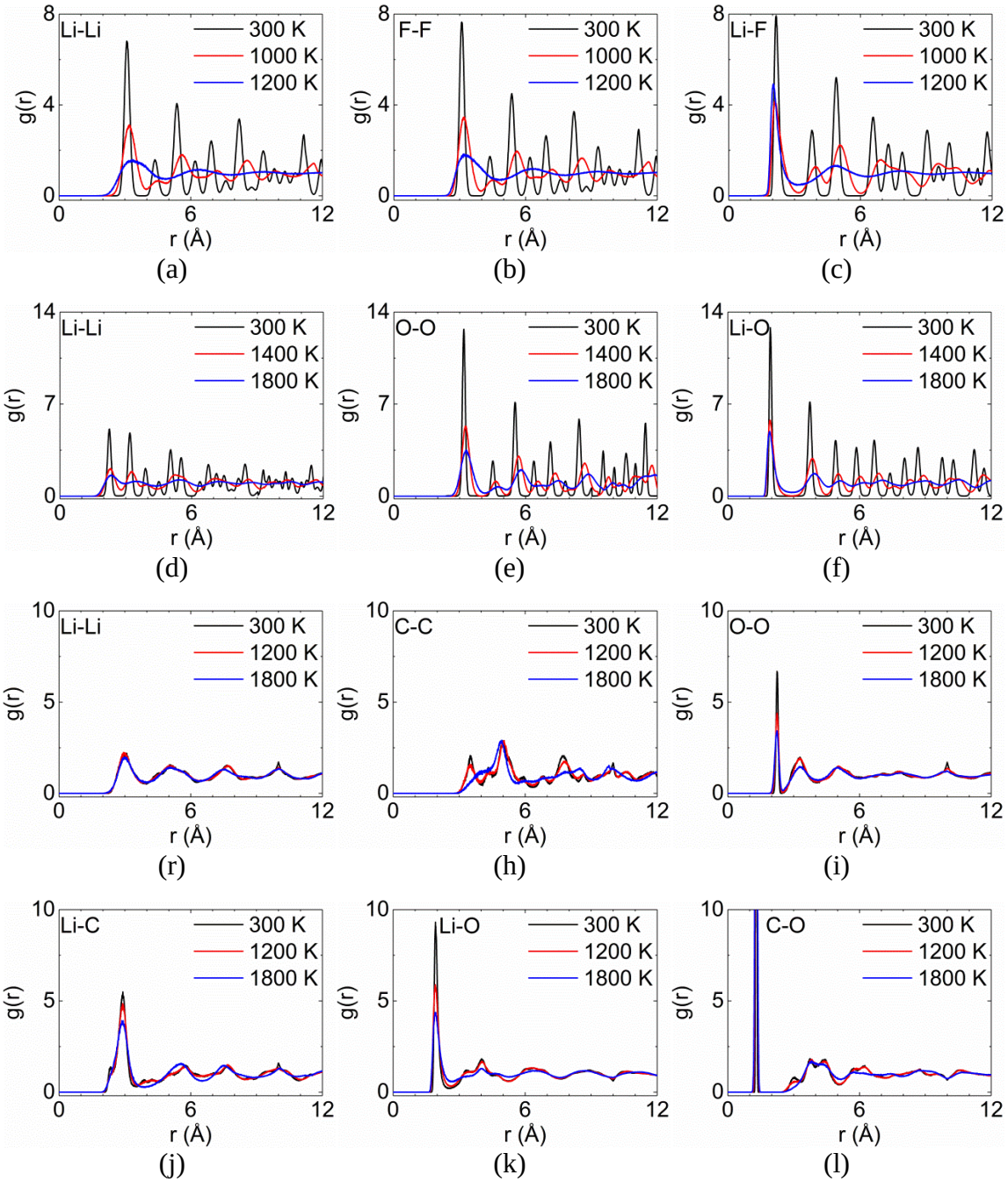

Figure 4.6. Selected radial distribution functions of LiF, Li_2O and Li_2CO_3 at various temperatures. For LiF at 300 K, 1000 K and 1200 K: (a) Li-Li, (b) F-F, and (c) Li-F. For Li_2O at 300 K, 1400 K and 1800 K: (d) Li-Li, (e) O-O, and (f) Li-O. For Li_2CO_3 at 300K, 1200 K and 1800 K: (g) Li-Li, (h) C-C, (i) O-O, (j) Li-C, (k) Li-O, and (l) C-O. Snapshots used to calculate RDF's are taken every 2 ps during 1000 ps temperature equilibrations using NPT ensemble.

After vacancies and interstitial are introduced in each SEI product, the lithium ion diffusion coefficients for each case are obtained from the slope of the MSD curves. Coefficient values for each temperature below 400 K are tabulated in Table 4.4. At 300 K, for Li^+ diffusion in LiF it is $D = 3.93\times10^{-16}$ m^2/s which is in the range of values (10^{-26} m^2/s and 10^{-16} m^2/s) that have been reported for diffusion of Li in LiF found using phase-field, molecular dynamics and NEB methods.[24, 150, 185] Similarly, the Li-ion diffusion in Li_2O is $D = 4.01\times10^{-16}$ m^2/s at 300 K, which is also within the range (10^{-20} m^2/s and 10^{-16} m^2/s) of published theoretical values of diffusivity of Li in Li_2O obtained also by phase-field method and molecular dynamics.[24, 185] For Li_2CO_3 at 300 K, $D = 3.3\times10^{-16}$ m^2/s, which is one order of magnitude smaller than the reported values (10^{-15} and 10^{-12} m^2/s) of diffusion of Li in Li_2CO_3 found by NEB and molecular dynamics studies.[174, 185] Moreover, all of the results at 300 K are within the range of values (10^{-18} and 10^{-14} m^2/s) of diffusion of Li in amorphous silicon that have been experimentally found.[66, 220-221]

Table 4.4. Diffusion Coefficients for Li-ion in LiF, Li_2O and Li_2CO_3.

Temperature	Diffusion Coefficient (D) (m^2/s)		
(K)	LiF	Li_2O	Li_2CO_3
250	6.83×10^{-17}	1.71×10^{-18}	1.00×10^{-16}
275	1.12×10^{-15}	1.74×10^{-16}	7.11×10^{-16}
300	3.93×10^{-16}	4.01×10^{-16}	3.30×10^{-16}
325	1.22×10^{-15}	5.30×10^{-16}	9.14×10^{-15}
350	7.10×10^{-16}	6.92×10^{-16}	6.73×10^{-14}
375	4.64×10^{-17}	1.10×10^{-16}	1.08×10^{-15}
400	1.07×10^{-15}	3.63×10^{-16}	1.68×10^{-14}

At low temperatures, mainly the atom vibrations due to the increased temperature are observed and no diffusion hopping events during the simulation time are seen. On the contrary, at high temperatures, Li-ion diffusion can be clearly observed. Sample snapshots of Li-ion diffusion are presented in Figure 4.7. Diffusion mechanisms observed in the simulations include both vacancy assisted and knock-off diffusion in LiF. This agrees with previous theoretical results that found vacancy diffusion more favorable than interstitial diffusion.[150] The diffusion mechanism observed in Li_2O is direct exchange, where two neighboring ions move simultaneously. A similar mechanism, ring diffusion, was found in a recent study.[197]

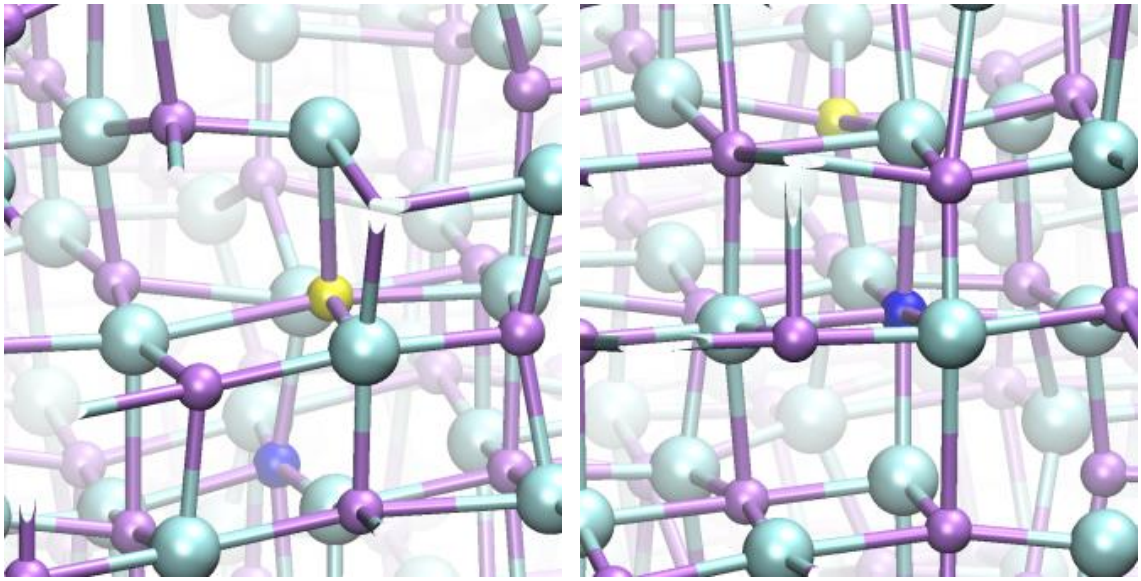

(a) (b)

Figure 4.7. Li-ion diffusion in (a-b) LiF, (c-d) Li_2O and (e-f) Li_2CO_3 at high temperatures. Initial (a,c,e) and final (b,d,f) position of Li-ions. Li (purple, blue, yellow), F (cyan), O (red), C (brown).

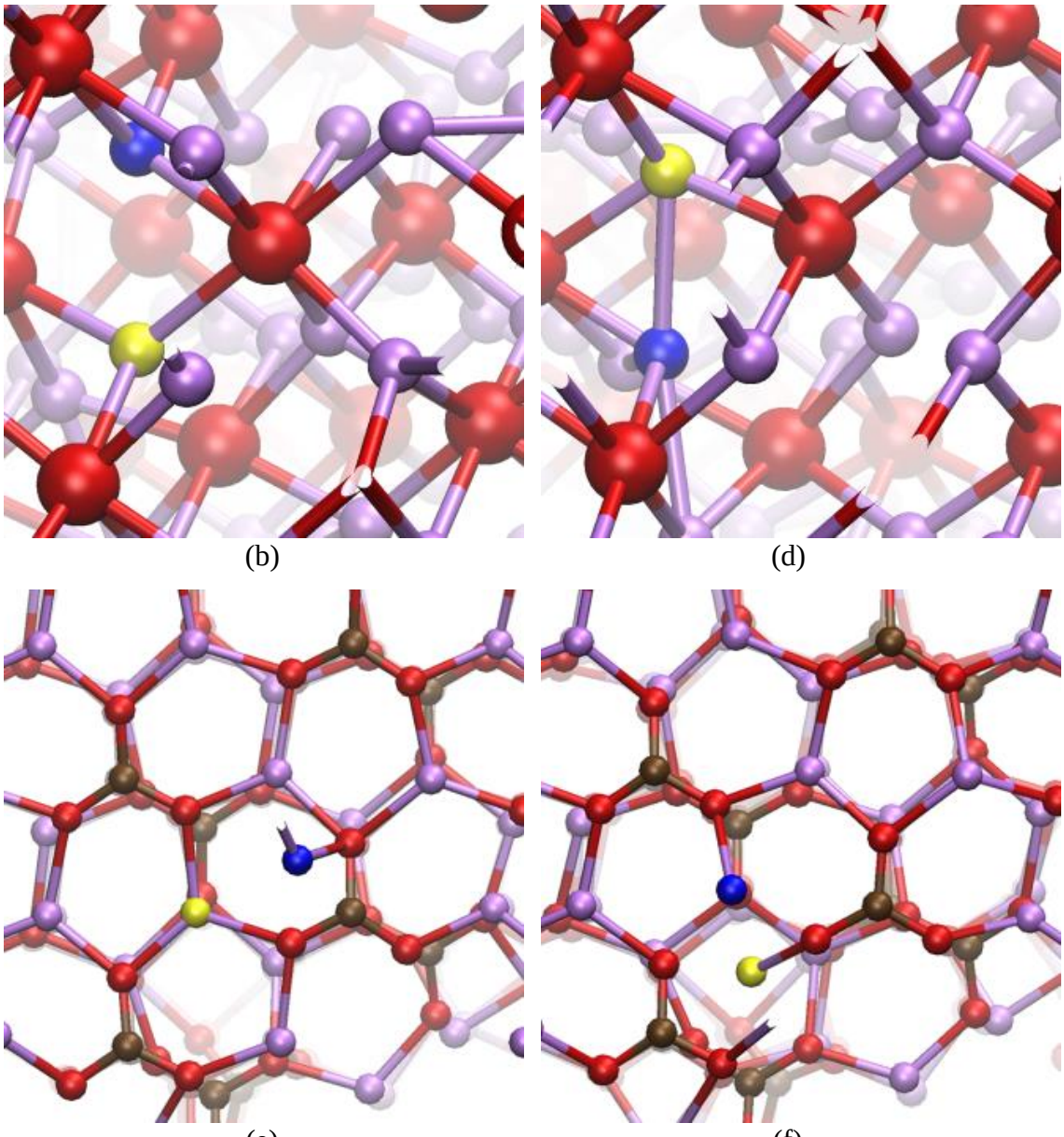

(b) (d)

(e) (f)

Figure 4.7. Continued.

Vacancy and knock-off diffusion mechanisms are observed in Li_2CO_3; in contrast, a previous theoretical study found that interstitial Li^+ ions are the main carriers,[175] but also that this interstitial Li^+ moves via knock off mechanism. In LiF case, shown in Figure 4.7(a), a Li-ion (blue) displaces a Li-ion (yellow) that is able to move to a neighbor vacant site. In Li_2O, presented in Figure 4.7(b), direct exchange, where two neighboring ions (blue and yellow) move simultaneously, is observed. Figure 4.7(c) shows the knock-off mechanism observed in Li_2CO_3, where a Li interstitial ion (blue) removes a Li-ion (yellow) from its original site.

The temperature dependence of diffusion coefficients follows the Arrhenius equation[222] given by

$$D = D_0 e^{-E_a/RT} \tag{4.7}$$

where D_0 is a pre-exponential factor for the diffusion coefficient, E_a is the diffusion activation energy, T is the temperature and R is the ideal gas constant. The activation energy E_a can be found from the negative slope of the Arrhenius plot, and the intercept of the line can be used to determine the temperature-independent pre-factor D_0. Figure 4.8 shows the ln(D) as function of 1/T obtained from the diffusion coefficient results. First, at temperatures from 250 K to 650 K, the diffusion coefficients are very low; a dependency on temperature is not observed. As mentioned before, only atom vibrations are observed in the simulations.

Second, at high temperatures, it can be observed in all cases, LiF, Li_2O and Li_2CO_3, that the diffusion coefficients increase as the temperature increases. Moreover, the LiF and Li_2O results are comparable to the experimental values and other MD

results.[178, 189, 193-196] Furthermore, the diffusion coefficients of Li^+ at high temperatures ranged from 700 K to 1800 K are higher than the low temperature results by at least five orders of magnitude; this is expected since the movement of atoms is usually higher in liquid phase than in solid phase.

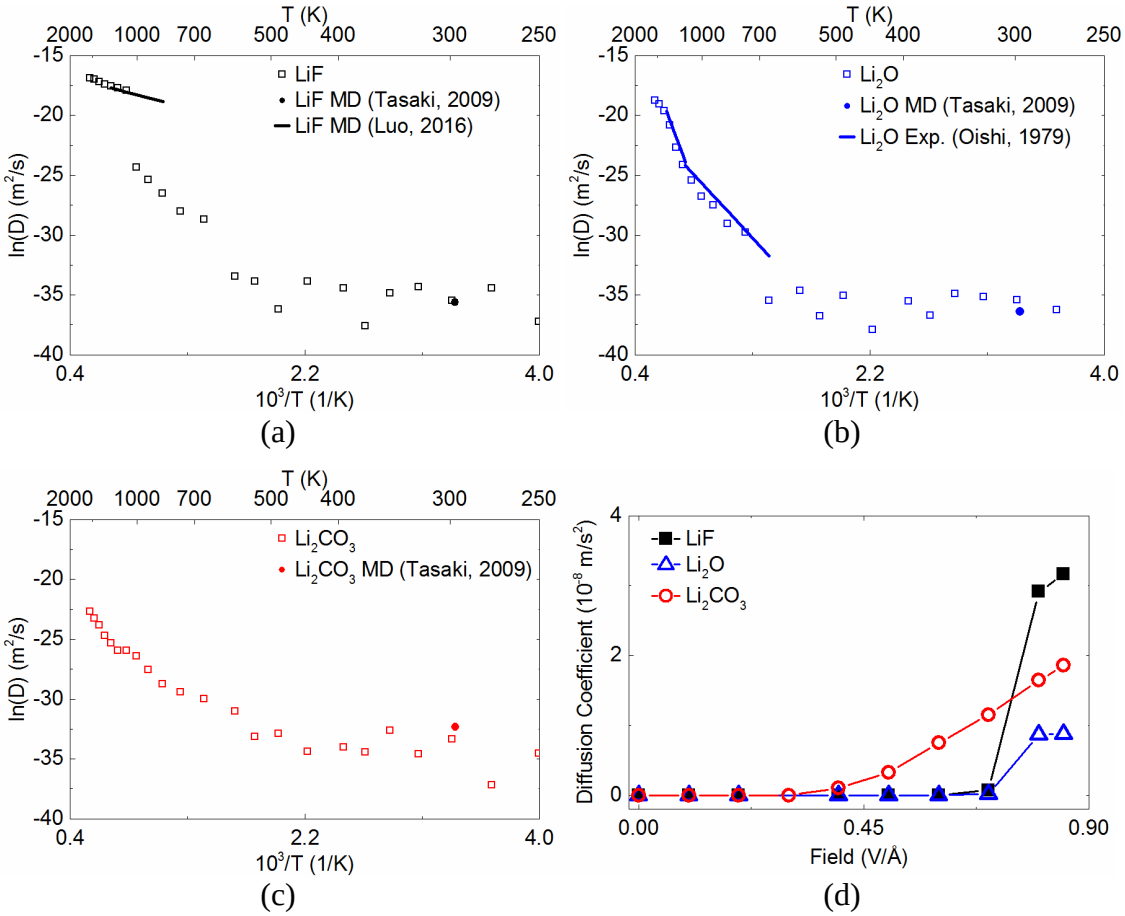

Figure 4.8. The ln(D) versus 1/T for (a) LiF, (b)Li_2O, and (c) Li_2CO_3. (d) Diffusion coefficient versus applied electric field for all SEI products. Results from molecular dynamics (solid circles) and experimental studies (solid lines) previously reported by others are shown for comparison in (a) LiF,[178, 185] (b) Li_2O,[185, 196] and (c) Li_2CO_3.[185]

The diffusion pre-exponential factor (D_0) and activation energy E_a obtained from the linear fit of the Arrhenius plot for all SE products studied are summarized in Table 4.5. Results at low temperature show that the activation energy in LiF is the smallest of the three samples studied, followed by Li_2O then Li_2CO_3. The results for the LiF and Li_2CO_3 activation energy, E_a = 0.04 eV and E_a = 0.12 eV, are below the values obtained experimentally and by other MD studies.[64, 174, 176-177, 198] On the contrary, the Li_2O energy result, E_a = 0.22 eV, is within the already reported values. [64, 176] At high temperatures, LiF still has activation energy, E_a = 0.32 eV, lower than Li_2O, E_a = 2.3 eV, even above 1300 K where Li_2O presents superionic conductivity.

Table 4.5. Diffusion Pre-factor (D_0) and Diffusion Activation Energy (E_a) for LiF, Li_2O and Li_2CO_3 at Low Temperatures and High Temperatures.

Temperature Range	SEI Product	Reference	D_0 (m^2/s)	E_a (eV)
Low Temperature 250 K - 400 K	LiF	This work	1.8×10^{-15}	0.04
		Other[64, 176-177]		0.65-0.80
	Li_2O	This work	5.4×10^{-13}	0.22
		Other[64, 176]		0.15-0.34
	Li_2CO_3	This work	7.6×10^{-13}	0.12
		Other[63-64, 174-175, 198]		0.23-0.80
High Temperature 1300 K - 1800 K	LiF	This work	3.5×10^{-7}	0.32
		Other[178, 184]	1.6×10^{-8}	0.25-1.86
	Li_2O	This work	3.1×10^{-2}	2.30
		Exp.[196]	4.1×10^{-1}	2.5
	Li_2CO_3	This work	7.3×10^{-6}	1.34

In addition, the LiF and Li_2O results for the diffusion pre-factor (D_0) are within one order of magnitude of the published values, and the results for the activation energy are close to values obtained by other studies.[178, 196]

For Li_2CO_3 case, in the temperature range of 1300 K to 1800 K the activation energy is E_a = 1.34 eV. Moreover, the slope changes at approximately 650 K and 1000 K which corresponds to a phase transformation and melting of Li_2CO_3.[218-219] To the best of my knowledge, no studies have reported on diffusion of Li^+ in Li_2CO_3 at high temperatures. In summary, our results at high temperatures are closer to those from previous works. However, in the case of low temperatures, the discrepancies can be due to the fact that less diffusion events occur and it becomes more difficult to calculate the actual diffusion coefficients since the error in the calculation increases as the temperature decreases.

An electric field is then applied to the sample and the diffusion coefficients are calculated at 300 K. As the electric field is increased, Li-ion diffusion exponentially increases as observed in Figure 4.8(d). Li-ion diffusion is clearly observed in the simulations at 0.4 V/Å in Li_2CO_3 and at 0.7 V/Å in both LiF and Li_2O. Coefficients at these fields are at least five orders of magnitude greater than those where no field is applied (Table 4.4). Shi et al.[174] reported coefficients close to 10^{-12} m^2/s for Li_2CO_3 at a voltage range from 0 to 4.4V. For the same voltage range, which corresponds to electric fields from 0 to 0.18 V/Å, the diffusion coefficient values are found to be between 10^{-14} and 10^{-13} m^2/s.

Diffusion events observed in the simulations consist of Li^+ ions moving mainly via knock-off diffusion in LiF, where multiple Li^+ ions knock-off their nearest neighbors in a cascade manner in the direction of the electric field. In the LiF case, shown in Figure 4.9(a), first a Li^+ ion (green) starts a chain movement of Li^+ ions (purple, orange and yellow) as indicated by the top set of arrows; then in a subsequent simulation step, another Li^+ ion (red) starts a second chain of displacements as indicated by the bottom set of arrows. Li^+ ions move in Li_2O from one lattice site to an empty one in sequence, as well as multiple Li^+ ions move simultaneously in the direction of the applied field. Shown in Figure 4.9(b), first a Li^+ ion (top orange and bottom yellow) moves to a vacant site, consequently the other Li^+ ions move, both individually and in pairs, in the direction of the electric field. No studies were found in the literature that study LiF and Li_2O diffusion mechanisms under an applied electric field. In Li_2CO_3, the diffusion mechanism observed is a combined vacancy-interstitial diffusion, shown in Figure 4.9(c). First a Li^+ ion (yellow) moves slightly from its lattice position thus allowing another Li^+ ion (blue) to easily take its place and further displace it to an interstitial position; then in a subsequent step another Li^+ ion (green) moves to a vacant site, and the Li-ion in the interstitial position (yellow) moves accordingly as indicated in the arrows. The observed mechanism in Li_2CO_3 fully agrees with Shi et al.[174] who found that above ~4 V, vacancy diffusion dominates Li-ion diffusion but diffusion through interstitials is also energetically favorable; vacancy and interstitial formation energies are ~0.6 eV and 1 eV, respectively. Notice that 4 V corresponds to an electric field of ~0.17 V/Å in this Li_2CO_3 box as its length in the field direction is 24 Å.

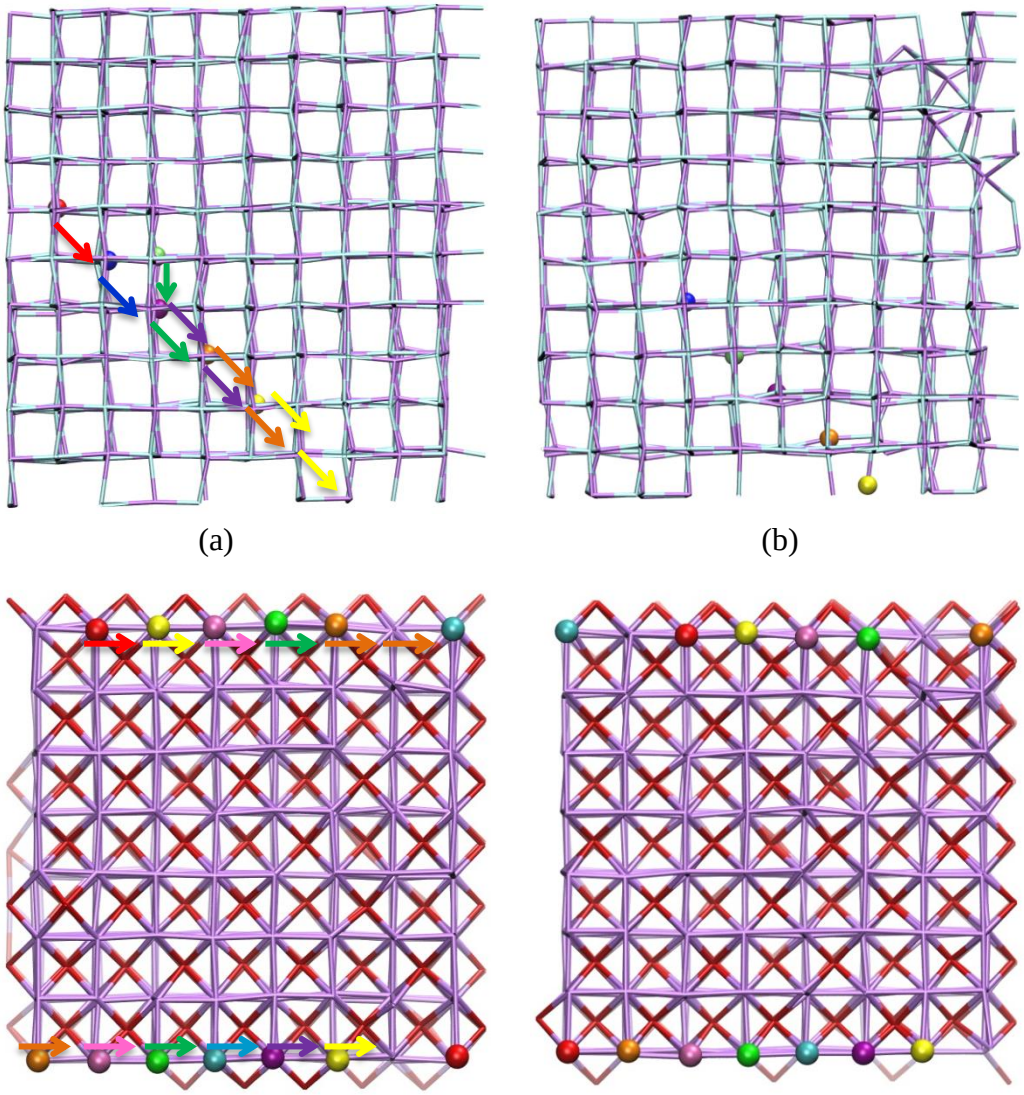

Figure 4.9. Snapshots of initial (a,c,e) and final (b,d,f) positions of Li^+ ions to show diffusion displacement in (a-b) LiF, (c-d) Li_2O and (e-f) Li_2CO_3 when an electric field is applied. Li^+ ions (multiple colors), F (cyan), O (red), C (brown).

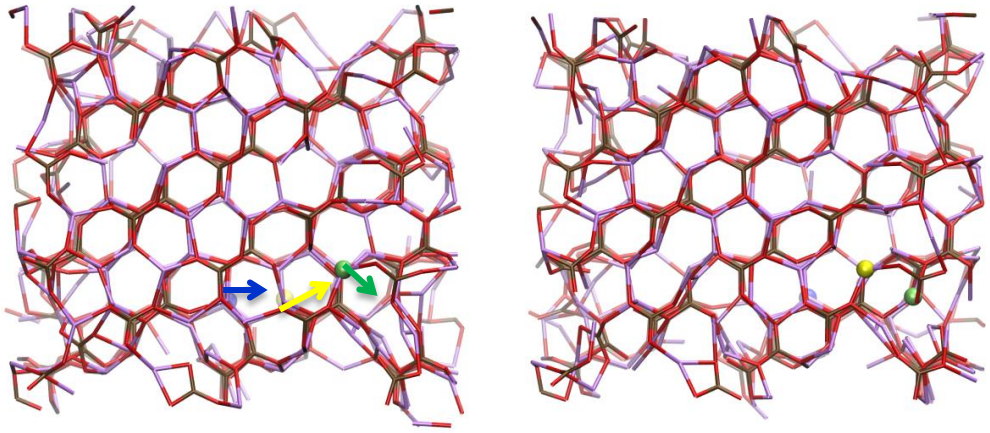

(e) (f)

Figure 4.9. Continued.

The total energy and temperature profiles are analyzed for each of the SEI samples at different applied electric fields. In the case of LiF, shown in Figure 4.10(a-b), the energy slightly increases as the electric field is increased to 0.6 V/Å, then at 0.7 V/Å, 0.8 V/Å and 0.85 V/Å a significant increase in the energy occurs, which goes from -73 Gcal/mol to -68 Gcal/mol. An increase in the temperature of the sample is also observed when 0.7 V/Å, 0.8 V/Å and 0.85 V/Å electric fields are applied to the sample. In the case of the Li_2O, shown in Figure 4.10(c-d), a large variation in the energy at the beginning of the simulation is also observed, as explained previously. Then at 300K, when the electric field is applied the energy remains at -113 Gcal/mol up to 0.7 V/Å, then at 0.8 V/Å and 0.85 the energy jumps to -110 Gcal/mol. An increase in the temperature of the sample is also observed when 0.8 V/Å and 0.85 V/Å are applied to the sample.

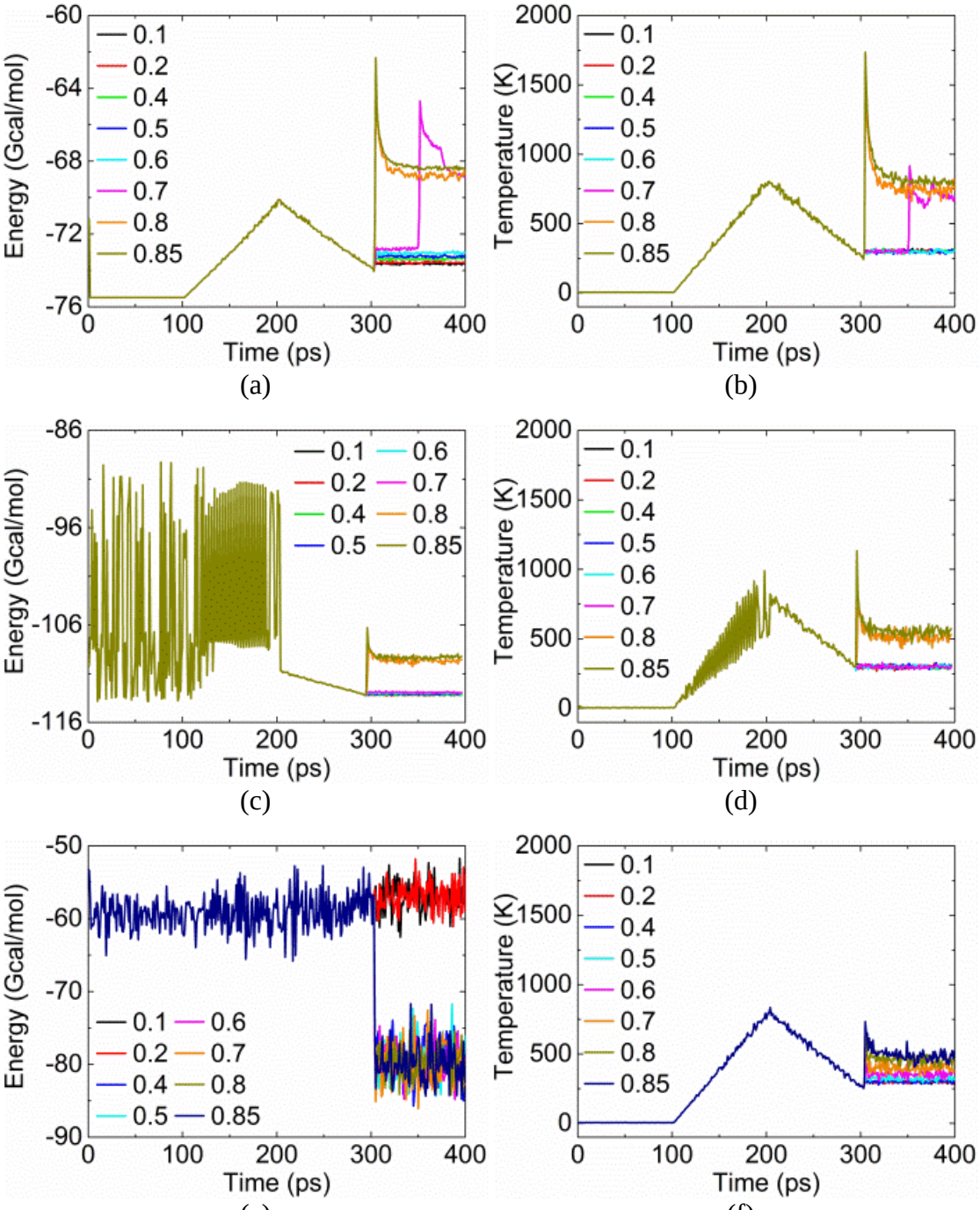

Figure 4.10. Energy versus time curves (left) and Temperature versus time curves (right) for samples with applied electric fields in the range from 0 V/Å to 0.85 V/Å. (a-b) LiF with a vacancy defect ratio of 2/1000, (c-d) Li_2O with a vacancy defect ratio of 3/798, and (e-f) Li_2CO_3 with interstitial defect ratio of 1/864.

In the case of Li_2CO_3, shown in Figure 4.10(e-f), the energy of the samples remain at -60 Gcal/mol up to 0.2 V/Å, then from 0.4 V/Å to 0.85 V/Å the energy decreases to and stays at -80 Gcal/mol. The temperature of the sample stays at 300 K up to 0.4 V/Å then from 0.5 V/Å to 0.85 V/Å, it slowly increases from 300 K to 500K. When comparing the results of the SEI products analyzed, it can be observed that in the LiF and Li_2O cases the energy of the sample increases as the electric field applied is increased. However, in the Li_2CO_3 case, the contrary occurs with the energy of the sample decreasing when an electric field is applied. This may be due to the defect types created in the sample. In the LiF and Li_2O cases vacancies are introduced whereas in the Li_2CO_3 sample an interstitial Li atom with a positive charge is introduced.

Selected representative RDF curves for the different atom pairs of Li_2CO_3 at various applied electric fields are presented in Figure 4.11. These distribution plots are taken during a 100 ps temperature equilibration at 300 K in different simulation runs for each applied field. Each atom pair distribution plot includes curves for 0, 0.4, and 0.85 V/Å in black, red and blue respectively. In all atom pair cases, RDF curves for 0.1 and 0.2 V/Å are equal to the 0 V/Å curve. Characteristic peaks representing the crystalline structure are observed, and the intensity of the peaks and their widths do not change as the field is increased. At 0.4 V/Å, the RDF curves are clearly different from those at lower electric fields. In the case of Li-Li, O-O and Li-O, the peaks can still be observed yet they are broader and their intensity is decreased. In the rest of the atom pairs, C-C, Li-C, and C-O, the changes are more significant.

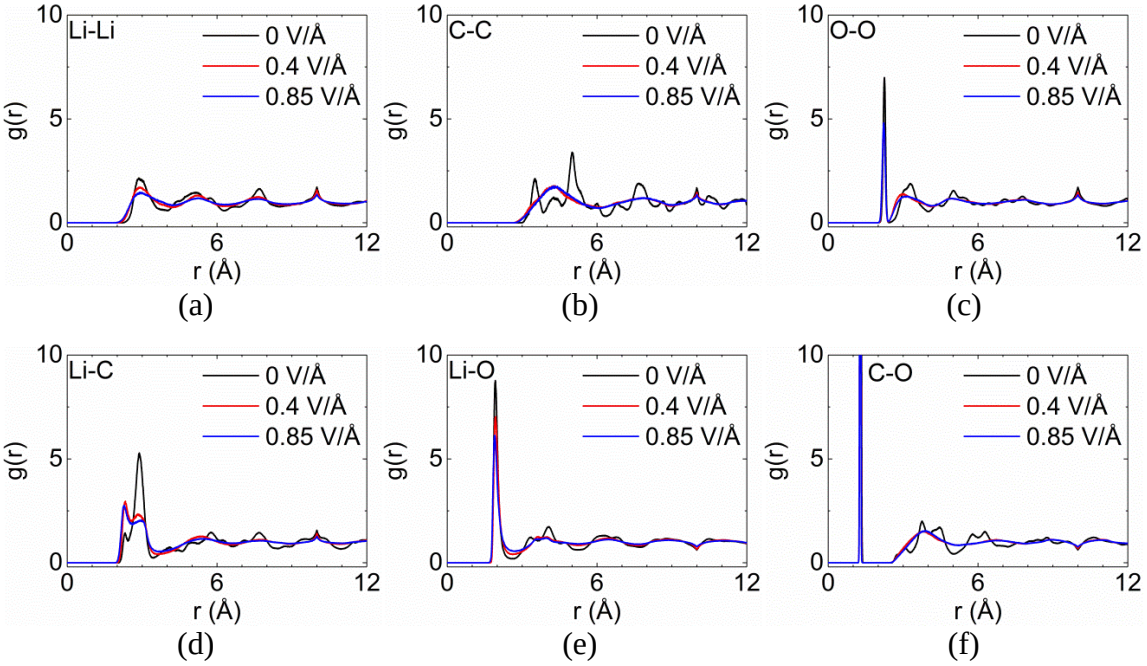

Figure 4.11. Selected radial distribution functions of Li_2CO_3 at various applied electric fields. (a) Li-Li, (b) C-C, (c) O-O, (d) Li-C, (e) Li-O, and f) C-O. Snapshots used to calculate RDF's are taken every 0.1 ps during a 100 ps temperature equilibration at 300 K using NPT ensemble.

In C-C distribution plot the characteristic peaks at 3.5, 4.3 and 5 Å combine and make a broad peak at 4.3 Å, similarly the peak at 7.6 Å combines with smaller peaks at 6.9 and 8.6 Å and form a very broad peak at 7.9 Å. In Li-C, the intensity of the first peak at 2.3 Å increases and the intensity of the second peak at 2.8 Å decreases; the rest of the peaks combine and make broad peaks. In the C-O distribution plot the characteristic peak at 1.29 Å remains very similar, only a small decrease in intensity is observed; individual peaks at 3 Å, 3.75 Å and 4.4 Å combine a form a broad peak at 3.83; similarly, the rest of the peaks in the distribution plot combine and form broader peaks.

As the electric field is increased from 0.4 to 0.85 V/Å, no significant changes occur; only a very small decrease in the first peak intensity is observed in Li-Li, Li-C and Li-O distribution plots.

4.5. Conclusions

Classical molecular dynamics simulations were used to obtain the diffusion coefficients of Li-ion in the three main components of the solid electrolyte interphase found in Li-ion batteries. Suitable force fields were successfully evaluated by comparing the resulting bond distances of each SEI structure at 300 K. In all SEI compounds the resulting bond distances were within ±0.2 Å of experimental results. Then the radial distribution functions of atom pairs in each structure were calculated in a wide range of temperatures from 250 K to 1800 K. Melting temperatures obtained for both LiF and Li_2CO_3 were very close to the experimental results; the result for Li_2O was higher than the experimental value. The mean square displacements of Li-ions in LiF, Li_2O and Li_2CO_3 were obtained and the diffusion coefficients over the operating temperature range of 250 K to 400 K for LIB were found. Since most of the experimental diffusion measurements are done at high temperature, diffusion coefficients at temperatures ranging from 600 K to 1800 K were also found. Simulation results showed that Li-ion diffusion coefficients at 300 K are 3.93×10^{-16} m^2/s, 4.01×10^{-16} m^2/s, and $4.90X10^{-17}$ m^2/s for LiF, Li_2O and Li_2CO_3, respectively. These results are comparable with available experimental data and other computational results. In addition, the diffusion coefficients were fitted to the Arrhenius equation, and the activation energies (E_a) and pre-exponential factors (D_0) were obtained. Activation energies found at low temperatures

are close to those previously obtained by others experimentally and theoretically. At high temperatures the pre-factor values and activation energies obtained were 3.5×10^{-7} m^2/s and 0.32 eV for LiF, 3.1×10^{-2} m^2/s and 2.3 eV for Li_2O, and 7.3×10^{-6} m^2/s and 1.34 eV for Li_2CO_3. These results are very close to the available literature results. Moreover, the diffusion mechanisms observed were vacancy assisted and knock-off diffusion in LiF, direct exchange in Li_2O, and vacancy and knock-off in Li_2CO_3. These findings generally agree with previous theoretical results. The effect of an applied electric field in the diffusion coefficients and the diffusion mechanisms was also analyzed. Diffusion coefficients increased exponentially with the increase of the electric field, and diffusion of Li-ions observed under the applied electric field occurred via knock-off in LiF, and via vacancies in Li_2O and in Li_2CO_3. Whereas no studies were found of Li-ion diffusion in LiF or Li_2O under an applied electric field, the diffusion coefficient and mechanism obtained in Li_2CO_3 case fully agrees with previous theoretical findings. Previously mentioned studies calculate diffusion coefficients only at room temperature, or only at very high temperatures, this work provides coefficients over a wider temperature range from 250 K to 1800 K. Furthermore, the evaluated force field parameters can be used in this range of temperatures to further study lithium ion transport in structures combining two or more SEI products using classical molecular dynamics simulations.

5. SUMMARY

This study investigated the electron transport and ion diffusivity through the solid electrolyte interphase compounds found in lithium-ion batteries (LIB) with silicon anodes. Key findings are summarized below.

In Section 2, the electron transfer through two model interfacial SEI components are characterized: EC-$(LiF)_x$-Li_xSi_y and EC-$(Li_2O)_x$-Li_xSi_y. Three degrees of lithiation for the electrode are studied: Si, LiSi, and Li. Results indicate that, in all Li_xSi_y cases, the current is significantly reduced with the addition of the SEI components as compared with the samples where no SEI element is present. It is also found that at high voltages of ~5, Li_2O films allow a higher electron transfer than LiF films. Moreover, it is found that separating the fragments at Van der Waals distances results in lower currents, thus implying lower electron transfer rates. Moreover, increasing the thickness of the SEI layer reduces the electron transfer exponentially; yet, a finite small current is still found even at large film thicknesses.

In Section 3, the electron transport on Li_2CO_3, Si_2O and $Li_2Si_2O_5$ is investigated in four lithiation stages of the Si anode using the DFT-GF approach presented in Section 1 to understand early stages of SEI nucleation and growth. Similar results to those in Section 2 are found: significant reduction of the current with the addition of any SEI component in comparison to samples where no SEI is present; further reduction of the electron transfer as the SEI layer thickness is increased; at high voltages of ~5 V, $Li_2Si_2O_5$ presents a much higher resistance to electron transfer than Li_2CO_3 and SiO_2;

exponential decrease of the current as the SEI layer thickness increases. Moreover, HOMO-LUMO gaps for all SEI products and oxides are calculated. It was observed, in all samples, that increasing the SEI layer reduces the HOMO-LUMO gap.

In Section 4, classical molecular dynamics simulations are used to obtain the diffusion coefficients of Li-ion in the three main components of the solid electrolyte interphase found in Li-ion batteries. The mean square displacements of Li-ions in LiF, Li_2O and Li_2CO_3 are obtained and the diffusion coefficients over the operating temperature range of 250 K to 400 K for LIB are found. Since most of the experimental diffusion measurements are done at high temperature, diffusion coefficients at temperatures ranging from 600 K to 1800 K are also found. Simulation results show that Li-ion diffusion coefficients at 300 K are 3.93×10^{-16} m^2/s, 4.01×10^{-16} m^2/s, and $4.90X10^{-17}$ m^2/s for LiF, Li_2O and Li_2CO_3, respectively. At high temperatures the pre-factor values and activation energies obtained were 3.5×10^{-7} m^2/s and 0.32 eV for LiF, 3.1×10^{-2} m^2/s and 2.3 eV for Li_2O, and 7.3×10^{-6} m^2/s and 1.34 eV for Li_2CO_3. Moreover, the diffusion mechanisms observed were vacancy assisted and knock-off diffusion in LiF, direct exchange in Li_2O, and vacancy and knock-off in Li_2CO_3. The effect of an applied electric field in the diffusion coefficients and the diffusion mechanisms is also analyzed. Diffusion coefficients increased exponentially with the increase of the electric field, and diffusion of Li-ions observed under the applied electric field occurred via knock-off in LiF, and via vacancies in Li_2O and in Li_2CO_3.

The following recommendations on future studies are suggested to further increase the understanding of the SEI in lithium-ion batteries and/or expand and

accelerate their improvement. First, the DFT-GF approach utilized in Section 2 and Section 3 to find the electron transport characteristics is a very practical and versatile tool. Within the lithium-ion batteries area, it can be used to study schemes where the anode is changed i.e. to sulfur (S); or to study models where, instead of EC as the electrolyte, PC or DEC are used. Furthermore, the force field parameters presented in Section 4 can be used in classical molecular dynamics simulations to further study lithium ion transport in structures combining two or more SEI products in a wide temperature range from 250 K to 1800 K. Moreover, similar diffusion studies can be done in models arising from solid-state batteries, where the electrolyte is replaced with a solid material.

REFERENCES

1. Nitta, N.; Wu, F.; Lee, J. T.; Yushin, G., Li-Ion Battery Materials: Present and Future. *Mater. Today* **2014**, *18*, 252–264.

2. Tarascon, J. M.; Armand, M., Issues and Challenges Facing Rechargeable Lithium Batteries. *Nature* **2001**, *414*, 359-367.

3. Tarascon, J. M., Key Challenges in Future Li-Battery Research. *Philos. Trans. R. Soc., A* **2010**, *368*, 3227-3241.

4. Manthiram, A., Materials Challenges and Opportunities of Lithium Ion Batteries. *J. Phys. Chem. Lett.* **2011**, *2*, 176-184.

5. Sasaki, T.; Ukyo, Y.; Novák, P., Memory Effect in a Lithium-Ion Battery. *Nat. Mater.* **2013**, *12*, 569-575.

6. Miranda, D.; Costa, C. M.; Lanceros-Mendez, S., Lithium Ion Rechargeable Batteries: State of the Art and Future Needs of Microscopic Theoretical Models and Simulations. *J. Electroanal. Chem.* **2015**, *739*, 97-110.

7. Chen, J.; Buhrmester, C.; Dahn, J. R., Chemical Overcharge and Overdischarge Protection for Lithium-Ion Batteries. *Electrochem. Solid-State Lett.* **2005**, *8*, A59-A62.

8. Etacheri, V.; Marom, R.; Elazari, R.; Salitra, G.; Aurbach, D., Challenges in the Development of Advanced Li-Ion Batteries: A Review. *Energy Environ. Sci.* **2011**, *4*, 3243-3262.

9. Arora, P.; White, R. E.; Doyle, M., Capacity Fade Mechanisms and Side Reactions in Lithium-Ion Batteries. *J. Electrochem. Soc.* **1998**, *145*, 3647-3667.

10. Amine, K.; Kanno, R.; Tzeng, Y., Rechargeable Lithium Batteries and Beyond: Progress, Challenges, and Future Directions. *MRS Bull.* **2014**, *39*, 395-401.

11. Thomas, C. E., Fuel Cell and Battery Electric Vehicles Compared. *Int. J. Hydrogen Energy* **2009**, *34*, 6005-6020.

12. Roberts, A.; Brooks, R.; Shipway, P., Internal Combustion Engine Cold-Start Efficiency: A Review of the Problem, Causes and Potential Solutions. *Energy Convers. Manage.* **2014**, *82*, 327-350.

13. Thackeray, M. M.; Thomas, J. O.; Whittingham, M. S., Science and Applications of Mixed Conductors for Lithium Batteries. *MRS Bull.* **2000**, *25*, 39-46.

14. Verma, P.; Maire, P.; Novák, P., A Review of the Features and Analyses of the Solid Electrolyte Interphase in Li-Ion Batteries. *Electrochim. Acta* **2010**, *55*, 6332-6341.

15. Roy, P.; Srivastava, S. K., Nanostructured Anode Materials for Lithium Ion Batteries. *J. Mater. Chem. A* **2015**, *3*, 2454-2484.

16. Stephan, A. M., Review on Gel Polymer Electrolytes for Lithium Batteries. *Eur. Polym. J.* **2006**, *42*, 21-42.

17. Tipton, W. W.; Bealing, C. R.; Mathew, K.; Hennig, R. G., Structures, Phase Stabilities, and Electrical Potentials of Li-Si Battery Anode Materials. *Phys. Rev. B: Condens. Matter* **2013**, *87*, 184114.

18. Chevrier, V. L.; Zwanziger, J. W.; Dahn, J. R., First Principles Studies of Silicon as Negative Electrode Material for Lithium-Ion Batteries. *Can. J. Phys.* **2009**, *87*, 625-632.

19. Kim, H.; Chou, C. Y.; Ekerdt, J. G.; Hwang, G. S., Structure and Properties of Li-Si Alloys: A First-Principles Study. *J. Phys. Chem. C* **2011**, *115*, 2514-2521.

20. Chou, C. Y.; Hwang, G. S., Surface Effects on the Structure and Lithium Behavior in Lithiated Silicon: A First Principles Study. *Surf. Sci.* **2013**, *612*, 16-23.

21. Su, X.; Wu, Q.; Li, J.; Xiao, X.; Lott, A.; Lu, W.; Sheldon, B. W.; Wu, J., Silicon-Based Nanomaterials for Lithium-Ion Batteries: A Review. *Adv. Ener. Mater.* **2014**, *4*, 1-23.

22. Zhang, J.; Wang, R.; Yang, X.; Lu, W.; Wu, X.; Wang, X.; Li, H.; Chen, L., Direct Observation of Inhomogeneous Solid Electrolyte Interphase on MnO Anode with Atomic Force Microscopy and Spectroscopy. *Nano Lett.* **2012**, *12*, 2153-2157.

23. Zheng, J.; Zheng, H.; Wang, R.; Ben, L.; Lu, W.; Chen, L.; Chen, L.; Li, H., 3D Visualization of Inhomogeneous Multi-Layered Structure and Young's Modulus of the Solid Electrolyte Interphase (SEI) on Silicon Anodes for Lithium Ion Batteries. *Phys. Chem. Chem. Phys.* **2014**, *16*, 13229-13238.

24. Guan, P.; Liu, L.; Lin, X., Simulation and Experiment on Solid Electrolyte Interphase (SEI) Morphology Evolution and Lithium-Ion Diffusion. *J. Electrochem. Soc.* **2015**, *162*, A1798-A1808.

25. Aurbach, D.; Zaban, A., Impedance Spectroscopy of Lithium Electrodes. Part 1. General Behavior in Propylene Carbonate Solutions and the Correlation to Surface Chemistry and Cycling Efficiency. *J. Electroanal. Chem.* **1993**, *348*, 155-179.

26. Aurbach, D.; Markovsky, B.; Shechter, A.; Ein-Eli, Y.; Cohen, H., A Comparative Study of Synthetic Graphite and Li Electrodes in Electrolyte Solutions Based on Ethylene Carbonate-Dimethyl Carbonate Mixtures. *J. Electrochem. Soc.* **1996**, *143*, 3809-3820.

27. Aurbach, D.; Levi, M. D.; Levi, E.; Schechter, A., Failure and Stabilization Mechanisms of Graphite Electrodes. *J. Phys. Chem. B* **1997**, *101*, 2195-2206.

28. Balbuena, P. B.; Wang, Y., *Lithium-Ion Batteries: Solid-Electrolyte Interphase*. Imperial College Press: London, 2004.

29. Zhang, H. L.; Li, F.; Liu, C.; Tan, J.; Cheng, H. M., New Insight into the Solid Electrolyte Interphase with Use of a Focused Ion Beam. *J. Phys. Chem. B* **2005**, *109*, 22205-22211.

30. Lee, Y. M.; Lee, J. Y.; Shim, H. T.; Lee, J. K.; Park, J. K., SEI Layer Formation on Amorphous Si Thin Electrode During Precycling. *J. Electrochem. Soc.* **2007**, *154*, A515-A519.

31. Xiao, X.; Lu, P.; Ahn, D., Ultrathin Multifunctional Oxide Coatings for Lithium Ion Batteries. *Adv. Mater.* **2011**, *23*, 3911-3915.

32. Nie, M.; Chalasani, D.; Abraham, D. P.; Chen, Y.; Bose, A.; Lucht, B. L., Lithium Ion Battery Graphite Solid Electrolyte Interphase Revealed by Microscopy and Spectroscopy. *J. Phys. Chem. C* **2013**, *117*, 1257-1267.

33. Wang, Y.; Nakamura, S.; Ue, M.; Balbuena, P. B., Theoretical Studies to Understand Surface Chemistry on Carbon Anodes for Lithium-Ion Batteries: Reduction Mechanisms of Ethylene Carbonate. *J. Am. Chem. Soc.* **2001**, *123*, 11708-11718.

34. Aurbach, D.; Zaban, A.; Schechter, A.; Ein-Eli, Y.; Zinigrad, E.; Markovsky, B., Study of Electrolyte Solutions Based on Ethylene and Diethyl Carbonates for Rechargeable Li Batteries I. Li Metal Anodes. *J. Electrochem. Soc.* **1995**, *142*, 2873-2882.

35. Peled, E.; Golodnitsky, D.; Ardel, G., Advanced Model for Solid Electrolyte Interphase Electrodes in Liquid and Polymer Electrolytes. *J. Electrochem. Soc.* **1997**, *144*, L208-L210.

36. Pinson, M. B.; Bazant, M. Z., Theory of SEI Formation in Rechargeable Batteries: Capacity Fade, Accelerated Aging and Lifetime Prediction. *J. Electrochem. Soc.* **2013**, *160*, A243-A250.

37. Wu, H.; Chan, G.; Choi, J. W.; Ryu, I.; Yao, Y.; McDowell, M. T.; Lee, S. W.; Jackson, A.; Yang, Y.; Hu, L., et al., Stable Cycling of Double-Walled Silicon Nanotube

Battery Anodes through Solid-Electrolyte Interphase Control. *Nat. Nanotechnol.* **2012**, *7*, 310-315.

38. Lin, Y. X.; Liu, Z.; Leung, K.; Chen, L. Q.; Lu, P.; Qi, Y., Connecting the Irreversible Capacity Loss in Li-Ion Batteries with the Electronic Insulating Properties of Solid Electrolyte Interphase (SEI) Components. *J. Power Sources* **2016**, *309*, 221-230.

39. Zhang, Z.; Fouchard, D.; Rea, J. R., Differential Scanning Calorimetry Material Studies: Implications for the Safety of Lithium-Ion Cells. *J. Power Sources* **1998**, *70*, 16-20.

40. Liang, B.; Liu, Y.; Xu, Y., Silicon-Based Materials as High Capacity Anodes for Next Generation Lithium Ion Batteries. *J. Power Sources* **2014**, *267*, 469-490.

41. Park, G.; Nakamura, H.; Lee, Y.; Yoshio, M., The Important Role of Additives for Improved Lithium Ion Battery Safety. *J. Power Sources* **2009**, *189*, 602-606.

42. Ogihara, N.; Igarashi, Y.; Kamakura, A.; Naoi, K.; Kusachi, Y.; Utsugi, K., Disordered Carbon Negative Electrode for Electrochemical Capacitors and High-Rate Batteries. *Electrochim. Acta* **2006**, *52*, 1713-1720.

43. Yazami, R.; Reynier, Y. F., Mechanism of Self-Discharge in Graphite-Lithium Anode. *Electrochim. Acta* **2002**, *47*, 1217-1223.

44. Zaghib, K.; Nadeau, G.; Kinoshita, K., Effect of Graphite Particle Size on Irreversible Capacity Loss. *J. Electrochem. Soc.* **2000**, *147*, 2110-2115.

45. Novák, P.; Panitz, J. C.; Joho, F.; Lanz, M.; Imhof, R.; Coluccia, M., Advanced in Situ Methods for the Characterization of Practical Electrodes in Lithium-Ion Batteries. *J. Power Sources* **2000**, *90*, 52-58.

46. Churikov, A. V., Transfer Mechanism in Solid-Electrolyte Layers on Lithium: Influence of Temperature and Polarization. *Electrochim. Acta* **2001**, *46*, 2415-2426.

47. Winter, M., The Solid Electrolyte Interphase - the Most Important and the Least Understood Solid Electrolyte in Rechargeable Li Batteries. *Z. Phys. Chem.* **2009**, *223*, 1395-1406.

48. Yoshida, T.; Takahashi, M.; Morikawa, S.; Ihara, C.; Katsukawa, H.; Shiratsuchi, T.; Yamaki, J. I., Degradation Mechanism and Life Prediction of Lithium-Ion Batteries. *J. Electrochem. Soc.* **2006**, *153*, A576-A582.

49. Edström, K.; Herstedt, M.; Abraham, D. P., A New Look at the Solid Electrolyte Interphase on Graphite Anodes in Li-Ion Batteries. *J. Power Sources* **2006**, *153*, 380-384.

50. Harks, P. P. R. M. L.; Mulder, F. M.; Notten, P. H. L., In Situ Methods for Li-Ion Battery Research: A Review of Recent Developments. *J. Power Sources* **2015**, *288*, 92-105.

51. Aurbach, D.; Ein-Eli, Y.; Chusid, O.; Carmeli, Y.; Babai, M.; Yamin, H., Correlation between the Surface Chemistry and the Performance of Li-Carbon Intercalation Anodes for Rechargeable `Rocking-Chair' Type Batteries. *J. Electrochem. Soc.* **1994**, *141*, 603-611.

52. Benitez, L.; Cristancho, D.; Seminario, J. M.; Martinez de la Hoz, J. M.; Balbuena, P. B., Electron Transfer through Solid-Electrolyte-Interphase Layers Formed on Si Anodes of Li-Ion Batteries. *Electrochim. Acta* **2014**, *140*, 250-257.

53. Soto, F. A.; Ma, Y.; Martinez De La Hoz, J. M.; Seminario, J. M.; Balbuena, P. B., Formation and Growth Mechanisms of Solid-Electrolyte Interphase Layers in Rechargeable Batteries. *Chem. Mater.* **2015**, *27*, 7990-8000.

54. Michan, A. L.; Leskes, M.; Grey, C. P., Voltage Dependent Solid Electrolyte Interphase Formation in Silicon Electrodes: Monitoring the Formation of Organic Decomposition Products. *Chem. Mater.* **2016**, *28*, 385-398.

55. Veith, G. M.; Doucet, M.; Baldwin, J. K.; Sacci, R. L.; Fears, T. M.; Wang, Y.; Browning, J. F., Direct Determination of Solid-Electrolyte Interphase Thickness and Composition as a Function of State of Charge on a Silicon Anode. *J. Phys. Chem. C* **2015**, *119*, 20339-20349.

56. Rejovitzky, E.; Di Leo, C. V.; Anand, L., A Theory and a Simulation Capability for the Growth of a Solid Electrolyte Interphase Layer at an Anode Particle in a Li-Ion Battery. *J. Mech. Phys. Solids* **2015**, *78*, 210-230.

57. Andersson, A. M.; Edström, K., Chemical Composition and Morphology of the Elevated Temperature SEI on Graphite. *J. Electrochem. Soc.* **2001**, *148*, A1100-A1109.

58. Andersson, A. M.; Abraham, D. P.; Haasch, R.; MacLaren, S.; Liu, J.; Amine, K., Surface Characterization of Electrodes from High Power Lithium-Ion Batteries. *J. Electrochem. Soc.* **2002**, *149*, A1358-A1369.

59. Kong, F.; Kostecki, R.; Nadeau, G.; Song, X.; Zaghib, K.; Kinoshita, K.; McLarnon, F., In Situ Studies of SEI Formation. *J. Power Sources* **2001**, *97-98*, 58-66.

60. Liu, X. H.; Huang, J. Y., In Situ TEM Electrochemistry of Anode Materials in Lithium Ion Batteries. *Energy Environ. Sci.* **2011**, *4*, 3844-3860.

61. Lu, P.; Harris, S. J., Lithium Transport within the Solid Electrolyte Interphase. *Electrochem. Commun.* **2011**, *13*, 1035-1037.

62. Veryovkin, I. V.; Tripa, C. E.; Zinovev, A. V.; Baryshev, S. V.; Li, Y.; Abraham, D. P., TOF SIMS Characterization of SEI Layer on Battery Electrodes. *Nucl. Instrum. Methods Phys. Res., Sect. B* **2014**, *332*, 368-372.

63. Dunstan, M. T.; Griffin, J. M.; Blanc, F.; Leskes, M.; Grey, C. P., Ion Dynamics in Li_2CO_3 Studied by Solid-State NMR and First-Principles Calculations. *J. Phys. Chem. C* **2015**, *119*, 24255-24264.

64. Chen, Y. C.; Ouyang, C. Y.; Song, L. J.; Sun, Z. L., Electrical and Lithium Ion Dynamics in Three Main Components of Solid Electrolyte Interphase from Density Functional Theory Study. *J. Phys. Chem. C* **2011**, *115*, 7044-7049.

65. Lee, B.; Lee, C. K.; Han, S.; Lee, J.; Hwang, C. S., First-Principles Calculation of Capacitance Including Interfacial Effects. *J. Appl. Phys.* **2008**, *103*, 24106.

66. Xie, J.; Imanishi, N.; Zhang, T.; Hirano, A.; Takeda, Y.; Yamamoto, O., Li-Ion Diffusion in Amorphous Si Films Prepared by RF Magnetron Sputtering: A Comparison of Using Liquid and Polymer Electrolytes. *Mater. Chem. Phys.* **2010**, *120*, 421-425.

67. Tritsaris, G. A.; Zhao, K.; Okeke, O. U.; Kaxiras, E., Diffusion of Lithium in Bulk Amorphous Silicon: A Theoretical Study. *J. Phys. Chem. C* **2012**, *116*, 22212-22216.

68. Wang, H.; Ji, X.; Chen, C.; Xu, K.; Miao, L., Lithium Diffusion in Silicon and Induced Structure Disorder: A Molecular Dynamics Study. *AIP Advances* **2013**, *3*, 112102.

69. Panchmatia, P. M.; Armstrong, A. R.; Bruce, P. G.; Islam, M. S., Lithium-Ion Diffusion Mechanisms in the Battery Anode Material $Li_{1+x}V_{1-x}O_2$. *Phys. Chem. Chem. Phys.* **2014**, *16*, 21114-21118.

70. Wang, Z.; Su, Q.; Deng, H.; He, W.; Lin, J.; Fu, Y. Q., Modelling and Simulation of Electron-Rich Effect on Li Diffusion in Group IVA Elements (Si, Ge and Sn) for Li Ion Batteries. *J. Mater. Chem. A* **2014**, *2*, 13976-13982.

71. Wu, M.; Xu, B.; Ouyang, C., Physics of Electron and Lithium-Ion Transport in Electrode Materials for Li-Ion Batteries. *Chin. Phys. B* **2015**, *25*, 018206.

72. Bhatt, M. D.; Cho, M.; Cho, K., Density Functional Theory Calculations and Ab Initio Molecular Dynamics Simulations for Diffusion of Li^+ within Liquid Ethylene Carbonate. *Modell. Simul. Mater. Sci. Eng.* **2012**, *20*, 065004.

73. Park, M.; Zhang, X.; Chung, M.; Less, G. B.; Sastry, A. M., A Review of Conduction Phenomena in Li-Ion Batteries. *J. Power Sources* **2010**, *195*, 7904-7929.

74. Yu, J.; Balbuena, P. B.; Budzien, J.; Leung, K., Hybrid DFT Functional-Based Static and Molecular Dynamics Studies of Excess Electron in Liquid Ethylene Carbonate. *J. Electrochem. Soc.* **2011**, *158*, A400-A410.

75. Ganesh, P.; Jiang, D. E.; Kent, P. R. C., Accurate Static and Dynamic Properties of Liquid Electrolytes for Li-Ion Batteries from Ab Initio Molecular Dynamics. *J. Phys. Chem. B* **2011**, *115*, 3085-3090.

76. Borodin, O.; Smith, G. D., Litfsi Structure and Transport in Ethylene Carbonate from Molecular Dynamics Simulations. *J. Phys. Chem. B* **2006**, *110*, 4971-4977.

77. Wang, Y.; Balbuena, P. B., Theoretical Studies on Cosolvation of Li Ion and Solvent Reductive Decomposition in Binary Mixtures of Aliphatic Carbonates. *Int. J. Quantum Chem.* **2005**, *102*, 724-733.

78. Wang, Y.; Balbuena, P. B., Combined Ab Initio Quantum Mechanics and Classical Molecular Dynamics Studies of Polyphosphazene Polymer Electrolytes: Competitive Solvation of Li^+ and $LiCF_3SO_3$. *J. Phys. Chem. B* **2004**, *108*, 15694-15702.

79. Van Der Ven, A.; Ceder, G., Lithium Diffusion in Layered Li_xCoO_2. *Electrochem. Solid-State Lett.* **2000**, *3*, 301-304.

80. Bogle, X.; Vazquez, R.; Greenbaum, S.; Cresce, A. V. W.; Xu, K., Understanding Li^+-Solvent Interaction in Nonaqueous Carbonate Electrolytes with ^{17}o NMR. *J. Phys. Chem. Lett.* **2013**, *4*, 1664-1668.

81. Borodin, O.; Smith, G. D., Quantum Chemistry and Molecular Dynamics Simulation Study of Dimethyl Carbonate: Ethylene Carbonate Electrolytes Doped with $LiPF_6$. *J. Phys. Chem. B* **2009**, *113*, 1763-1776.

82. Ong, M. T.; Verners, O.; Draeger, E. W.; Van Duin, A. C. T.; Lordi, V.; Pask, J. E., Lithium Ion Solvation and Diffusion in Bulk Organic Electrolytes from First-Principles and Classical Reactive Molecular Dynamics. *J. Phys. Chem. B* **2015**, *119*, 1535-1545.

83. Persson, K.; Sethuraman, V. A.; Hardwick, L. J.; Hinuma, Y.; Meng, Y. S.; Van Der Ven, A.; Srinivasan, V.; Kostecki, R.; Ceder, G., Lithium Diffusion in Graphitic Carbon. *J. Phys. Chem. Lett.* **2010**, *1*, 1176-1180.

84. Churikov, A. V.; Ivanishchev, A. V.; Ushakov, A. V.; Romanova, V. O., Diffusion Aspects of Lithium Intercalation as Applied to the Development of Electrode Materials for Lithium-Ion Batteries. *J. Solid State Electrochem.* **2014**, *18*, 1425-1441.

85. Van der Ven, A.; Bhattacharya, J.; Belak, A. A., Understanding Li Diffusion in Li-Intercalation Compounds. *Acc. Chem. Res.* **2013**, *46*, 1216-1225.

86. Schroeder, M.; Eames, C.; Tompsett, D. A.; Lieser, G.; Islam, M. S., Li_xFeF_6 (X = 2, 3, 4) Battery Materials: Structural, Electronic and Lithium Diffusion Properties. *Phys. Chem. Chem. Phys.* **2013**, *15*, 20473-20479.

87. Soetens, J.-C.; Millot, C.; Maigret, B., Molecular Dynamics Simulation of $Li^+BF_4^-$ in Ethylene Carbonate, Propylene Carbonate, and Dimethyl Carbonate Solvents. *J. Phys. Chem. A* **1998**, *102*, 1055-1061.

88. Borodin, O.; Bedrov, D., Interfacial Structure and Dynamics of the Lithium Alkyl Dicarbonate SEI Components in Contact with the Lithium Battery Electrolyte. *J. Phys. Chem. C* **2014**, *118*, 18362-18371.

89. Ogata, S.; Ohba, N.; Kouno, T., Multi-Thousand-Atom DFT Simulation of Li-Ion Transfer through the Boundary between the Solid-Electrolyte Interface and Liquid Electrolyte in a Li-Ion Battery. *J. Phys. Chem. C* **2013**, *117*, 17960-17968.

90. Leung, K., Electronic Structure Modeling of Electrochemical Reactions at Electrode/Electrolyte Interfaces in Lithium Ion Batteries. *J. Phys. Chem. C* **2013**, *117*, 1539-1547.

91. Borodin, O.; Zhuang, G. V.; Ross, P. N.; Xu, K., Molecular Dynamics Simulations and Experimental Study of Lithium Ion Transport in Dilithium Ethylene Dicarbonate. *J. Phys. Chem. C* **2013**, *117*, 7433-7444.

92. Colclasure, A. M.; Smith, K. A.; Kee, R. J., Modeling Detailed Chemistry and Transport for Solid-Electrolyte-Interface (SEI) Films in Li-Ion Batteries. *Electrochim. Acta* **2011**, *58*, 33-43.

93. Márquez, A.; Balbuena, P. B., Molecular Dynamics Study of Graphite/Electrolyte Interfaces. *J. Electrochem. Soc.* **2001**, *148*, A624-A635.

94. Tullo, A., Dell Recalls Lithium Batteries. *Chemical & Engineering News Archive* **2006**, *84*, 11.

95. Hales, P. Dell Laptop Explodes at Japanese Conference. http://web.archive.org/web/20070905234726/http://www.theinquirer.net/default.aspx?article=32550 (accessed 03-05-2015).

96. Wikinews. Nokia Issues Bl-5c Battery Warning, Offers Replacement. http://en.wikinews.org/wiki/Nokia_issues_BL-5C_battery_warning%2C_offers_replacement (accessed 03-05-2015).

97. Abada, S.; Marlair, G.; Lecocq, A.; Petit, M.; Sauvant-Moynot, V.; Huet, F., Safety Focused Modeling of Lithium-Ion Batteries: A Review. *J. Power Sources* **2016**, *306*, 178-192.

98. News., C. R. Nikon Recalls More Than 200,000 Camera Batteries Due to Burn Hazard. http://www.consumerreports.org/cro/news/2012/07/nikon-recalls-more-than-200-000-camera-batteries-due-to-burn-hazard/index.htm (accessed 03-05-2015).

99. Menkin, S.; Golodnitsky, D.; Peled, E., Artificial Solid-Electrolyte Interphase (SEI) for Improved Cycleability and Safety of Lithium–Ion Cells for EV Applications. *Electrochem. Commun.* **2009**, *11*, 1789-1791.

100. Datta, S., *Quantum Transport Atom to Transistor*; Cambridge University Press: Cambridge, New York, 2005.

101. Agapito, L. A. Conductance States of Molecular Junctions for Encoding Binary Information a Computational Approach. Ph.D. Dissertation, Texas A&M University, College Station, TX, 2010.

102. Paulsson, M., Non Equilibrium Green's Functions for Dummies: Introduction to the One Particle NEGF Equations. *arXiv preprint cond-mat/0210519* **2002**.

103. Maassen, J.; Harb, M.; Michaud-Rioux, V.; Zhu, Y.; Guo, H., Quantum Transport Modeling from First Principles. *Proceedings of the IEEE* **2013**, *101*, 518-530.

104. Stokbro, K., First-Principles Modeling of Electron Transport. *J. Phys.: Condens. Matter* **2008**, *20*, 064216.

105. Datta, S., Electrical Resistance: An Atomistic View. *Nanotechnology* **2004**, *15*, S433.

106. Sergueev, N.; Guo, H. In *NEGF-DFT: A First Principles Formalism for Modeling Molecular Electronics*, NRC Research Press: 2003.

107. Datta, S. In *The Non-Equilibrium Green's Function (NEGF) Formalism: An Elementary Introduction*, IEDm: International Electron Devices meeting, 2002; pp 703-706.

108. Brandbyge, M.; Mozos, J.-L.; Ordejón, P.; Taylor, J.; Stokbro, K., Density-Functional Method for Nonequilibrium Electron Transport. *Phys. Rev. B* **2002**, *65*, 165401.

109. Taylor, J.; Guo, H.; Wang, J., Ab Initio Modeling of Quantum Transport Properties of Molecular Electronic Devices. *Phys. Rev. B: Condens. Matter Mater. Phys.* **2001**, *63*, 2454071-24540713.

110. Foresman, J. B., *Exploring Chemistry with Electronic Structure Methods*; Gaussian, Inc.: Pittsburgh, PA, 1996.

111. Szabo, A.; Ostlund, N. S., *Modern Quantum Chemistry: Introduction to Advanced Electronic Structure Theory*; Dover Publications, 2012.

112. Seminario, J. M., Preface to Density Functional Theory. In *Theoretical and Computational Chemistry*, Seminario, J. M., Ed. Elsevier: 1996; Vol. 4, pp v-x.

113. Levy, M., Elementary Concepts in Density Functional Theory. In *Theoretical and Computational Chemistry*, Seminario, J. M., Ed. Elsevier: 1996; Vol. 4, pp 3-24.

114. Hohenberg, P.; Kohn, W., Inhomogeneous Electron Gas. *Phys. Rev.* **1964**, *136*, B864-B871.

115. Sholl, D. S.; Steckel, J. A., What Is Density Functional Theory? In *Density Functional Theory*, John Wiley & Sons, Inc.: 2009; pp 1-33.

116. Kohn, W.; Sham, L. J., Self-Consistent Equations Including Exchange and Correlation Effects. *Phys. Rev.* **1965**, *140*, A1133-A1138.

117. Delle Site, L., Levy–Lieb Principle: The Bridge between the Electron Density of Density Functional Theory and the Wavefunction of Quantum Monte Carlo. *Chem. Phys. Lett.* **2015**, *619*, 148-151.

118. Seminario, J. M., An Introduction to Density Functional Theory in Chemistry. In *Theoretical and Computational Chemistry*, Seminario, J. M.; Politzer, P., Eds. Elsevier: 1995; Vol. 2, pp 1-27.

119. Levy, M., Universal Variational Functionals of Electron Densities, First-Order Density Matrices, and Natural Spin-Orbitals and Solution of the V-Representability Problem. *Proc. Natl. Acad. Sci. U. S. A.* **1979**, *76*, 6062-6065.

120. Lieb, E. H., Density Functionals for Coulomb Systems. *Int. J. Quantum Chem.* **1983**, *24*, 243-277.

121. Harris, J.; Jones, R. O., The Surface Energy of a Bounded Electron Gas. *J. Phys. F: Met. Phys.* **1974**, *4*, 1170.

122. Becke, A. D., Density-Functional Exchange-Energy Approximation with Correct Asymptotic Behavior. *Phys. Rev. A* **1988**, *38*, 3098-3100.

123. Lee, C.; Yang, W.; Parr, R. G., Development of the Colle-Salvetti Correlation-Energy Formula into a Functional of the Electron Density. *Phys. Rev. B* **1988**, *37*, 785-789.

124. Perdew, J. P.; Chevary, J. A.; Vosko, S. H.; Jackson, K. A.; Pederson, M. R.; Singh, D. J.; Fiolhais, C., Atoms, Molecules, Solids, and Surfaces: Applications of the

Generalized Gradient Approximation for Exchange and Correlation. *Phys. Rev. B* **1992**, *46*, 6671-6687.

125. Perdew, J. P.; Wang, Y., Accurate and Simple Analytic Representation of the Electron-Gas Correlation Energy. *Phys. Rev. B* **1992**, *45*, 13244-13249.

126. Becke, A. D., Density-Functional Thermochemistry. III. The Role of Exact Exchange. *J. Chem. Phys.* **1993**, *98*, 5648-5652.

127. Derosa, P. A.; Seminario, J. M., Electron Transport through Single Molecules: Scattering Treatment Using Density Functional and Green Function Theories. *J. Phys. Chem. B* **2001**, *105*, 471-481.

128. Meller, J., Molecular Dynamics. In *Encyclopedia of Life Science*, Nature Publishing Group: 2001; pp 1-8.

129. Gale, J., Interatomic Potential Models for Ionic Materials. In *Handbook of Materials Modeling*, Yip, S., Ed. Springer Netherlands: 2005; pp 479-497.

130. Hermann, C., The Different Statistical Ensembles. General Methods in Statistical Physics. In *Statistical Physics: Including Applications to Condensed Matter*, Springer New York: 2005; pp 31-58.

131. Li, J., Basic Molecular Dynamics. In *Handbook of Materials Modeling*, Yip, S., Ed. Springer Netherlands: 2005; pp 565-588.

132. Raghavachari, K., Perspective on "Density Functional Thermochemistry. III. The Role of Exact Exchange". In *Theoretical Chemistry Accounts: New Century Issue*, Cramer, C. J.; Truhlar, D. G., Eds. Springer Berlin Heidelberg: Berlin, Heidelberg, 2001; pp 361-363.

133. Bergerhoff, G.; Brown, I. D., In *Crystallographic Databases*, Allen, F. H.; Bergerhoff, G.; Sievers, R., Eds. Chester, International Union of Crystallography, 1987.

134. Frisch, M. J.; Trucks, G. W.; Schlegel, H. B.; Scuseria, G. E.; Robb, M. A.; Cheeseman, J. R.; Scalmani, G.; Barone, V.; Mennucci, B.; Petersson, G. A., et al. *Gaussian 09*, Gaussian, Inc.: Wallingford, CT, USA, 2009.

135. Seminario, J. M.; Yan, L. M., Ab Initio Analysis of Electron Currents in Thioalkanes. *Int. J. Quantum Chem.* **2005**, *102*, 711-723.

136. Cristancho, D.; Seminario, J. M., Polypeptides in Alpha-Helix Conformation Perform as Diodes. *J. Chem. Phys.* **2010**, *132*, 065102.

137. Kumar, N.; Seminario, J. M., Design of Nanosensors for Fissile Materials in Nuclear Waste Water. *J. Phys. Chem. C* **2013**, *117*, 24033-24041.

138. Cardenas-Jiron, G. I.; Leon-Plata, P.; Cortes-Arriagada, D.; Seminario, J. M., Electrical Characteristics of Cobalt Phthalocyanine Complexes Adsorbed on Graphene. *J. Phys. Chem. C* **2011**, *115*, 16052-16062.

139. Bautista, E. J.; Yan, L.; Seminario, J. M., Ab Initio Analysis of Electron Transport in Oligoglycines. *J. Phys. Chem. C* **2007**, *111*, 14552-14559.

140. Salazar-Salinas, K.; Jauregui, L. A.; Kubli-Garfias, C.; Seminario, J. M., Molecular Biosensor Based on a Coordinated Iron Complex. *J. Chem. Phys.* **2009**, *130*, 105101.

141. Dovesi, R.; Causa, M.; Orlando, R.; Roetti, C.; Saunders, V. R., Ab Initio Approach to Molecular-Crystals -a Periodic Hartree-Fock Study of Crystalline Urea. *J. Chem. Phys.* **1990**, *92*, 7402-7411.

142. Roetti, C., The Crystal Code. In *Quantum-Mechanical Ab-Initio Calculation of the Properties of Crystalline Materials*, Pisani, C., Ed. Springer-Verlag: Berlin, 1996; Vol. 67, pp 125-137.

143. Dovesi, R.; Saunders, V. R.; Roetti, C.; Orlando, R.; Zicovich-Wilson, C. M.; Pascale, F.; Civalleri, B.; Doll, K.; Harrison, N. M.; Bush, I. J., et al., *Crystal06 User's Manual*: University of Torino: Torino, 2006.

144. Buttiker, M.; Imry, Y.; Landauer, R.; Pinhas, S., Generalized Many-Channel Conductance Formula with Application to Small Rings. *Phys. Rev. B* **1985**, *31*, 6207-6215.

145. Landauer, R., Spatial Variation of Currents and Fields Due to Localized Scatterers in Metallic Conduction. *IBM J. Res. Dev.* **1957**, *1*, 223-231.

146. Landauer, R., Electrical Resistance of Disordered One-Dimensional Lattices. *Philos. Mag.* **1970**, *21*, 863-867.

147. Landauer, R., Comment on Lodder Exact Electromigration Theory. *Solid State Commun.* **1989**, *72*, 867.

148. Landauer, R. W., Irreversibility and Heat Generation in the Computing Process. *IBM J. Res. Dev.* **1961**, *5*, 183-191.

149. Christensen, J.; Newman, J., A Mathematical Model for the Lithium-Ion Negative Electrode Solid Electrolyte Interphase. *J. Electrochem. Soc.* **2004**, *151*, A1977-A1988.

150. Yildirim, H.; Kinaci, A.; Chan, M. K. Y.; Greeley, J. P., First-Principles Analysis of Defect Thermodynamics and Ion Transport in Inorganic SEI Compounds: LiF and NaF. *ACS Appl. Mater. Interfaces* **2015**, *7*, 18985-18996.

151. Martinez De La Hoz, J. M.; Soto, F. A.; Balbuena, P. B., Effect of the Electrolyte Composition on SEI Reactions at Si Anodes of Li Ion Batteries. *J. Phys. Chem. C* **2015**, *119*, 7060-7068.

152. Martínez De La Hoz, J. M.; Balbuena, P. B., Reduction Mechanisms of Additives on Si Anodes of Li-Ion Batteries. *Phys. Chem. Chem. Phys.* **2014**, *16*, 17091-17098.

153. Ma, Y.; Balbuena, P. B., DFT Study of Reduction Mechanisms of Ethylene Carbonate and Fluoroethylene Carbonate on Li^+-Adsorbed Si Clusters. *J. Electrochem. Soc.* **2014**, *161*, E3097-E3109.

154. Martinez De La Hoz, J. M.; Leung, K.; Balbuena, P. B., Reduction Mechanisms of Ethylene Carbonate on Si Anodes of Lithium-Ion Batteries: Effects of Degree of Lithiation and Nature of Exposed Surface. *ACS Appl. Mater. Interfaces* **2013**, *5*, 13457-13465.

155. Li, T.; Balbuena, P. B., Theoretical Studies of the Reduction of Ethylene Carbonate. *Chem. Phys. Lett.* **2000**, *317*, 421-429.

156. Xu, K., Electrolytes and Interphases in Li-Ion Batteries and Beyond. *Chem. Rev.* **2014**, *114*, 11503-11618.

157. Vollmer, J. M.; Curtiss, L. A.; Vissers, D. R.; Amine, K., Reduction Mechanisms of Ethylene, Propylene, and Vinylethylene Carbonates. A Quantum Chemical Study. *J. Electrochem. Soc.* **2004**, *151*, A178-A183.

158. Leung, K., Two-Electron Reduction of Ethylene Carbonate: A Quantum Chemistry Re-Examination of Mechanisms. *Chem. Phys. Lett.* **2013**, *568-569*, 1-8.

159. Cárdenas-Jirón, G. I.; Leon-Plata, P.; Cortes-Arriagada, D.; Seminario, J. M., Electrical Characteristics of Cobalt Phthalocyanine Complexes Adsorbed on Graphene. *J. Phys. Chem. C* **2011**, *115*, 16052-16062.

160. Rangel, N. L.; Seminario, J. M., Single Molecule Detection Using Graphene Electrodes. *J. Phys. B: At., Mol. Opt. Phys.* **2010**, *43*, 115101.

161. Yan, L.; Seminario, J. M., Electron Transport in Nano-Gold-Silicon Interfaces. *Int. J. Quantum Chem.* **2007**, *107*, 440-450.

162. Jauregui, L. A.; Seminario, J. M., A DNA Sensor for Sequencing and Mismatches Based on Electron Transport through Watson-Crick and Non-Watson-Crick Base Pairs. *IEEE Sens. J.* **2008**, *8*, 803-814.

163. Sotelo, J. C.; Yan, L.; Wang, M.; Seminario, J. M., Field-Induced Conformational Changes in Bimetallic Oligoaniline Junctions. *Phys. Rev. A: At. Mol. Opt. Phys.* **2007**, *75*, 022511.

164. Jauregui, L. A.; Salazar-Salinas, K.; Seminario, J. M., Transverse Electronic Transport in Double-Stranded DNA Nucleotides. *J. Phys. Chem. B* **2009**, *113*, 6230-6239.

165. Bondi, A., Van Der Waals Volumes and Radii. *J. Phys. Chem.* **1964**, *68*, 441-451.

166. Ortiz, D. O.; Seminario, J. M., Direct Approach for the Electron Transport through Molecules. *J. Chem. Phys.* **2007**, *127*, 111106.

167. Seminario, J. M.; Zacarias, A. G.; Tour, J. M., Theoretical Study of a Molecular Resonant Tunneling Diode. *J. Am. Chem. Soc.* **2000**, *122*, 3015-3020.

168. Seminario, J. M., Quantum Current-Voltage Relation for a Single Electron. *J. Phys. B: At., Mol. Opt. Phys.* **2007**, *40*, F275-F276.

169. Yan, L.; Bautista, E. J.; Seminario, J. M., Ab Initio Analysis of Electron Currents through Benzene, Naphthalene, and Anthracene Nanojunctions. *Nanotechnology* **2007**, *18*, 485701.

170. Baskoutas, S.; Terzis, A. F., Size-Dependent Band Gap of Colloidal Quantum Dots. *J. Appl. Phys.* **2006**, *99*, 013708.

171. Delley, B.; Steigmeier, E. F., Size Dependence of Band Gaps in Silicon Nanostructures. *Appl. Phys. Lett.* **1995**, *67*, 2370.

172. Wang, K.; Rangel, N. L.; Kundu, S.; Sotelo, J. C.; Tovar, R. M.; Seminario, J. M.; Liang, H., Switchable Molecular Conductivity. *J. Am. Chem. Soc.* **2009**, *131*, 10447-10451.

173. Ramos-Berdullas, N.; Mandado, M., Revisiting the Calculation of I/V Profiles in Molecular Junctions Using the Uncertainty Principle. *J. Phys. Chem. A* **2014**, *118*, 3827-3834.

174. Shi, S.; Qi, Y.; Li, H.; Hector, L. G., Defect Thermodynamics and Diffusion Mechanisms in Li_2CO_3 and Implications for the Solid Electrolyte Interphase in Li-Ion Batteries. *J. Phys. Chem. C* **2013**, *117*, 8579-8593.

175. Shi, S.; Lu, P.; Liu, Z.; Qi, Y.; Hector, L. G.; Li, H.; Harris, S. J., Direct Calculation of Li-Ion Transport in the Solid Electrolyte Interphase. *J. Am. Chem. Soc.* **2012**, *134*, 15476-15487.

176. Koyama, Y.; Yamada, Y.; Tanaka, I.; Nishitani, S. R.; Adachi, H.; Murayama, M.; Kanno, R., Evaluation of Migration Energy of Lithium Ions in Chalcogenides and Halides by First Principles Calculation. *Mater. Trans.* **2002**, *43*, 1460-1463.

177. Maier, J., Defect Chemistry: Composition, Transport, and Reactions in the Solid State; Part I: Thermodynamics. *Angew. Chem. Int. Ed.* **1993**, *32*, 313-335.

178. Luo, H.; Xiao, S.; Wang, S.; Huai, P.; Deng, H.; Hu, W., Molecular Dynamics Simulation of Diffusion and Viscosity of Liquid Lithium Fluoride. *Comp. Mater. Sci.* **2016**, *111*, 203-208.

179. Kobelev, M., Molecular Dynamics Simulation of the Reciprocal Fused LiF-KBr Mixture: Local Structure and Self-Diffusion Coefficients. *Mol. Simul.* **2013**, *39*, 868-874.

180. Merlet, C.; Madden, P. A.; Salanne, M., Internal Mobilities and Diffusion in an Ionic Liquid Mixture. *Phys. Chem. Chem. Phys.* **2010**, *12*, 14109-14114.

181. Andreev, O. L.; Raskovalov, A. A.; Larin, A. V., A Molecular Dynamics Simulation of Lithium Fluoride: Volume Phase and Nanosized Particle. *Russ. J. Phys. Chem. A* **2010**, *84*, 48-52.

182. Sarou-Kanian, V.; Rollet, A. L.; Salanne, M.; Simon, C.; Bessada, C.; Madden, P. A., Diffusion Coefficients and Local Structure in Basic Molten Fluorides: In Situ NMR Measurements and Molecular Dynamics Simulations. *Phys. Chem. Chem. Phys.* **2009**, *11*, 11501-11506.

183. Ciccotti, G.; Jacucci, G.; McDonald, I. R., Transport Properties of Molten Alkali Halides. *Phys. Rev. A* **1976**, *13*, 426-436.

184. Stoebe, T.; Huggins, R., Measurement of Ionic Diffusion in Lithium Fluoride by Nuclear Magnetic Resonance Techniques. *J. Mater. Sci.* **1966**, *1*, 117-126.

185. Tasaki, K.; Goldberg, A.; Lian, J. J.; Walker, M.; Timmons, A.; Harris, S. J., Solubility of Lithium Salts Formed on the Lithium-Ion Battery Negative Electrode Surface in Organic Solvents. *J. Electrochem. Soc.* **2009**, *156*, A1019-A1027.

186. Asahi, R.; Freeman, C. M.; Saxe, P.; Wimmer, E., Thermal Expansion, Diffusion and Melting of Li2O Using a Compact Forcefield Derived from Ab Initio Molecular Dynamics. *Modell. Simul. Mater. Sci. Eng.* **2014**, *22*, 075009.

187. Long, J.; Yang, L.; Li, D., First-Principles Investigations of the Physical Properties of Antifluorite Li_2O under Various Pressures. *Solid State Sci.* **2013**, *19*, 12-18.

188. Sayle, T. X. T.; Ngoepe, P. E.; Sayle, D. C., Generating Structural Distributions of Atomistic Models of Li_2O Nanoparticles Using Simulated Crystallisation. *J. Mater. Chem.* **2010**, *20*, 10452-10458.

189. Oda, T.; Tanaka, S., Modeling of Li Diffusivity in Li_2O by Molecular Dynamics Simulation. *J. Nucl. Mater.* **2009**, *386-388*, 1087-1090.

190. Oda, T.; Oya, Y.; Tanaka, S.; Weber, W. J., Validation of Potential Models for Li_2O in Classical Molecular Dynamics Simulation. *J. Nucl. Mater.* **2007**, *367-370 A*, 263-268.

191. Hayoun, M.; Meyer, M.; Denieport, A., Complex Atomic-Diffusion Mechanism in Ionic Superconductors: The Case of the Lithium-Oxide Antifluorite. *Acta Mater.* **2005**, *53*, 2867-2874.

192. Wilson, M.; Jahn, S.; Madden, P. A., The Construction and Application of a Fully Flexible Computer Simulation Model for Lithium Oxide. *J. Phys.: Condens. Matter* **2004**, *16*, S2795-S2810.

193. Goel, P.; Choudhury, N.; Chaplot, S. L., Superionic Behavior of Lithium Oxide Li_2O: A Lattice Dynamics and Molecular Dynamics Study. *Phys. Rev. B* **2004**, *70*, 174307.

194. Rodeja, J. G.; Meyer, M.; Hayoun, M., Derivation and Validation of Model Potentials for Li_2O from Density-Functional Theory. *Modell. Simul. Mater. Sci. Eng.* **2001**, *9*, 81-96.

195. Fracchia, R. M.; Barrera, G. D.; Allan, N. L.; Barron, T. H. K.; Mackrodt, W. C., Lithium Oxide and Superionic Behaviour—a Study Using Potentials from Periodic Ab Initio Calculations. *J. Phys. Chem. Solids* **1998**, *59*, 435-445.

196. Oishi, Y.; Kamei, Y.; Akiyama, M.; Yanagi, T., Self-Diffusion Coefficient of Lithium in Lithium Oxide. *J. Nucl. Mater.* **1979**, *87*, 341-344.

197. Mulliner, A. D.; Aeberhard, P. C.; Battle, P. D.; David, W. I. F.; Refson, K., Diffusion in Li_2O Studied by Non-Equilibrium Molecular Dynamics for $873 < T/K < 1603$. *Phys. Chem. Chem. Phys.* **2015**, *17*, 21470-21475.

198. Iddir, H.; Curtiss, L. A., Li Ion Diffusion Mechanisms in Bulk Monoclinic Li_2CO_3 Crystals from Density Functional Studies. *J. Phys. Chem. C* **2010**, *114*, 20903-20906.

199. Bruno, M.; Prencipe, M., Ab Initio Quantum-Mechanical Modeling of the (0 0 1), (over(1,¯) 0 1) and (1 1 0) Surfaces of Zabuyelite (Li_2CO_3). *Surf. Sci.* **2007**, *601*, 3012-3019.

200. Duan, Y.; Sorescu, D. C., Density Functional Theory Studies of the Structural, Electronic, and Phonon Properties of Li_2O and Li_2CO_3: Application to CO_2 Capture Reaction. *Phys. Rev. B: Condens. Matter Mater. Phys.* **2009**, *79*, 014301.

201. Zhuravlev, Y. N.; Fedorov, I. A., The Nature of Electronic States and Chemical Bonding in Lithium and Potassium Carbonates. *J. Struct. Chem.* **2006**, *47*, 206-210.

202. Fedorov, I. A.; Zhuravlev, Y. N.; Korabel'nikov, D. V., Band Structure and Chemical Bond in Alkali Metal Carbonates. *Russ. Phys. J.* **2006**, *49*, 1106-1111.

203. Shang, S.-L.; Hector Jr, L. G.; Shi, S.; Qi, Y.; Wang, Y.; Liu, Z.-K., Lattice Dynamics, Thermodynamics and Elastic Properties of Monoclinic Li_2CO_3 from Density Functional Theory. *Acta Mater.* **2012**, *60*, 5204-5216.

204. Ji, Y.; Zhang, Y.; Wang, C. Y., Li-Ion Cell Operation at Low Temperatures. *J. Electrochem. Soc.* **2013**, *160*, A636-A649.

205. Shi, S.; Gao, J.; Liu, Y.; Zhao, Y.; Wu, Q.; Ju, W.; Ouyang, C.; Xiao, R., Multi-Scale Computation Methods: Their Applications in Lithium-Ion Battery Research and Development. *Chin. Phys. B* **2015**, *25*, 018212.

206. Politzer, P.; Murray, J. S.; Clark, T., Halogen Bonding and Other σ-hole Interactions: A Perspective. *Phys. Chem. Chem. Phys.* **2013**, *15*, 11178-11189.

207. Clark, T.; Hennemann, M.; Murray, J. S.; Politzer, P., Halogen Bonding: The σ-hole. *J. Mol. Model.* **2007**, *13*, 291-296.

208. Murray, J. S.; Lane, P.; Politzer, P., Expansion of the σ-hole Concept. *J. Mol. Model.* **2009**, *15*, 723-729.

209. Kale, S.; Herzfeld, J., Pairwise Long-Range Compensation for Strongly Ionic Systems. *J. Chem. Theory Comput.* **2011**, *7*, 3620-3624.

210. Mao, A. H.; Pappu, R. V., Crystal Lattice Properties Fully Determine Short-Range Interaction Parameters for Alkali and Halide Ions. *J. Chem. Phys.* **2012**, *137*, 064104.

211. Tasaki, K.; Harris, S. J., Computational Study on the Solubility of Lithium Salts Formed on Lithium Ion Battery Negative Electrode in Organic Solvents. *J. Phys. Chem. C* **2010**, *114*, 8076-8083.

212. Rappe, A. K.; Casewit, C. J.; Colwell, K. S.; Goddard, W. A.; Skiff, W. M., Uff, a Full Periodic Table Force Field for Molecular Mechanics and Molecular Dynamics Simulations. *J. Am. Chem. Soc.* **1992**, *114*, 10024-10035.

213. Plimpton, S., Fast Parallel Algorithms for Short-Range Molecular Dynamics. *J. Comput. Phys* **1995**, *117*, 1-19.

214. Humphrey, W.; Dalke, A.; Schulten, K., Vmd: Visual Molecular Dynamics. *J. Mol. Graphics* **1996**, *14*, 33-38.

215. Borodin, O.; Smith, G. D.; Fan, P., Molecular Dynamics Simulations of Lithium Alkyl Carbonates. *J. Phys. Chem. B* **2006**, *110*, 22773-22779.

216. Gurvich, L. V.; Veyts, I. V.; Alcock, C. B., *Thermodynamic Properties of Individual Substances*; CRC Press, 1989.

217. Ortman, M. S.; Larsen, E. M., Preparation, Characterization, and Melting Point of High-Purity Lithium Oxide. *J. Am. Ceram. Soc.* **1983**, *66*, 645-648.

218. Dissanayake, M. A. K. L.; Mellander, B. E., Phase Diagram and Electrical Conductivity of the Li_2SO_4-Li_2CO_3 System. *Solid State Ionics* **1986**, *21*, 279-285.

219. Bale, C. W.; Pelton, A. D., Coupled Phase Diagram and Thermodynamic Analysis of the 18 Binary Systems Formed among Li_2CO_3, K_2CO_3,Na_2CO_3, LiOH, KOH, NaOH, Li_2SO_4, K_2SO_4 and Na_2SO_4. *Calphad* **1982**, *6*, 255-278.

220. Ding, N.; Xu, J.; Yao, Y. X.; Wegner, G.; Fang, X.; Chen, C. H.; Lieberwirth, I., Determination of the Diffusion Coefficient of Lithium Ions in Nano-Si. *Solid State Ionics* **2009**, *180*, 222-225.

221. Ruffo, R.; Hong, S. S.; Chan, C. K.; Huggins, R. A.; Cui, Y., Impedance Analysis of Silicon Nanowire Lithium Ion Battery Anodes. *J. Phys. Chem. C* **2009**, *113*, 11390-11398.

222. Mehrer, H., *Diffusion in Solids: Fundamentals, Methods, Materials, Diffusion-Controlled Processes*; Springer-Verlag Berlin Heidelberg, 2007.